Multiscale Models for the Degradation, Damage, and Failure of Collagen-Based Soft Tissues

A DISSERTATION
SUBMITTED TO THE FACULTY OF
UNIVERSITY OF MINNESOTA
BY

Mohammad Faisal Hadi

IN PARTIAL FULFILLMENT OF THE REQUIREMENTS
FOR THE DEGREE OF
DOCTOR OF PHILOSOPHY

Professor Victor H. Barocas

June 2013

Acknowledgements

There are clearly too many people that I need to thank and acknowledge who have made this dissertation possible. However, I will do my best to recognize at least the primary forces that have shaped my work while on campus. To all those who will have to go unnamed--I am eternally grateful to you as well for supporting me over the years.

Dr. Victor Barocas has been an incredible advisor and mentor. An incomparable scientist, wordsmith, and puzzle master, he has never failed to support and champion the work of his students. Aside from all this he is also a great person--humble, thoughtful, articulate, and fatherly. He has been a true inspiration and I will continue to owe him a great deal.

My thesis committee has supported my work throughout. I would like to thank and acknowledge Dr. Hubel, Dr. Netoff, and Dr. Tranquillo, who have all played a significant role in helping me sort through my ideas and offered me guidance when I needed it.

All members of the Barocas Research Group, past and present, have supported me tremendously. In particular, my batchmates, Dr. Victor Lai and Dr. Sara Jouzdani, deserve tremendous praise for their genius, support, and empathy during our time together. Many others, Dr. Rouzbeh Amini, Amy Claeson, Inka Gyoneva, Sarah Hunt, Tina Nagel, Dr. Ramesh Raghupathy, Sachin Shah, Dr. Masano Sugiyama, Dr. Julie Whitcomb, and Colleen Witzenburg, have also been incredibly supportive. The post-docs that I have been more than fortunate to work with--Dr. Ed Sander, Dr. Spencer Lake, and Dr. Hallie Wagner--all deserve special credit for being such outstanding mentors and colleagues. I am also thankful for all the wonderful undergraduates that I have had the chance to work with in a wide range of different contexts.

My family and friends have always been a great strength--my wife Veena (my chief support and toughest critic, without whom this dissertation would have been impossible), my daughter Marjane, my mother-in-law Vasanthi, and my father-in-law Raja have all made my work easier. My parents, Mohammad and Parveen, and my siblings, Samina, Sattar, and Rubina, have sacrificed much to help me in countless ways. My family members Bart, Pam, and Gautham have also helped me out tremendously along the road. Thanks also to all my friends whose help I have gotten by on for many, many years.

Dedication

In honor of a new generation of thinkers and wizards:
Ebi, Fenris, Marji, Najda, Nia, Salma, and Yusef.

Table of Contents

List of Figures

Chapter 2: Simulated Remodeling of Loaded Collagen Networks

Chapter 3: Tissue-Level Failure from Collagen Fiber-Level Damage

Chapter 4: Microscale Fiber Network Alignment Affects Failure

Chapter 5: Mechanics of a Fiber Network Within a Non-Fibrillar Matrix

Chapter 6: Generating Mimetic Random Network Topologies

1. Introduction

1.1 Background

Multiscale computational models for the deformation, degradation, and failure of soft tissues can inform the work of tissue engineers (Zahedmanesh et al., 2012; Spencer et al., 2012; Black et al., 2008; Barocas and Tranquillo, 1997), clinicians who treat soft tissue injuries (Cumming et al., 2010; Ault and Hoffman, 1992), and biologists who study the growth and development of soft tissues (Bates, 2007; Driessen et al., 2008; Varner et al., 2010). Increasingly, mechanical models for tissues that couple multiple length scales include microstructural information in their design (Kao et al., 2011; Driessen et al., 2004). Multiscale tissue models are revealing fundamental insights into how and why tissues deform, degrade, and fail in response to loading (Sander et al., 2011; Zohdi, 2007). The rapid growth in computational resources available to researchers (such as through academic supercomputing facilities) has also lead to an increase in the complexity and fidelity of multiscale models for tissue mechanics that may not have been possible even a decade ago (Luo et al., 2009; Zhang et al., 2013).

The finite element method has served as a popular modeling approach to couple the material properties of tissues at varying length scales (Weinberg et al., 2010; Guilak and Mow, 2000; Humphrey, 2003; Raghupathy and Barocas, 2009). In the present dissertation, a series of multiscale models which couple a macroscale finite element continuum to deterministic microscale fiber networks were used to simulate the

degradation, damage, and failure of collagen-based tissues and tissue analogs. The models build on previous work that has focused primarily on the pre-failure mechanics of tissues (Chandran and Barocas, 2007; Stylianopoulos and Barocas, 2007b). Enzymatic degradation (Chapter 2) was modeled by changing the effective diameter of microscale collagen fibers over time to mimic the action of strain-dependent collagenases (Hadi et al., 2012a). Mechanical failure and damage (Chapters 3 and 4) was modeled via the failure of discrete collagen fibers in a tissue based on a critical stretch criterion (Hadi et al., 2012b; Hadi and Barocas 2013a). Related research on the mechanical role of non-fibrillar matrix in tissues (Chapter 5 and Appendix I) and on the mechanics of networks of varying topology (Chapter 6) is included that will largely shape future research on the failure of multicomponent tissues and tissues of varying microstructure (Lake et al., 2012a; Lai et al., 2013; Hadi and Barocas, 2013b).

1.2 Research Aims

Several aims have shaped the overall purpose of this dissertation. These aims have evolved over the course of several years as research progressed in several areas:

Aim 1: Develop a multiscale model for the mechanical damage and failure of tissues and tissue analogs (based on microscale fiber failure in representative volume element networks) that can inform the work of tissue engineers and clinicians.

Aim 2: Model the enzymatic mechanical degradation of a tissue over time based on the

strain-dependent action of collagenases on individual microscale collagen fibers.

Aim 3: Consider the role of fiber network topology and non-fibrillar matrix on the overall deformation and failure properties of fiber-based materials such as soft tissues.

1.3 Resulting Research

Completion of these aims has lead to several key research studies that have considered a single aim or some combination of these aims as applied to tissues and tissue analogs. These research studies comprise the major chapters of this dissertation and are outlined briefly below as they relate to the primary research aims of this dissertation.

Enzymatic Degradation (Chapter 2)

Current research suggests that the enzymatic degradation of collagen fibers (such as by collagenases) may exhibit strain-dependent kinetics (Bhole et al., 2009; Flynn et al., 2010). Understanding this process can offer insight into the dynamic mechanisms governing collagen management in tissues, such as during growth and development. The strain dependent decay of collagen may lead to self-organizing principles in tissues where fibers under tension (perhaps useful) are preserved while slack fibers (perhaps less useful) are degraded (Ruberti and Hallab, 2005). In this study, the strain-dependent decay and constant growth of collagen fibers was modeled in a multiscale fashion with uniaxial and biaxial geometries under displacement and load control (Hadi et al., 2012a). The model was informed by microstructural data from enzymatic decay experiments. For

uniaxially loaded dogbone samples, the model predicted an increase in the spread of fiber diameters over the course of degradation because of variations in individual fiber load. For the biaxially stretched case for cruciforms, the central sample region exhibited greater decay and less spread in fiber diameter as compared to the arms. Slight changes in the average fiber orientation in different regions of the cruciform were also apparent.

Fiber-Based Failure in Collagen Tissue Analogs (Chapters 3 and 4)

Characterizing and modeling failure at multiple length scales in native and engineered tissues is open problem in biomedical engineering (Ritter et al., 2009). Better multiscale models for mechanical tissue damage and failure can lead to improved methods of engineering tissues, an enhanced understanding of tissue pathologies, and greater insight into tissue structure-function relationships (Humphrey, 2003). In these two studies that consider failure in collagen-based materials, macroscale failure was linked to the failure of microscale collagen fibers (Hadi et al., 2012b; Hadi and Barocas, 2013a). Fibers were allowed to fail in microscale networks when they exceed a critical stretch. The microscale networks served as representative volume elements in a multiscale finite element framework that linked microscale fiber failure to macroscale failure outcomes. This method allowed for the modeling of failure in simple collagen tissue analogs (gels) and also lead to some insight into how microscale fiber alignment leads to different macroscale failure outcomes for collagen-based materials.

Role of Non-Fibrillar Matrix and Network Topology (Chapters 5, 6, and Appendix)

Since native and engineered tissues contain multiple components other than fibrillar collagen and also have varied collagen microstructures, several studies were completed to consider the role of non-fibrillar matrix and varying network topology on tissue mechanics (Lake et al., 2012a; Lai et al., 2013; Hadi and Barocas, 2013b). Outcomes from these studies can be useful in developing multiscale failure models that consider multiple components (such as cells or proteoglycans) and multiple fiber network topologies (of collagen or other protein biopolymers) in tissues. The ability to link network topology to mechanical outcomes is also a vital tool in developing fiber networks for multiscale tissue models.

2. Simulated Remodeling of Loaded Collagen Networks via Strain-Dependent Enzymatic Degradation and Constant-Rate Fiber Growth

The content of this chapter was previously published as a research article in the journal *Mechanics of Materials* by Hadi, Sander, Ruberti, and Barocas (Hadi et al., 2012a).

2.1 Introduction

Throughout life, the tissues of the body change in response to various environmental cues. The fundamental processes of growth and remodeling are essential for proper development of the individual and for healing following injury or disease. Examples include development of the embryonic heart (Nerurkar et al., 2006) and brain (Varner et al., 2010), post-infarction cardiac remodeling (Weber, 1997; Holmes et al., 2005), dermal wound healing and scarring (Madden and Peacock Jr, 1971; Cumming et al., 2010), and vascular remodeling (Adiguzel et al., 2009; Galis and Khatri, 2002; Taber and Humphrey, 2001). The evolution of bioengineered tissues follows a similar course (Robinson et al., 2008; Sander and Barocas, 2008; Sacks et al., 2009). The underlying processes are poorly understood and involve complex biochemical, bioelectrical, and biomechanical interactions between cells and extracellular matrix (ECM). Great progress toward understanding these interactions has been made using models that treat the tissue, including its constituent ECM, as a continuum (Ramasubramanian and Taber, 2008) or using a fiber-population-based model (Driessen et al., 2008; Kuhl et al., 2005). Cell-ECM interactions, however, are coordinated both locally and globally, such that changes in the

microenvironment produce cell-directed organizational and compositional tissue adaptation. It is therefore desirable that one considers a model with a more realistic representation of the tissue architecture.

In native and engineered load-bearing soft tissues, the primary ECM component that resists tensile load is fibrillar collagen, in particular types I and III, forming into fibrils, fibers and, depending on the tissue, more complex, hierarchical structures. Networks, particularly unstructured networks, show very different behavior from structured networks (Chandran and Barocas, 2006; Sander et al., 2010; Sastry et al., 1998; Stein et al., 2008). Most importantly among these, the unstructured network has far greater potential for fiber rearrangement under load, which leads to certain characteristic features in contrast to structured networks: greater fiber rotation (Chandran and Barocas, 2006); smaller fiber stretches vis-à-vis the tissue stretch, especially in uniaxial loading (Sander et al., 2009b); greater variation in stretch among fibers (Chandran and Barocas, 2004); and large Poisson's ratios in tension (Stylianopoulos and Barocas, 2007b).

The distribution of fiber stretches may be critical to microstructural remodeling in a tissue. There are a number of enzymes that degrade ECM proteins, notably the matrix metalloproteinases (MMPs). MMPs are a family of mammalian proteases that degrade various constituents of the ECM and participate in the turnover of type I collagen (Lauer-Fields et al., 2002; Pardo and Selman, 2005). Bacterial collagenases (BC) have also been shown to degrade type I collagen, though with less specificity, and are often used *in vitro*

to study the effects of enzymatic degradation on ECM proteins (Ruberti and Hallab, 2005). Recent work (Bhole et al., 2009; Flynn et al., 2010) has shown that MMP8 and BC kinetics for the degradation of reconstituted and native type I collagen fibers are strain dependent. Results from Bhole et al.'s micrometer-scale study exploring the strain dependent effects of BC on type I collagen fibers were directly used in the development of our present multiscale fiber degradation model. In the study, Bhole et al. used a novel in vitro method to measure the radial degradation of reconstituted type I collagen fibers by BC (Bhole et al., 2009). The method employed a microliter-scale reaction chamber in which reconstituted collagen networks were mechanically strained using a set of functionalized micropipettes while the networks were immersed in a highly concentrated BC solution. Dynamic changes in fiber diameter were then measured using microscopic differential interference contrast imaging to determine the strain dependence of fiber degradation.

In summary, two key observations motivate this work: (1) the mechanical environment within a complex tissue can vary from fiber to fiber, and (2) the MMP-mediated degradation of a collagen fiber is dependent on that mechanical environment. Thus, the objective of the current study was to conduct a preliminary exploration of how a model tissue might evolve under strain-dependent remodeling conditions.

2.2 Methods

2.2.1 Multiscale Model Implementation

Simulations of remodeling within a collagen network were implemented using a deterministic multiscale mechanical model. The model linked the volume-averaged stress in micrometer-scale representative volume elements (RVEs) to a millimeter-scale finite element (FE) continuum. The general concept is illustrated in Fig. 2.1. Hexahedral elements with linear shape functions (8 Gauss points per element) comprised the FE domain. Each element was assigned a unique RVE, and RVE networks at each Gauss point within the element were updated discretely during the simulation. RVEs were comprised of a network of several hundred discrete type I collagen fibers within a cubic unit volume. Displacements were communicated from the continuum scale to the microscopic scale as boundary conditions on the RVE domain, and the resulting stresses were communicated to the continuum scale as a volume-averaged stress over the domain. The model iterated between both scales until the microscopic-scale and the macroscopic-scale force balances were satisfied. The model has been used previously to simulate the mechanics of collagen-based materials (Luo et al., 2009; Sander et al., 2009a; Stylianopoulos and Barocas, 2007a). In the current study, the model was modified to include strain-dependent collagen fiber decay and constant-rate fiber growth as described in Section 2.2.2.

Each RVE within the model was created using a stochastic fiber growth algorithm (Chandran and Barocas, 2006; Sander et al., 2009b). Fibers were grown from a random set of seed points that intersected to form cross-links. A typical RVE is shown in Fig. 2.1. For the present study, RVEs contained a mean of 1,007 fibers and had an edge length of

roughly 30 μm. Fibers within the RVE (either in extension or contraction) were governed by the exponential force-strain constitutive relation:

$$F_{fiber} = \frac{E_{fiber} A_{fiber}}{B} (\exp[B\ \varepsilon_G] - 1) \quad (2\text{-}2.1)$$

where F_{fiber} is the resultant force along a fiber, E_{fiber} is the Young's modulus for a fiber at infinitesimal strain, A_{fiber} is the fiber cross-sectional area, ε_G is the fiber Green strain, and B is a fitting parameter. The relation was adapted from a previous fiber-based soft tissue model (Billiar and Sacks, 2000) and has been used in prior multiscale simulations (Stylianopoulos and Barocas, 2007b; Sander et al., 2009b). For the present study, a value of 79 MPa was used for E_{fiber}, a value of 1.2 for B, and A_{fiber} was calculated from an initial fiber diameter of 100 nm, based on a previous analysis of collagen gels (Stylianopoulos and Barocas, 2007b).

At each simulation step, the displacement field that yields mechanical equilibrium within the continuum is determined iteratively. At the macroscale, the material properties of the FE continuum were derived from the mechanical response of RVEs at Gauss points within each element. Based on the macroscale deformation of the FE continuum, the volume-averaged Cauchy stress was calculated for each RVE (Chandran and Barocas, 2007):

$$\sigma_{ij} = \frac{1}{V} \int_V \sigma_{ij}^L \, dV = \frac{1}{V} \sum_{bc} x_i f_j \quad (2\text{-}2.2)$$

In this equation σ is the macroscale averaged Cauchy stress, σ^L is the local microscale stress, V is the RVE volume, *bc* indicates a discrete summation over all RVE boundary fiber cross-links, x is the boundary fiber cross-link coordinate, f is the force acting on the boundary fiber cross-link, and index notation is used. The continuum force balance based on the volume-averaged stress is given by (Chandran and Barocas, 2007):

$$\sigma_{ij,j} = \frac{1}{V}\oint_{\partial V}\left(\sigma_{ij}^{L} - \sigma_{ij}\right)u_{k,i}n_k dS \qquad (2\text{-}2.3)$$

In this relation n is the normal vector to the RVE boundary and u is the displacement of the RVE boundary. For more details see Stylianopoulos and Barocas (2007b).

2.2.2 Enzymatic Decay and Constant Growth Model

Strain-dependent fiber decay and constant fiber growth kinematic expressions were incorporated into the multiscale mechanical model to simulate remodeling within a collagen network over time. As a starting point, the following strain-dependent kinetic expression governing fiber decay was implemented:

$$dr/dt = -k_1\, r \exp[\, -k_2\, (\lambda_{fiber} - 1)\,] \qquad (2\text{-}2.4)$$

The expression is a function of fiber radius, r, and fiber stretch, λ_{fiber} (where $\lambda_{fiber} > 1$ in extension and $\lambda_{fiber} < 1$ in contraction), and contains two kinetic parameters, k_1 and k_2.

The expression was fit to a set of experimental results for the degradation of a micrometer-scale collagen network via bacterial collagenase (BC) as seen in Fig. 2.2 (Bhole et al., 2009). Using the strain-free decay experimental case (where $\lambda_{fiber} = 1$), model parameter k_1 was first fit to a value of 10.5×10^{-4} nm/sec by iteratively minimizing the sum of squared error between model and experimental fiber diameter (determined in the experiment via differential interference contrast microscopy) (Bhole et al., 2009). Parameter k_2 was then fit to a unitless value of 0.83 using the experimental case where the network was held under strain. For this fit, a simulated microscale RVE network was held at a constant 25% stretch. All fibers within the RVE were set to an initial diameter of 100 nm and the fiber decay expression was then applied to fibers to simulate exposure to BC for 2500 seconds. The sum of squared errors in diameter between model and experiment was then minimized iteratively. It is noted that the fit is not particularly good, suggesting that a more accurate model could be developed, but the simple exponential decay model was chosen for this initial study.

A constant-rate radial growth parameter was later added to Eq. 2-2.4 to simulate coupled growth and decay of collagen fibers. This constant-rate growth with strain-dependent decay kinetic expression was:

$$dr/dt = k_3 - k_1 r \exp[-k_2 (\lambda_{fiber} - 1)] \qquad (2\text{-}2.5)$$

In this relation, the constant-rate growth parameter k_3 was set to a trial value of 0.10

nm/sec and was implemented to gauge the response of the system to the simultaneous growth and decay of fibers. This trial value for k_3 was chosen to ensure that the system would be in a state of net growth throughout the duration of the simulation.

Both kinetic expressions in Eq. 2-2.4 and Eq. 2-2.5 impact the mechanics of RVE fibers within the model that are governed by the fiber constitutive relation given in Eq. 2-2.1. A change in a fiber's radius, r, over time by decay and growth will change its effective cross-sectional area, A_{fiber}, which is utilized in the fiber's constitutive relation. The fiber stretch, λ_{fiber}, that drives the kinetic expressions for fiber degradation is used in calculating the fiber Green strain, ε_G, which is also utilized in the fiber constitutive relation. These fiber-level expressions in turn impact the macroscale stress field via the volume-averaged stress for an RVE that is determined by the volume-averaging relation given previously in Eq. 2-2.2 (Chandran and Barocas, 2007).

2.2.3 Case Studies

Constant-force uniaxial extension and constant-strain biaxial extension simulations were implemented over a time course of 2,500 seconds with two distinct geometries for the decay and growth scenarios. For the constant-force uniaxial simulations, a dogbone geometry with a 290-element / 2,320-RVE mesh was used. The dogbone had a maximum length of 42.0 mm in the direction of loading, 17.0 mm in width, and 2.0 mm in thickness, as shown in Fig. 2.1. For the constant-strain equibiaxial extension simulations, a cruciform with a 316-element / 2,528-RVE mesh was used. One quadrant of the

cruciform, with symmetry boundary conditions, was used with maximum axial dimensions of 22.0 mm and 20.0 mm, and a thickness of 1.0 mm, as shown in Fig. 2.1. The cruciform had an arm width ratio of 1:2, with the sample grip in axis 1 measuring 4.0 mm on its edge, and the sample grip in axis 2 measuring 8.0 mm. This geometry was chosen to be consistent with previous experimental and computational studies (Sander et al., 2009b; Jhun et al., 2009). The mesh discretization was tested against a refined 1172-element uniaxial mesh and resulted in a mean grip-to-grip Green strain difference of only 0.19% versus the 290-element mesh over a 1000-second fixed force uniaxial hold with decay, ensuring that the chosen mesh discretization was sufficiently refined for the present study.

For each simulation, all fibers were set to an initial diameter of 100 nm. The sample was then strained incrementally to the target grip force or extension, and the decay and growth kinetic relations were applied over a time course of 2,500 seconds. Four distinct simulations were conducted for the study: (1) uniaxial decay with a fixed grip force of 0.2 N, (2) uniaxial decay with a fixed grip force of 0.4 N, (3) biaxial decay with a fixed equibiaxial strain of 30%, and (4) biaxial growth with decay with a fixed equibiaxial stretch of 30%.

At each simulation step, all discrete microscale fiber positions, fiber lengths, and fiber diameters in the simulation were recorded for analysis, along with the macroscale FE nodal positions, Cauchy stress, and grip forces. Uniaxial simulations contained

approximately 2,300,000 discrete fibers, and biaxial extension simulations contained approximately 2,600,000 discrete fibers. After simulations were completed, fiber and RVE statistics were calculated. As a measure of stiffness, selected RVEs were stretched uniaxially by 25%. The normal Cauchy stress in the axis of strain was taken as a measure of the network stiffness in that dimension. The diagonal components of the mass-weighted fiber orientation tensor, Ω, for RVEs were also calculated for analysis using the expression:

$$\Omega_{ij} = \frac{\sum m_{fiber}\, n_i n_j}{m_{total}} \qquad (2\text{-}2.6)$$

The expression was summed over each fiber in the network where m_{fiber} is the mass of the fiber, m_{total} is the total fiber mass in the network, n is the unit vector pointing along the fiber, and index notation was used (Stylianopoulos and Barocas, 2007b; Sander and Barocas, 2009c). All simulations were implemented using a custom C code (utilizing MPI message passing) on a 30-core sub-cluster at the Minnesota Supercomputing Institute. Each simulation had a wall time of approximately 14 hours. All post-processing and data analysis was done using MATLAB (Natick, MA).

2.3 Results

2.3.1 Constant-Force Uniaxial Extension with Strain-Dependent Enzymatic Decay

The 0.2 N uniaxial extension experiment on a dogbone is shown in Fig. 2.3. The stress

was, as expected, fairly uniform in the center of the dogbone but with some stretch dependent heterogeneity. Networks in the central gauge region of the sample became highly aligned in the direction of stretch, and the sample became considerably thinner, consistent with our previous theoretical work (Stylianopoulos and Barocas, 2007b) and experimental studies on collagen gels in tension (Lake and Barocas, 2011a). A network near the grip, shown for comparison, experienced less stress and less rearrangement.

A snapshot from the enzyme-induced creep of the sample is shown in Fig. 2.4. As the fibers were degraded by the enzyme, the sample lengthened over time, thinning further in the central gauge region. The average fiber diameter in each element decreased with time but remained nearly uniform over the central region, indicating that average fiber stretches were consistent locally. The regional element-to-element variation in Fig. 2.4 is due to individual differences in the networks at each Gauss point in the mesh. That is, the slight inhomogeneity of the fiber networks led to a slight inhomogeneity in degradation rate.

The network-level changes are seen more clearly in histograms of fiber diameters for a set of RVEs from the central gauge region of the sample (Fig. 2.5). Recalling that the initial fiber distribution was a delta function (s.d. = 0) at r = 100 nm, we see a steady spread of the distribution over time to a value of 5.89 nm at t = 1500. The spread resulted from different fibers within the network being under different loads, which in turn led to different degradation rates. Thus, fibers at low loads degraded quickly, producing the

low-radius end of the distribution and separating from those at higher loads, which degraded more slowly. The global spread in fiber diameter is also apparent by evaluating average diameter in the sample over time (Fig. 2.4). Again, areas with diminished fiber stretch, such as in the peripheries of the grip region, experienced increased degradation as compared with the central gauge region.

When the load was changed to 0.4 N, two major effects were observed, as can be seen in Fig. 2.6. In both cases, the sample strain increased monotonically with time, and the 0.4 N load sample stretched more than the 0.2 N sample (Fig. 2.6a), but the ratio between the two decreased over time due to greater mass loss in the 0.2 N case (Fig. 2.6b). Early on, the two samples degraded at nearly the same rate, but as strains in the 0.4 N case got larger, its degradation rate slowed down, leading to a smaller difference in tissue strain between the two cases.

2.3.2 Constant-Strain Equibiaxial Extension with Strain-Dependent Enzymatic Decay

In the second set of simulations, the model was used to simulate the mechanics of a more complex and more tissue-like loading environment using one quadrant of a 1:2 arm-ratio cruciform sample. A fixed 30% equibiaxial stretch was applied to the cruciform that was then exposed to enzymatic decay. The resultant maximum fiber stretch per element is plotted alongside the maximum fiber diameter per element in Fig. 2.7a. Areas with collagen fibers experiencing the greatest fiber stretch coincided with areas with the

greatest fiber diameter. As compared with the uniform loading and fiber stretch in the center of the uniaxial dogbone geometry, the cruciform geometry produced more pronounced inhomogeneity in fiber stretch and loading.

Three distinct regions of interest – the belly, the axis 1 arm, and the axis 2 arm – showed dissimilar fiber stretch ranges. These regions are marked in Fig. 2.8 alongside histograms of the fiber diameter in each region after 500 and 1500 seconds of enzymatic decay. Each histogram represents fibers from 8 individual RVEs from a region of interest. The standard deviation in the fiber diameter increased for each region from 500 to 1500 seconds of decay. The belly of the sample had the smallest spread in fiber diameter and the smallest average fiber diameter at both time points. The axis 1 arm, where the stress was largest, retained the largest fiber diameter over time and also had the widest spread in fiber diameter.

The forces in arm 1 (normal force acting along axis 1) and arm 2 (normal force acting along axis 2) diminished over time, as seen in Fig. 2.9. The steepest drop in force occurred at the initial onset of enzymatic decay, and the rate of decay decreased over time. The ratio between the two arm forces (force in arm 1 / force in arm 2) increased slightly over time and appeared to level off towards the end of the simulation.

2.3.3 Constant-Strain Equibiaxial Extension with Constant-Rate Growth and Strain-Dependent Decay

As in the decay-only case, the constant-rate growth with decay case revealed a correlation between areas of greatest fiber stretch and areas with the greatest fiber diameter, as seen in Fig. 2.7b. The maximum and average fiber diameter per element, however, increased across all elements due to the action of the growth term in equation (2-2.5). The sample was held under a constant 30% equibiaxial extension, though the element-by-element maximum fiber stretches revealed non-uniformity in the local collagen network stretch. The forces in the arms increased over time due to growth, and, as in the degradation-only case, there was a slight shift toward equal forces as the system evolved (Fig. 2.9b).

The mass weighted fiber orientation tensor, Ω, was calculated for 8 RVE collagen networks in each of the three regions of interest. Prior to loading and modeling growth and decay, networks in the sample had roughly an isotropic fiber orientation with $\Omega_{11} \approx \Omega_{22} \approx \Omega_{33} \approx 0.33$, with each normal component of the tensor yielding a relative strength of alignment in the corresponding axis. Immediately after loading but before any degradation / growth, the orientation shifted considerably due to fiber realignment ($t = 0$ points in Fig. 2.10). The diagonal elements of Ω were (0.56, 0.28, 0.16) for the narrow horizontal arm, (0.30, 0.48, 0.22) for the wide vertical arm, and (0.40, 0.42, 0.18) for the belly. To summarize, the fibers in the arms tended to align in the direction of pull, and the fibers in all sections tended to rotate into the plane of biaxial extension.

Subsequent to the shift from isotropy after loading, the networks evolved over time from the action of constant-rate growth and enzymatic decay. The belly of the sample

experienced the least change in fiber orientation, with its Ω_{11} and Ω_{22} values increasing approximately 2.5% and the network remaining nearly isotropic in the 1-2 plane. The axis 1 arm experienced an 8.4% increase in Ω_{11}, shifting alignment into the direction of fixed extension for that arm via coupled growth and decay. The axis 2 arm experienced a similar but slightly less pronounced increase of 6.5% in its Ω_{22} component.

The relative change in RVE stiffness in the 1 and 2 directions is given in Fig. 2.11. The axis 1 arm stiffness in direction 1, calculated from 3 RVEs within the region subjected to a set of uniform uniaxial stretches, experienced a significant increase in the mean as compared with the other two regions ($p<0.05$). The mean stiffness in arm 2 increased in axis 2, but was not statistically significant ($p =0.142$) as compared to the mean stiffness in the other two regions.

2.4 Discussion

As seen in Fig. 2.6b, the 0.4 N uniaxial hold simulation with decay had a diminished rate of fiber mass loss over time as compared with its 0.2 N counterpart. This is likely due to a subset of fibers within the 0.4 N hold that experienced greater strains than the 0.2 N case, and as a result, underwent diminished enzymatic degradation. In Fig. 2.6a, the greater sample strain over time for the 0.4 N case is evident. Qualitatively, the non-linear increase in strain over time for both the 0.2 N and 0.4 N holds and the greater strains generated with a larger magnitude fixed force resembles the experimental strain results from a set of creep experiments conducted recently by Zareian et al. with millimeter-scale

collagenous corneal strip samples subjected to enzymatic decay (Zareian and Ruberti, 2010). This similarity is comforting, but the simplifications of the model must still be recognized. Immediately apparent is non-exponential nature of the decay in the experiments fit in Fig. 2.2. The actual degradation is slower at short time and then faster at long time, suggesting that a nonlinear equation for degradation could provide a better model. We would expect significant quantitative differences from a more accurate model but would not expect changes to the qualitative observations made here.

It also must be recognized that a real fiber will eventually fail. Shen *et al.* (2008) found that they could stretch collagen fibrils to 30-50% engineering strain without failure, but that yielding began at approximately 20% strain. Especially in the 0.4 N uniaxial extension case, the strains reached very large values (>100% engineering strain). The large strains are the result of a fixed load scenario where the grip-to-grip strain is increasing to maintain load in response to the dynamic degradation of fibers over time. One must assume that the sample would fail before being able to achieve some of our results. A model incorporating fiber failure as well as degradation and growth would be an important next step in analysis of these systems.

In the case of the constant strain biaxial enzymatic decay simulation, the results were consistent with remodeling serving as an adaptive process. Regions of higher stress (the arms, in particular the narrow arm) did not degrade as quickly as those of lower stress (the belly), and the relative stiffness of the regions under higher load increased vis-à-vis

those under lower load. The belly region is important not only because its lower stresses provide for faster degradation, but also because the biaxial nature of the stress on the belly leads to roughly uniform stress within the network, so the spread in the fiber diameter was smaller. In the arms, fibers that were aligned in the stretch direction experienced significantly more stretch than those that were aligned transversely to the stretch direction, leading to greater variation in degradation rate and a greater spread in fiber diameter in Figure 2.8. The structural variations led to mechanical anisotropy of the sample, as shown in Fig. 2.11.

2.5 Conclusion

The model in the present study was able to successfully transfer a microscale fiber-based expression for strain-dependent decay and constant-rate growth into a deterministic macroscale outcome for an evolving tissue analog. Remodeling of collagenous tissue is an extremely complex process, including not only fiber degradation and growth but also mechanobiological effects on the cells in the tissue (e.g., changes in rate of MMP secretion or collagen deposition in response to different loads, Collins et al., 2005). The detailed interrelation between the fiber network and the cells that create and inhabit it, especially during development, growth, injury, and disease, remains an open question and important area for future study.

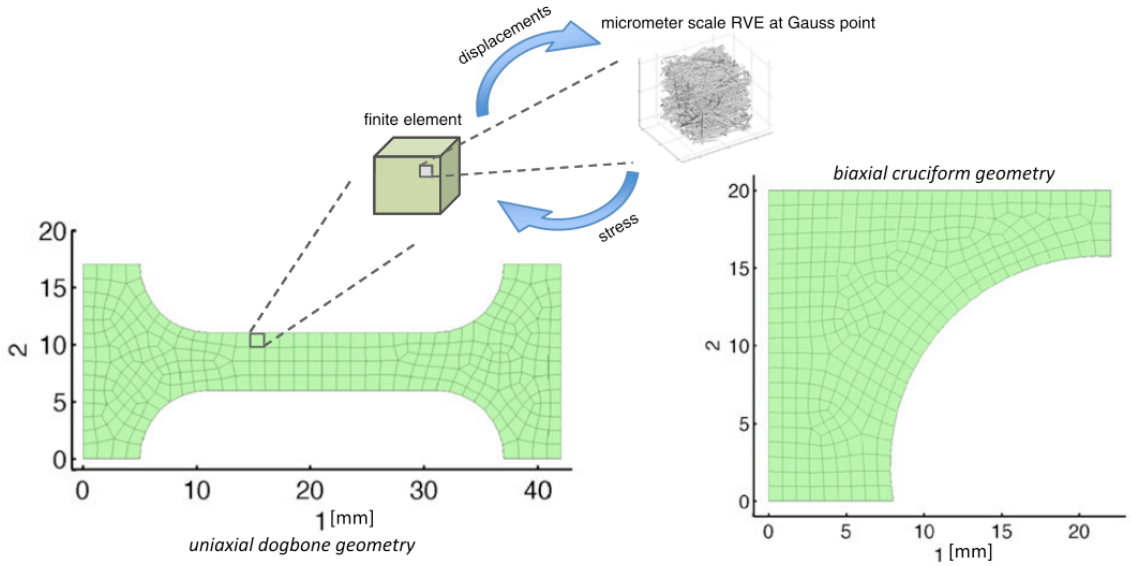

Fig. 2.1: Simulation geometries and overview of the multiscale model. In the multiscale model, displacements were communicated from the continuum scale to the microscopic scale as boundary conditions on the RVE domain, and the resulting stresses were communicated to the continuum scale as a volume-averaged stress over the domain.

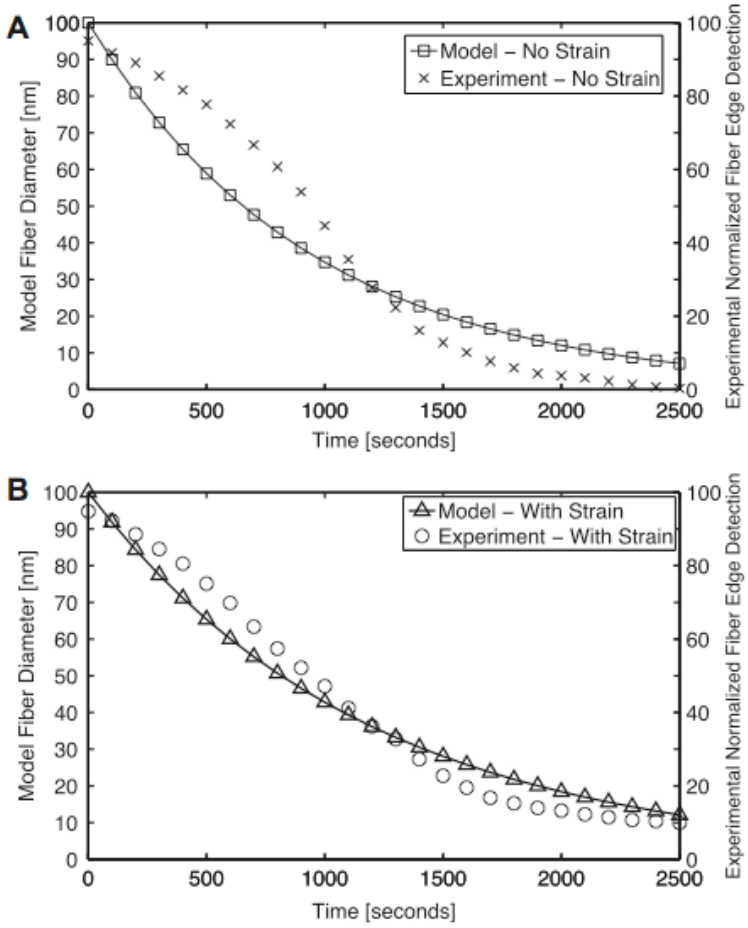

Fig. 2.2: Change in the microscale model fiber diameter over time fit to the experimental normalized fiber edge detection results (normalized measure of the experimental fiber diameter) from Bhole et. al (2009) for the (A) unstrained and (B) strained case. The loss of fiber diameter is due to enzymatic decay via bacterial collagenase.

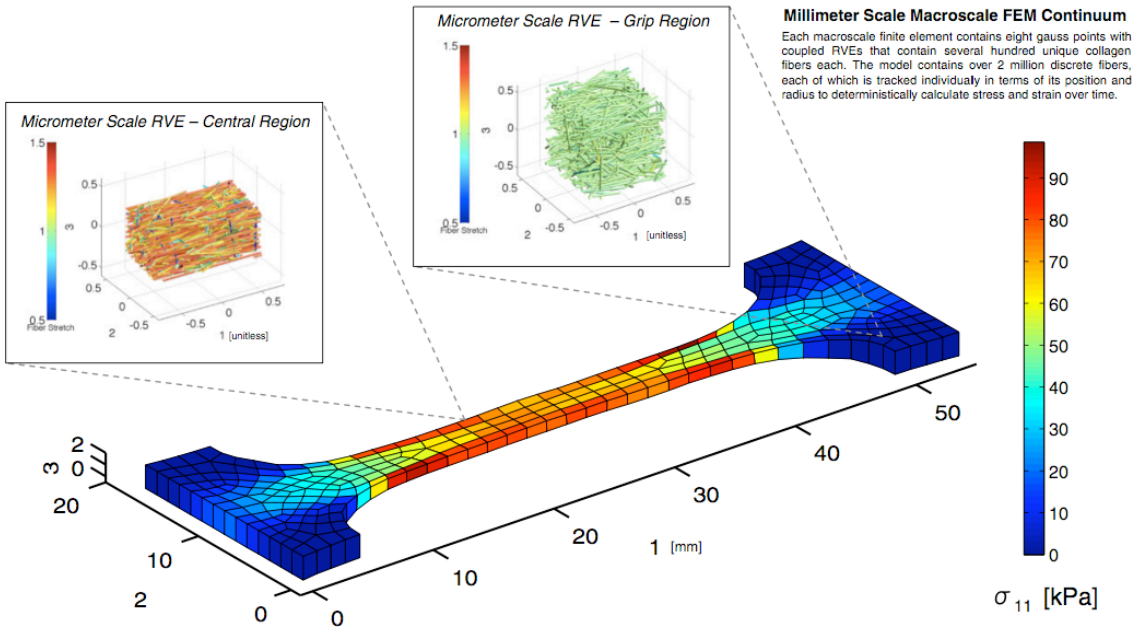

Fig. 2.3: The σ_{11} Cauchy stress plotted over the deformed macroscale mesh for the uniaxial 0.2-N fixed force with enzymatic decay simulation case at t = 500 seconds. RVEs from two selected macroscale elements in the central and grip regions of the sample are plotted in their deformed configuration depicting fiber stretch within individual RVE networks.

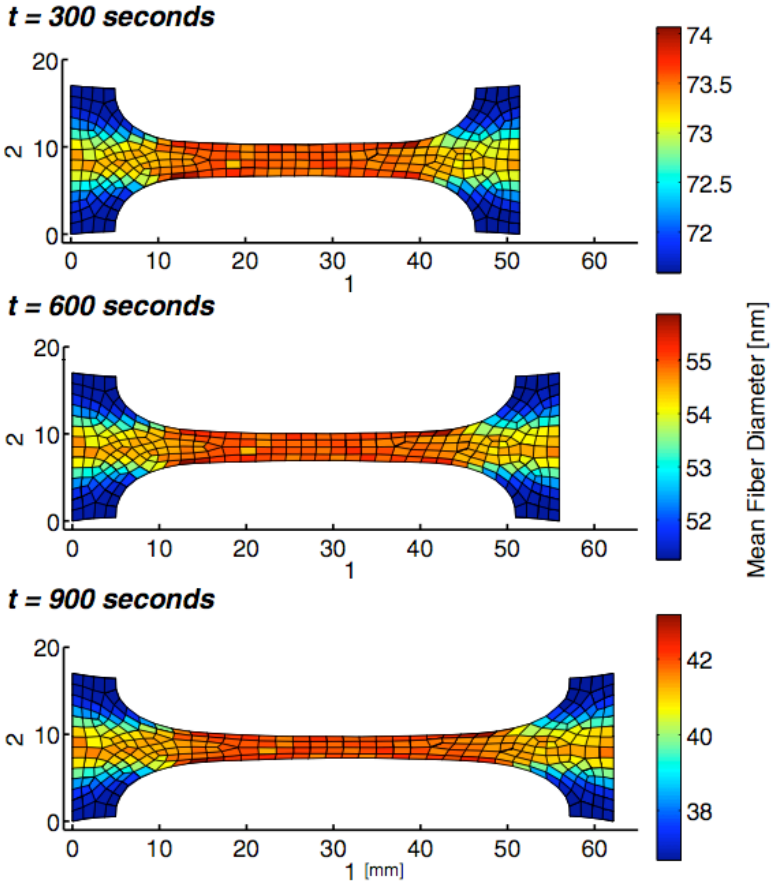

Fig. 2.4: Mean fiber diameter per element plotted over the deformed mesh for the uniaxial fixed 0.2-N force hold with enzymatic decay simulation at t = 300, t = 600, and t = 900 seconds.

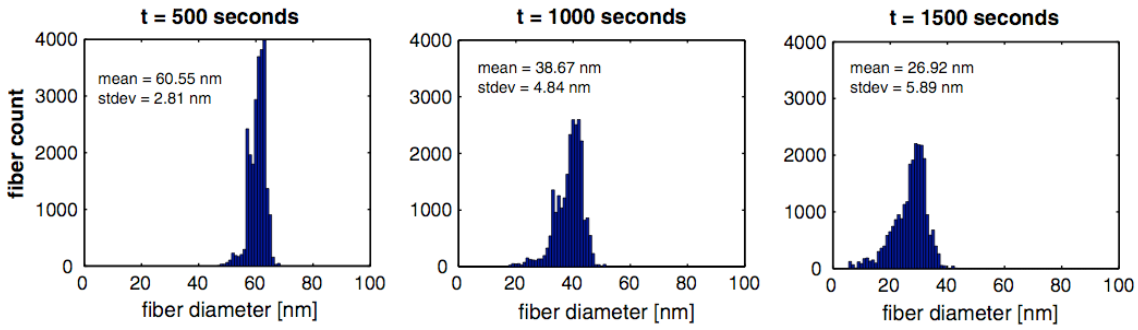

Fig. 2.5: Fiber diameter histograms at t = 500, t = 1000, and t = 1500 seconds for the 0.2-N uniaxial fixed force with enzymatic decay simulation for n = 24 RVEs within the central gauge region of the dogbone sample.

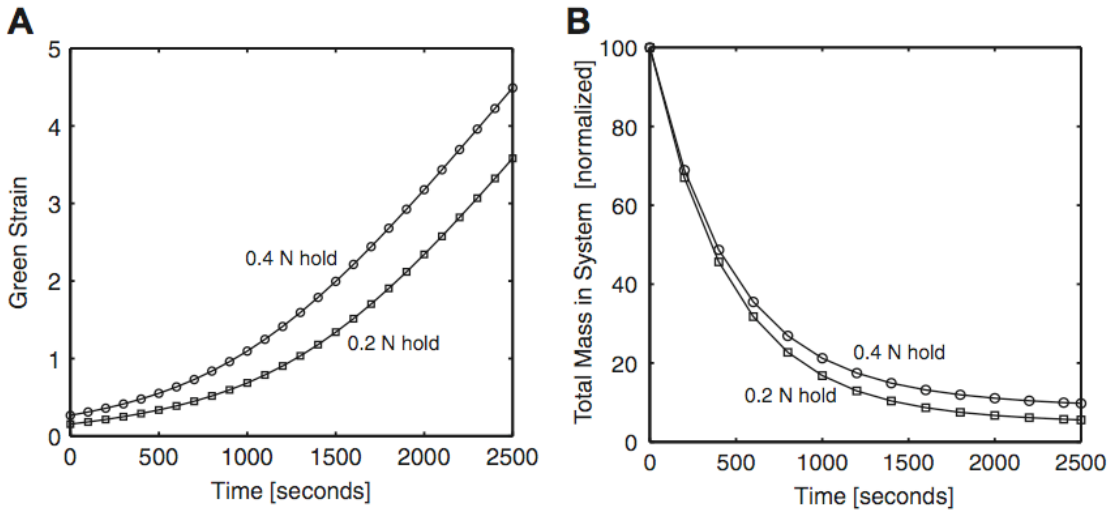

Fig. 2.6: (A) the macroscale Green strain in the 1 direction over time for the uniaxial dogbone fixed force with enzymatic decay simulations. Two different hold forces were implemented. The Green strain was calculated using the reference sample length from grip-to-grip. (B) Decay in mass over time for the uniaxial enzymatic decay case for the 0.2-N and 0.4-N fixed force holds.

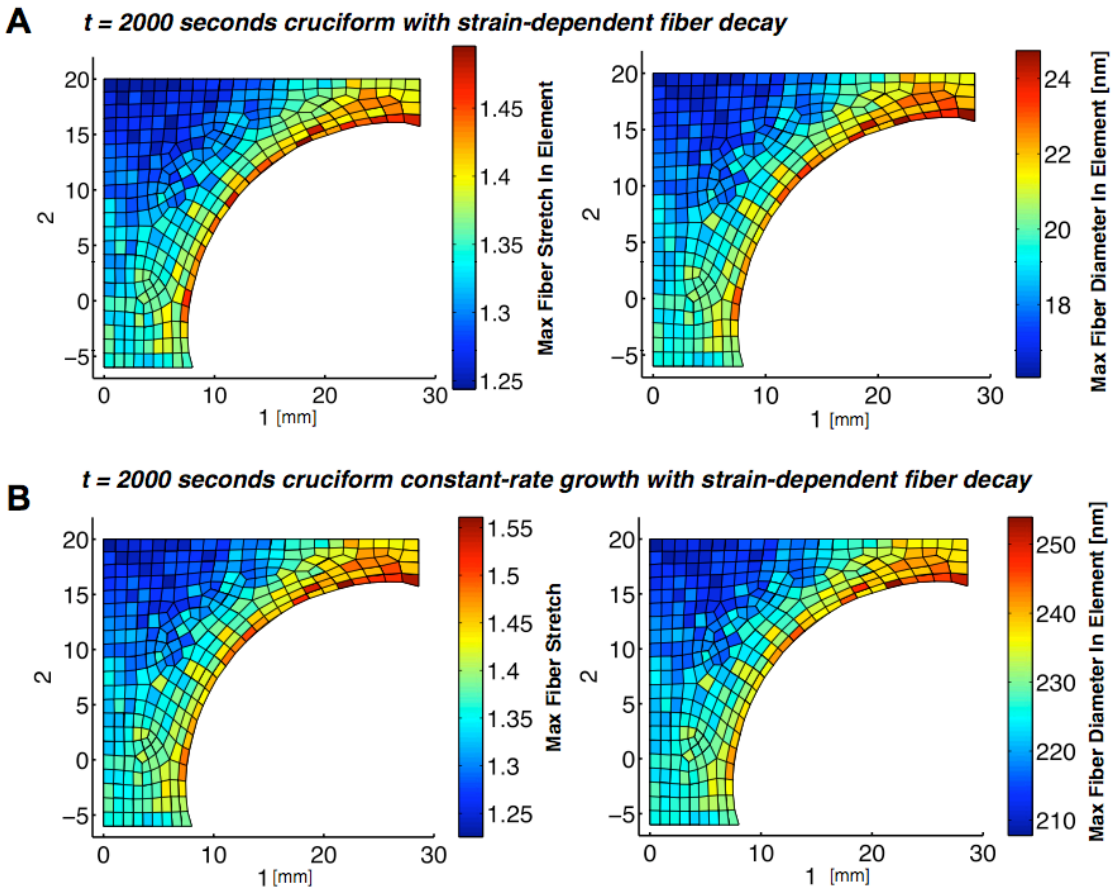

Fig. 2.7: Maximum fiber stretch per element as compared alongside the maximum fiber diameter per element for the (A) decay only and (B) constant-rate growth (k3=0.10 nm/sec) with strain-dependent enzymatic decay case. In both simulations the sample is held at a 30% equibiaxial stretch. The initial fiber diameter for the model was 100 nm.

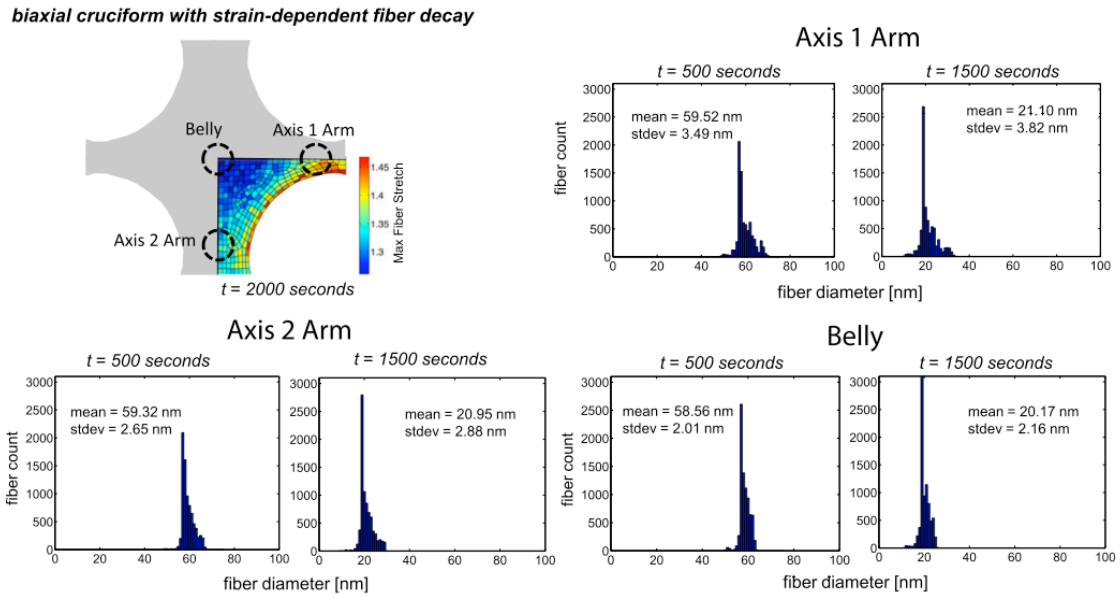

Fig. 2.8: Fiber diameter histograms for fibers sampled from elements in three distinct regions of the domain for the 30% equibiaxial stretch with strain-dependent decay case. Fibers were sampled at t = 500 and t = 1500 seconds. In each region, 8 individual RVEs were selected for analysis. The initial fiber diameter for the model was 100 nm.

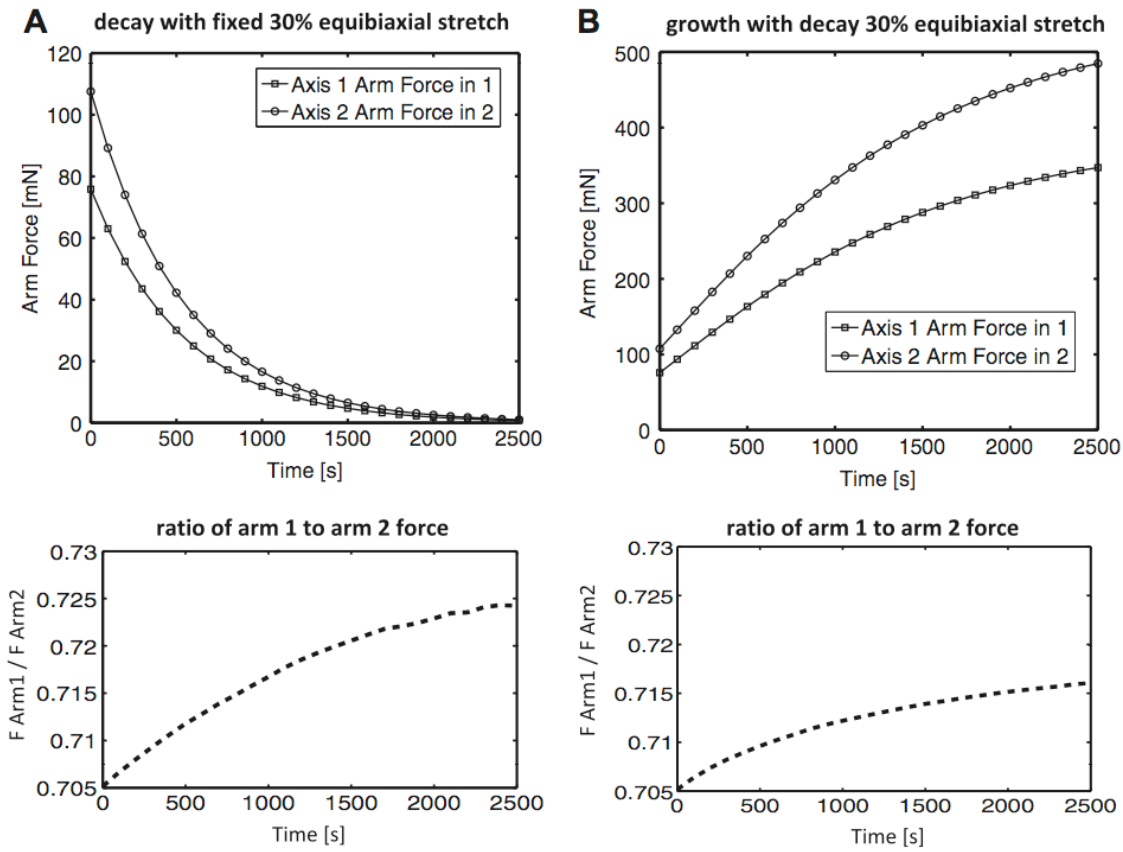

Fig. 2.9: The axis 1 and axis 2 arm forces plotted for the (A) decay only and the (B) growth with decay 30% equibiaxial stretch cases. The ratio between arm forces (F_{arm1} / F_{arm2}) is plotted for comparison.

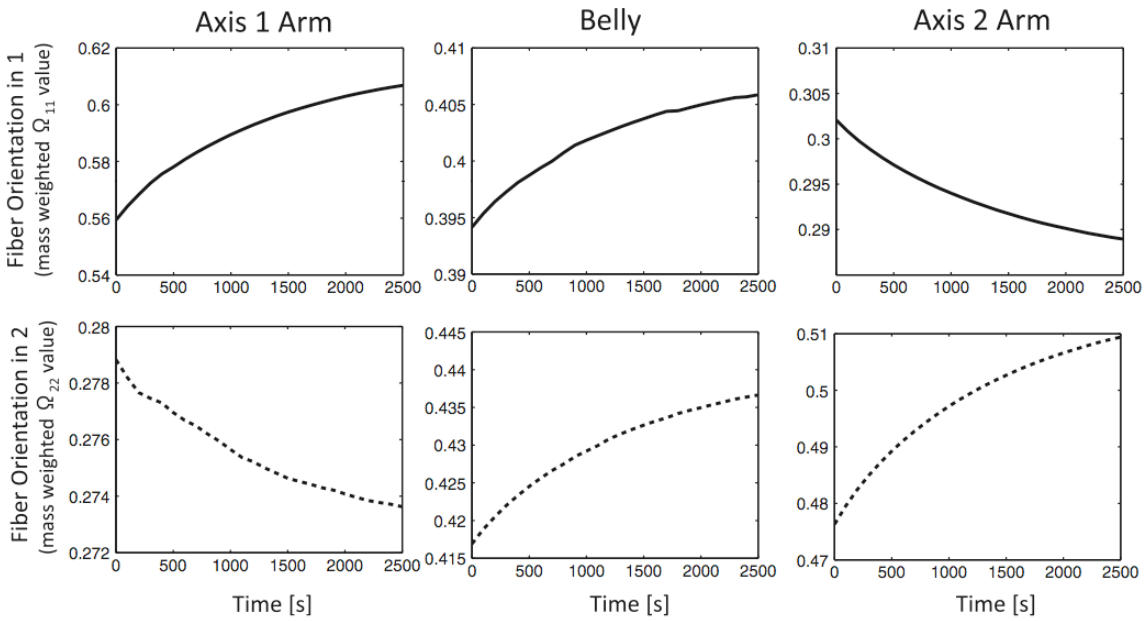

Fig. 2.10: Fiber orientation values (from the mass weighted orientation tensor) for three distinct regions of the cruciform in the 1 and 2 directions show localized changes in fiber alignment over time for the constant-rate growth and stain-dependent decay case for a constant 30% equibiaxial stretch. For comparison, a completely isotropic sample would have tensor orientation values of Ω_{11}= 0.33 and Ω_{22} = 0.33 in the 1-2 plane.

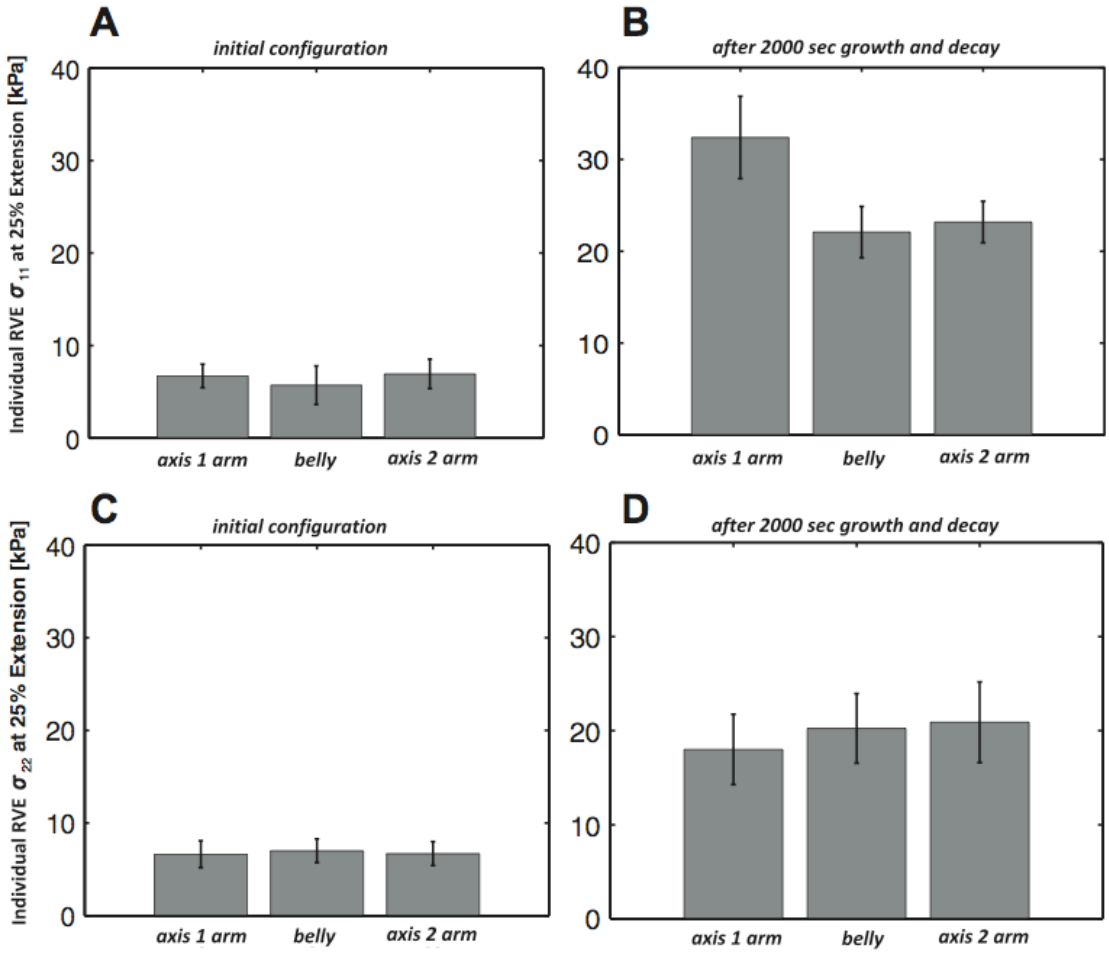

Fig. 2.11: For the equibiaxial extension with constant-rate growth with enzymatic decay case (A) σ_{11} stress for n = 3 RVEs extended individually 25% in 1 from their undeformed configurations in the initial state and (B) after 2000 seconds of growth and decay. In (C) σ_{22} stress for n = 3 RVEs extended individually 25% in 2 from their undeformed configurations in the initial state and (D) after 2000 seconds of growth and decay. The RVEs were sampled from the areas of the arms and belly of the biaxial sample pictured in Fig. 2.7. Columns represent the mean value, and errorbars express the 95% confidence interval for each mean.

3. Multiscale Model Predicts Tissue-Level Failure from Collagen Fiber-Level Damage

The content of this chapter was published as a research article in the *Journal of Biomechanical Engineering* by Hadi, Sander, and Barocas (Hadi et al., 2012b).

3.1 Introduction

Extracellular matrix proteins are assembled into complex hierarchical structures in a tissue-specific manner to provide tissue stability and to enable tissue function. When tissue-level forces exceed the physiological range, ECM components can be damaged, the stability of the tissue can become compromised, and the tissue can become non-functional. For example, in whiplash injuries, where abnormal head and neck kinematics produce excessive cervical facet deformation, painful microtears may develop in the cervical facet capsular ligament (Quinn and Winkelstein, 2011). Alternatively, pathological remodeling can lead to alterations in the tissue microstructure that progressively weaken it and make it susceptible to catastrophic failure. Such is the case with aortic aneurysms, where the stress in the aortic wall exceeds the local tissue strength and the vessel ruptures or dissects, often with fatal consequences (Phillippi et al., 2011). In both cases, there is a fundamental lack of understanding of how tissue-level loads are communicated to the ECM microstructure and lead to tissue damage and failure. Because of the lack of understanding of multiscale failure phenomenon, the biomedical

community is limited in its ability to prevent, diagnose, and treat soft tissue injuries and diseases of this nature.

To understand tissue failure better, several important models have been developed that incorporate aspects of the tissue microstructure, often through collagen fiber crimp, fiber orientation, and strain-based recruitment and failure distributions (De Vita and Slaughter, 2007; Hurschler et al., 1997; Liao and Belkoff, 1999; Wren et al., 2001). Although these models can describe failure phenomenon, they are constrained in their ability to provide insight into the mechanisms of failure because the description of the tissue microstructure is limited or essential elements such as fiber-fiber interactions and realistic fiber kinematics are absent. Others have focused on the importance of these elements as they relate to lung (Ritter et al., 2009), intermediate filaments in the cytoskeleton (Ackbarow et al., 2009; Keten et al., 2010), and non-biological materials (Sastry et al., 1998; Wang and Sastry, 2000), but those models are either two-dimensional or limited to the behavior of a single network. Zohdi has successfully modeled multiscale failure in regular lattices of biological fibers (Zohdi, 2007) and Ernst et al. (Ernst et al., 2010) have also explored multiscale fiber network failure (though in a non-biological context) using a regular unit cell with periodic boundaries. Most tissues are much more complex and display regional inhomogeneities in microstructure, fiber organization, and mechanical properties, such that the mechanical response of the tissue derives from the integrated deformation and distribution of load throughout the tissue ECM. Hence, for these types of tissues, any model predicated on mechanisms of local fiber failure must contain an explicit three-

dimensional description of the ECM microstructure and the spatial heterogeneity of the tissue. Recent studies support the need for this level of detail, as they report non-affine fiber reorganization (Billiar and Sacks, 1997; Gilbert et al., 2006; Lake et al., 2009) and regional variations in the mechanical behavior in response to load (Moger et al., 2009; Padala et al., 2010), including an example of complex relationships between the non-coincident locations of damage and strain (Quinn and Winkelstein, 2008).

To address these issues, we have developed a multiscale model that incorporates spatial heterogeneity and links the microscale failure of discrete collagen fibers to the macroscale material response of the tissue. We have initiated our development of a failure theory for soft tissues by examining failure mechanisms in a simpler system that shares some of the properties of native tissues – a reconstituted collagen gel. This model system has been used previously to understand multiscale mechanical interactions and to validate model predictions (Sander et al., 2009a; Sander et al., 2009b). In the current work, we apply a multiscale scheme to the question of mechanical damage and failure in reconstituted type I collagen gels. We have developed a multiscale model for damage that links the microscale failure of discrete collagen fibers to the macroscale material response of a collagen gel. First, we fitted the model to a series of uniaxial strain-to-failure experiments using a dogbone-shaped sample geometry. Next, we tested the model against an alternative geometry that varied by design – a notched dogbone in uniaxial extension – and gauged its ability in predicting experimental forces, strains, and fiber alignment. In

both portions of the study, we use the same collagen source stock for our gels, reconstituted to a specific protein density using the same protocol.

3.2 Materials and Methods

3.2.1 Multiscale Model

In our multiscale mechanical model (Fig. 3.1), representative volume elements (RVEs) comprised of discrete fiber networks determine the mechanical properties of a finite element (FE) continuum at each of its Gauss points (with eight Gauss points assigned to each element using tri-linear basis functions). Typically, RVEs are on the scale of 10-20 micrometers whereas the FE domain spans several centimeters. A unique, randomly generated RVE network was assigned to each element in the model. This model has been successfully used to simulate a range of materials (Chandran and Barocas, 2007; Sander et al., 2009b; Stylianopoulos and Barocas, 2007). The method by which macroscale strain is coupled to microscale stress within the model has been described previously (Chandran and Barocas, 2007). Briefly, macroscale deformations are mapped to deformations of microscale RVE boundaries. The RVE network rearranges and stretches in response to the boundary deformation, generating a volume-averaged stress at each Gauss point within each finite element. The macroscale deformation that balances stress within the continuum is then determined iteratively.

Several governing equations were used in the model to couple macroscale and microscale displacement, force, and stress. The continuum force balance based on the volume-

averaged stress from RVE deformations is given by (Chandran and Barocas, 2007):

$$\sigma_{ij,j} = \frac{1}{V}\oint_{\partial V}(\sigma_{ij}^{L} - \sigma_{ij})u_{k,i}n_k dS \quad (3\text{-}1)$$

In this equation σ is the macroscale averaged Cauchy stress, σ^L is the local microscale stress, V is the RVE volume, n is the normal vector to the RVE boundary, u is the displacement of the RVE boundary, and index notation is employed. The RVE volume-averaged Cauchy stress was calculated via the equation (Chandran and Barocas, 2007):

$$\sigma_{ij} = \frac{1}{V}\int_V \sigma_{ij}^{L}\, dV = \frac{1}{V}\sum_{bc} x_i f_j \quad (3\text{-}2)$$

In this equation bc is the set of all RVE boundary fiber cross-links, x is the boundary fiber cross-link coordinate, f is a component of the force acting on the boundary fiber cross-link, σ is the macroscale averaged Cauchy stress, σ^L is the local microscale stress, and V is the RVE volume. The collagen density of all experimental samples (1.8 mg/ml) was matched exactly in the multiscale model by using the method outlined in (Stylianopoulos and Barocas, 2007) which allowed for the accurate unitization of the mechanical stress-strain response of RVE networks. All model simulations were run on a 32-core parallel cluster at the Minnesota Supercomputing Institute with wall times between 10 and 12 hours.

3.2.2 Microscale Network Damage

At the microscale, networks consist of assemblages of nodes and fibers within a unit cube. Nodes are freely rotating and freely displaced pivots between fibers. Fibers are nonlinear springs with the force along the axis of stretch governed by the nonlinear constitutive equation:

$$F_f = \frac{E_f A_f}{B}(\exp[B\ \varepsilon_G] - 1) \quad \text{with} \quad E_f \approx 0 \text{ for } \lambda_f > \lambda_{crit} \tag{3-3}$$

where F_f is the resultant force along a fiber, E_f is the Young's modulus for a fiber at infinitesimal strain, A_f is the fiber cross-sectional area, ε_G is the fiber Green strain, B is a fitting parameter, λ_f is the fiber stretch, and λ_{crit} is the critical fiber stretch value at which damage is triggered. The constitutive equation was adapted from a previous model by Billiar and Sacks (Billiar and Sacks, 2000) for the pre-failure mechanics of a collagenous tissue and the equation has been previously used successfully in multiscale models to capture the mechanical deformation (from small and large strains) of collagen tissue analogs (Lai et al., 2012; Sander et al., 2009b). The cross-sectional area, A_f, for fibers was calculated based on a diameter of 100 nm as seen recently in the work of Lai et al. (Lai et al., 2012) who performed scanning electron microscopy on reconstituted type I collagen gels and this diameter is also on the same scale as previous related studies (Sander et al., 2009b; Stylianopoulos and Barocas, 2007). Networks were created from Delaunay tessellations of a set of random points that were originally created in a 2-unit cube and then clipped from the center to produce a 1-unit cube in order to avoid edge effects.

Networks had a mean of 456 fibers with a standard deviation of 48 fibers. The chosen number of fibers per RVE network is on the same scale as previous studies using our multiscale model that successfully captured the mechanics of similar collagen gel tissue analogs (Sander et al., 2009b; Stylianopoulos and Barocas, 2007). The chosen topology of networks (as constructed from Delaunay triangulations) was previously compared to alternative topologies of lower nodal degree (Sander et al., 2011) in uniaxial strain to failure dogbone simulations and the chosen topology was found to be the best match for experimental outcomes. The model and experimental fiber alignment was initially isotropic in the undeformed configuration (confirmed via polarized light microscopy and then input into the model using isotropic RVE networks) for all simulations considered. Collagen fiber alignment changes can be compared relative to this initial starting point for both model and experiment. Since each macroscale element contains a unique fiber network at each of its eight Gauss points (and simulation FE meshes consisted of several hundred elements) the physics of approximately 1 to 2 million discrete microscale fibers were tracked in each simulation run necessitating the use of supercomputing resources. The small-strain modulus, E_f, of a fiber within the network was reduced by ten orders of magnitude (to achieve a near-zero mechanical contribution) if the fiber exceeded a critical stretch value, λ_{crit}. This method of implementing damage effectively removed the mechanical contributions of the failed fiber within the network but preserved network topology. This failure model could potentially represent the failure of a fiber or of a fiber-to-fiber cross-link. Fibers were damaged at the end of each macroscale displacement step of 0.10 mm, selected as the minimum displacement step necessary to produce convergent

simulation results via trial and error. Fibers are allowed to stretch and rotate in each microscale network within the model (allowing for material reorientation and rearrangement) at each displacement step within the multiscale simulation. All intact fibers in each microscale network are load bearing (not only fibers that span the RVE) and all intact fibers play some role in contributing toward the single volume averaged stress calculated for each RVE in the model. However, fibers are connected to one another only through their original nodal linkages (topology is preserved) within each RVE network and fibers do not form new linkages during the course of the simulation, but rather pass through one another, limiting the manner in which fibers redistribute and interact in the model.

3.2.3 Collagen Gels

Type I collagen gels were reconstituted from a stock solution of 2.2 mg/ml acid solubilized type I bovine collagen (Organogenesis, Canton MA) with a final concentration of 1.8 mg/ml using a similar protocol described previously (Sander et al., 2009a). A solution containing 1M HEPES (Sigma, St. Louis MO), 1M NaOH (Sigma, St. Louis MO), and 10X MEM (Mediatech, Manassas VA) was used to reconstitute the gels. Gels were cast into molds of two different geometries – dogbone and notched (Fig. 3.1) each with distinct dimensions – and incubated at 37° C for approximately 14 hours prior to testing. Natural fiber scouring pad strips (3M, St. Paul MN) were used as sample anchors in each mold (the gels infiltrate the anchors at casting) and were inserted into molds prior to the addition of the reconstituted gels to facilitate gripping for uniaxial

extension. Spring-loaded sandpaper grips were then used to attach the anchors directly to the testing apparatus, alleviating the need to make contact with or apply direct forces to the actual collagen gel sample.

3.2.4 Mechanical Failure Experiments and Simulations

A series of uniaxial stretch-to-failure experiments were conducted. The gels were tested in two different geometries: dogbone (n=5) and notched (n=5). Experiments were conducted on a low-force planar mechanical tester (Instron, Norwood MA) in the University of Minnesota Tissue Mechanics Lab. Gels were tested to failure using a chosen grip displacement rate of 0.05 mm/sec to elicit a quasistatic force-strain response from samples. The mechanical tester was operated under displacement control at all times. A digital video camera fitted with a 105 mm macro lens (Canon USA, Lake Success NY) was used to image a selected sample of the notched geometry (speckled with Verhoeff's stain) for optical strain tracking via a custom digital image correlation method previously described in (Raghupathy et al., 2011). Briefly, the strain tracking method relied on the analysis of a series of still images captured from the filmed experiment using a custom code that applied an iterative Newton-Raphson method for pixel displacements based on the work of (Pan et al., 2009). The collagen fiber alignment in a selected notched geometry sample was also imaged during experiments using quantitative polarized light microscopy (Sander et al., 2009a; Sander et al., 2009b; Tower et al., 2002). Experimental fiber alignment was quantified using a custom code that analyzed sample images generated using a specialized optical train consisting of a series

of polarized light filters (Tower et al., 2002). Two separate samples were chosen for either strain analysis or for fiber alignment since we are unable to simultaneously capture both material parameters with our experimental methods. The grip forces and displacements for the dogbone geometry were used to fit key parameters (E_f, the fiber small-strain modulus, B, a non-linear fitting parameter, and λ_{crit}, the critical fiber stretch for damage) within our static (time-independent) multiscale damage model. Parameters were fit in series by first fitting the macroscopic failure stretch via the critical fiber stretch parameter, next the fiber modulus was fit, and then last, the fiber nonlinear fitting term was fit via a trial and error approach to minimize computational resources expended. The same parameter values were then used to simulate the notched test for comparison against the experimental findings. Several notched test simulations were run (n=3), each using a unique set of RVE fiber networks and with the same key parameters fit from the dogbone geometry. All fibers within the model were assigned the same material parameters. However, since the network assigned to each element in the model is randomly generated and unique, the effective material properties compared across all elements included some variance.

3.3 Results

3.3.1 Dogbone Experiment and Model Fit

Five dogbone samples were loaded to failure, each demonstrating some yielding before failure (Fig. 3.2). Model parameters (critical fiber failure stretch $\lambda_{crit} = 1.42$, unitless non-linear fitting parameter $B = 0.25$, and small-strain fiber modulus $E_f = 7.4$ MPa) were

determined so that the model peak force and strain at peak force were coincident with the experiment. Using these parameters, the model matched the loading response within the 95% confidence interval for grip force over the entire sample stretch range (Fig. 3.2), although the model did not demonstrate yielding, and the grip force was generally slightly lower than the mean values observed experimentally. By design, material failure and the bulk of the deformation occurred in the gauge region, defined as the interior region of the dogbone sample consisting of the area encompassed by the two parallel edges within its center. At peak force, the model stretch between the grips was 1.29 as compared with a maximum single element stretch of 1.61. Elements in the flared regions near the grips experienced little stretch in comparison.

A small population of adjoining elements within the gauge region was responsible for the loss of mechanical integrity within the sample (Fig. 3.2). A specific region of localized elements (which laterally spanned the sample in the center gauge region along two bands of contiguous elements transverse to the direction of loading) experienced the greatest loss of fibers and incurred the greatest element stretches (Fig. 3.3). The rapid stretch in this region allowed for the retraction of sample regions largely populated by unfailed fiber networks as catastrophic damage ensued. For all of our current and previous dogbone failure simulations these regions (Sander et al., 2011) have arisen and expanded within the gauge region of the sample. Fiber networks within these elements lost percolation (Fig. 3.4) (e.g. there was no connected fiber path across network faces) along the axis of stretch and experienced a maximum of 85.4% fiber failure at the end of the

simulation as compared with a mean of 4.36% across all elements (Fig. 3.5). The majority of elements, 61.5%, experienced no fiber failure during the simulation. Fibers that were left intact in non-percolating networks were found in unconnected clusters attached to RVE network faces or were contained in isolated fiber islands. Fibers in non-percolating networks were analyzed following catastrophic failure in the dogbone sample (at a grip-to-grip macroscopic sample stretch of 1.36) and fibers were distributed according to the mean fiber orientation tensor Ω (as defined in a previous study (Stylianopoulos and Barocas, 2007) that utilized fiber networks) with diagonal terms [Ω_{11} Ω_{22} Ω_{33}] equal to [0.35 0.32 0.33], indicating that remaining intact fibers were not simply arrayed orthogonal to the axis of extension and likely retracted upon the failure of the majority of fibers within the network. For context, all networks were initially isotropic on average with a mean fiber orientation tensor Ω containing diagonal terms [Ω_{11} Ω_{22} Ω_{33}] equal to [0.33 0.33 0.33] throughout the system before any strains were applied. It is important to note that while we have plotted distributions of intact fibers and network percolation within the model at different simulation points, we are unable to investigate the actual microscale deformation of the experimental collagen fiber network with our current experimental setup to compare against simulated results.

In the simulation, the single element with the largest Cauchy σ_{11} stress at peak grip force (loaded in axis 1) was not contained within the element set that experienced the greatest fiber failure and which subsequently lost mechanical integrity over the sample stretch (Fig. 3.6). Instead, elements that experienced the greatest strain along the axis of loading

at peak grip force (and after) were elements where macroscale failure initiated within the gauge region of the sample. Elements coincident with peak strain during the simulation also experienced the greatest loss of collagen fibers at the microscale. In all of our previous multiscale simulations of failure in dogbone samples (Sander et al., 2011), failure has taken place in the gauge region of the sample geometry regardless of networks selected for the model. In the present study we have not considered the role of stochasticity in the dogbone simulation case. Rather, the role of independent simulations with unique networks (n=3) was considered in the case of the notch validation simulations. A bimodal distribution of element stretches along the axis of loading arose near the moment of peak grip force (as one population of elements had largely failed while another population of elements was left largely intact) as particular elements already began to experience stretches that were 35% – 40% greater than the mean element stretch (Fig. 3.7).

Since RVE networks were generated randomly and were on average isotropic but included some variance in their mechanical stiffness, we calculated the tangent modulus of all networks used in the simulation at large deformations (using a uniaxial stretch of 1.4 for each network) to see if this statistic played a role in macroscale failure. Elements in the gauge region containing networks with the largest tangent modulii were, unsurprisingly, not coincident with regions of greatest strain and greatest fiber failure in the model. However, elements which contained networks with the smallest tangent modulii values did not experience the greatest strains or the greatest fiber failure in the

model, suggesting that while tangent modulii plays some role in framing damage within the model, there is an interplay between overall macroscale kinematics, network stiffness, and network variation that leads to catastrophic failure within the multsicale system.

3.3.2 Notched Dogbone Experiment and Model Predictions

For the failure of samples in the notched geometry simulated with fitted parameters from the dogbone geometry, we found that the predicted forces fell within the 95% confidence interval for all grip forces above a sample stretch of 1.08 (Fig. 3.8). In this case, the predicted grip forces were generally higher than those of the experiment, which featured a shallower toe region as compared to the dogbone experiment. The mean peak simulated force and the mean stretch at peak force fell within 15% of the experimental values. Failure in the simulated notch case, similar to failure experiments with notched collagen gels, was characterized by a propagation of the stress concentrator through the axis perpendicular to the direction of stretch.

At the end of the notch simulation, only 10.0% of elements had experienced fiber failure as compared to 38.5% for the dogbone case. Elements experiencing fiber failure were concentrated along a path parallel to the crack tip (Fig. 3.9). The maximum fiber failure percentage for these elements was 89.8%. At the mean peak simulated force, the grip sample stretch along the axis of extension was 1.17 was compared to an average stretch of 1.30 in the central region spanning the notch, though the maximum element stretch was 2.08 near the notch tip.

Percolation in RVE networks across the axis of stretch was lost for elements for the dogbone and notched case only after the peak force for these simulations was reached. 89% of elements that lost percolation along this axis had lost greater than 45% of their fibers during the simulation (Figs. 3.10 and 3.11). Only 5 of 312 elements for the notch geometry lost percolation while 21 of 473 elements lost percolation in the dogbone geometry. It is important to note that in both the notch and dogbone simulations all RVE networks were similarly generated and began as initially percolating and isotropic, with the notch modeled in the macroscale FE mesh of the simulation, not through any microscale RVE network alterations. The loss of percolation in elements was characterized by a sharp drop in the grip force for each simulation, leading to a catastrophic loss of mechanical integrity.

Simulated outcomes for the strain field and fiber alignment at peak grip force were also compared to the experimental case (as measured by digital image correlation) for the notched geometry (Fig. 3.12). Qualitatively, areas of greatest strain in the sample corresponded between simulation and experiment, centering at the notch tip. Discounting elements whose networks contained a majority of failed fibers, the peak Green strain components in the direction of extension near the notch tip fell within 0.3 and 0.5 for the model and experimental case. Fibers became highly aligned in the experimental case (as measured by quantitative polarized light microscopy) along the axis of stretch over the unnotched region of the sample. Fibers were left relatively unaligned in regions along the

axis of stretch through the notched region of the experimental sample. This trend was also seen in the simulated case, but there was greater realignment of fibers along the edges of the notch perpendicular to the axis of stretch. There was also less variation in alignment along the unnotched portion of the experimental sample as compared with the simulated result.

3.4 Discussion

The model may be a useful tool in predicting the macroscale failure conditions for engineered tissue analogs in complex geometries based either on fitted values from simple experimental geometries or from experimentally derived microstructural values for fiber failure. For our collagen gel model, we were able to demonstrate that a fiber-based rule (at the micrometer scale) for discrete failure could strongly shape the macroscale failure response of the gel (at the millimeter level). The agreement between the model and the experiments demonstrates the ability to predict tissue-level events based on a microstructural model. The systems studied were relatively simple in that the samples were of uniform collagen density and were initially isotropic. The extension to more complex geometries and architectures, however, as arise in native tissues (Quinn and Winkelstein, 2008; Sacks et al., 2009) and bioengineered tissues (Pins et al., 1997; Robinson and Tranquillo, 2009), would be difficult to model at the tissue scale without an underlying structural description. A major advance of the current work is the potential to accommodate regional structural variation without requiring a change in the failure criteria.

In order for us to realize that potential, however, a better understanding of fiber-level failure mechanisms is needed. One might well argue that we have replaced the intractable problem of modeling failure at the tissue level with the merely difficult problem of modeling it at the fiber level. The current work used the simplest possible failure model – no damage until a critical strain is reached, at which point the fiber fails catastrophically – which is appropriate for a single strain-to-failure experiment as performed here, but would not be able to capture a fatigue mechanism in which repeated loading cycles contribute to the failure of the tissue. Advances in single-collagen-fiber mechanical analysis (Shen et al., 2008) are steadily increasing our understanding of fiber behavior and will be particularly informative on this point. Direct comparisons to previous studies of single-fiber failure in type I collagen (both experimental and simulated) while useful for context, are limited by differences in fiber diameter, intrafibrillar cross-linking, hydration, and collagen source. Shen and others (Shen et al., 2008) experimentally strained type I collagen fibrils (native to sea cucumbers with diameters ranging from 150 to 470 nm) uniaxially and observed a mean yield stretch of 1.21 ± 0.13 with observed fiber failure occurring over a broader range with select fibers stretching well beyond this range without failure. Buehler (Buehler, 2006) has predicted, using purely atomistic modeling, tropocollagen molecule (subfibrillar) failure stretches between 1.4 and 1.6 via reactive force modeling. Pins et al. (Pins et al., 1997) experimentally found failure stretches for uncrosslinked reconstituted type I collagen fibers ranging from approximately 1.2 to 1.7 for much larger hydrated diameters falling

between 120 and 330 μm. Our chosen fiber failure parameter of 1.42 for all of our simulations falls within the range as these previous findings for fiber-level or sub-fiber-level failure stretch values. However, since fiber failure in our model may represent either the mechanical failure of fibers or potentially the failure of fiber-to-fiber linkages, direct comparisons are elusive. The small variance in our simulated outcome for the notched geometry (measured via the simulated grip force or sample stretch) relative to the experiment suggests that we may need to consider the possibility of stepped fiber failure or that we need to include greater variability in our model networks (perhaps by utilizing fiber diameter distributions) or by employing probabilistic rules for fiber failure. Furthermore, better understanding of network structure, and of what parameters are needed to characterize the network structure and to develop realistic network geometries (Stein et al., 2010), is also necessary to strengthen the model.

There is a growing body of work exploring the role of network structure in damage. Important two-dimensional examples include the work of Bates et al. on elastic fiber networks in the lung (Bates, 2007; Maksym et al., 1998) and Buehler et al. (Keten et al., 2010) on protein networks, all of which used structured networks with random variations in fiber properties to capture variability. Suki et al. have successfully used a zipper network model to add context to their experimental findings on the failure of engineered extracellular matrices (Black et al., 2008). However, none of these studies, nor any other to our knowledge, have linked subfailure microscale damage to the macroscale failure properties of tissue analogs as we have demonstrated in the present study. The analysis of

the loss of percolation in the three-dimensional Delaunay networks employed in our model also adds to existing work on quantifying percolation thresholds for various instances of Delaunay triangulation lattices such as the recent study by Becker and Ziff (Becker and Ziff, 2009) that numerically calculated an edge percolation threshold between 0.33 and 0.35 for two-dimensional random Delaunay lattices. In our three-dimensional networks, we find that when a fraction of nearly 0.55 fibers (edges) are connected in mechanical networks extended along a single axis, in most instances, percolation is preserved along the same axis.

Finally, we note that most tissues involve multiple fiber networks (e.g., fibrin and collagen) and/or a significant quantity of non-fibrillar macromolecules (e.g., proteoglycans), which could be extremely important in understanding the failure and subfailure behavior of a tissue. Gross tissue failure obviously must include failure of all components and might reasonably be expected to include (and, in many cases, be dominated by) the failure of a collagen network, but subfailure damage may well involve other components in non-obvious ways.

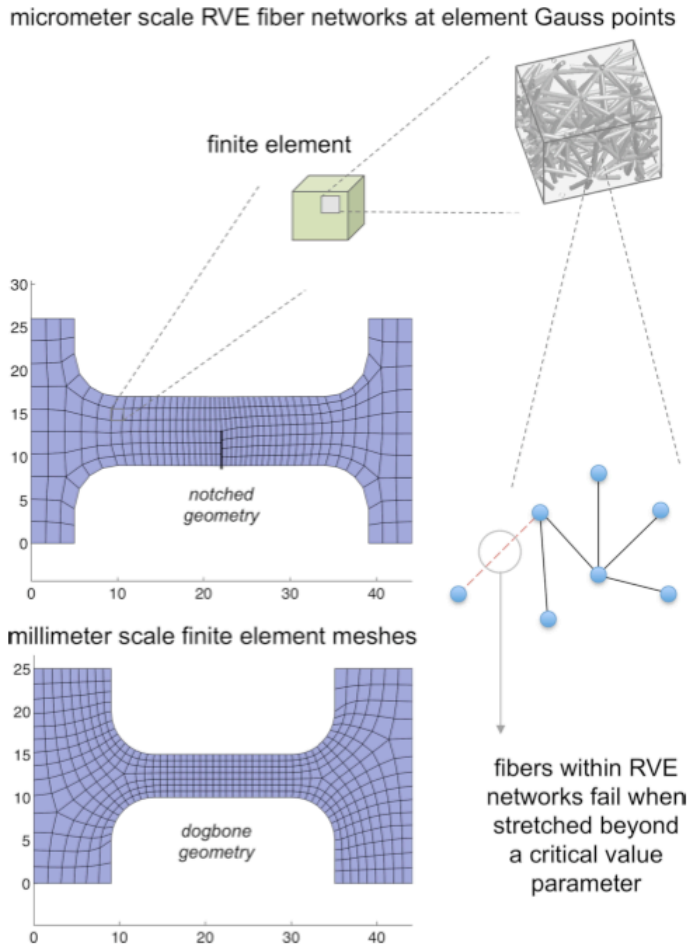

Fig. 3.1: Overview of the damage model used in the multiscale simulations. The dogbone domain, which exists on the scale of millimeters, is represented with a 3D finite-element (FE) mesh. Within each hexahedral element are eight microscopic fiber networks (RVEs) centered at the Gauss points that govern the stress-strain response of the element. As the FE domain stretches, interconnected fibers in the networks stretch and reorganize to satisfy force equilibrium. Fibers that exceed the critical fiber stretch ratio are effectively removed by reducing their modulus by ten orders of magnitude.

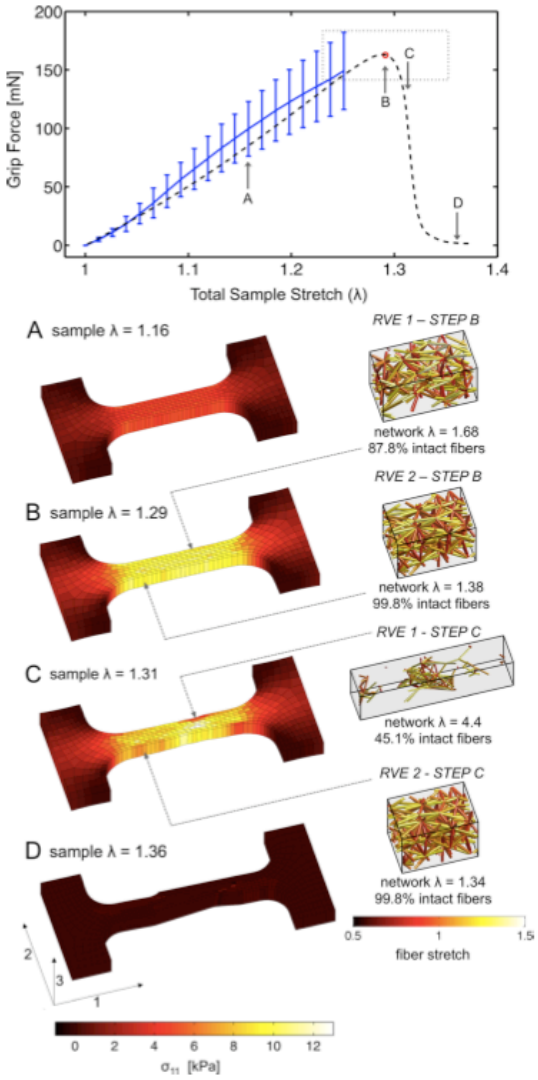

Fig. 3.2: Dogbone sample: comparison of the grip force against the total sample stretch (λ) for the experiment (solid line ends at first sample failure) and model (dashed line). Error bars represent the 95% confidence interval for the experimental mean (n=5). The quadrant defined by the dotted lines represents the 95% confidence interval for the peak experimental force and the 95% confidence interval for the experimental strain at peak force. The center of the quadrant is marked with a circle. The macroscopic stress in the model for select points (*A–D*) along the graph is depicted. Two fiber networks illustrating regional differences in the failure mechanics are shown.

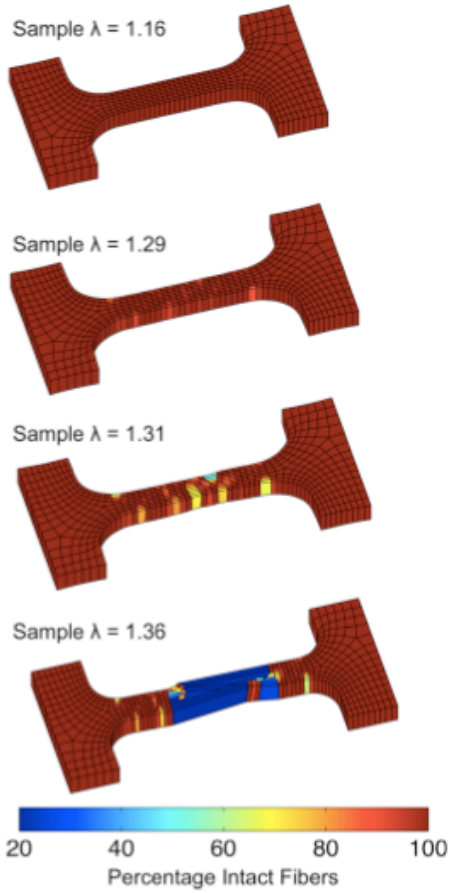

Fig. 3.3: Percentage of intact fibers per element varies at different grip-to-grip sample stretches (λ) for the model dogbone geometry. Percentage of intact fibers were averaged over all RVE networks within each element.

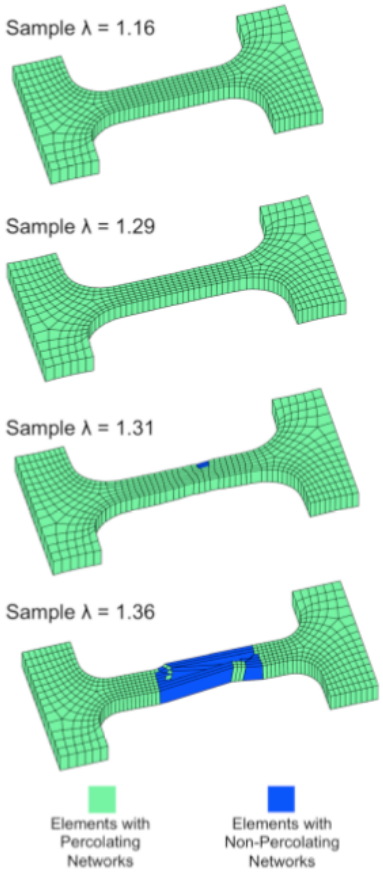

Fig. 3.4: Elements with non-percolating networks frame areas of damage for the modeled sample at different grip-to-grip stretches (λ) for the dogbone geometry. A percolating RVE was defined as a network that contained a connected fiber segment that spanned both RVE faces normal to the axis of loading.

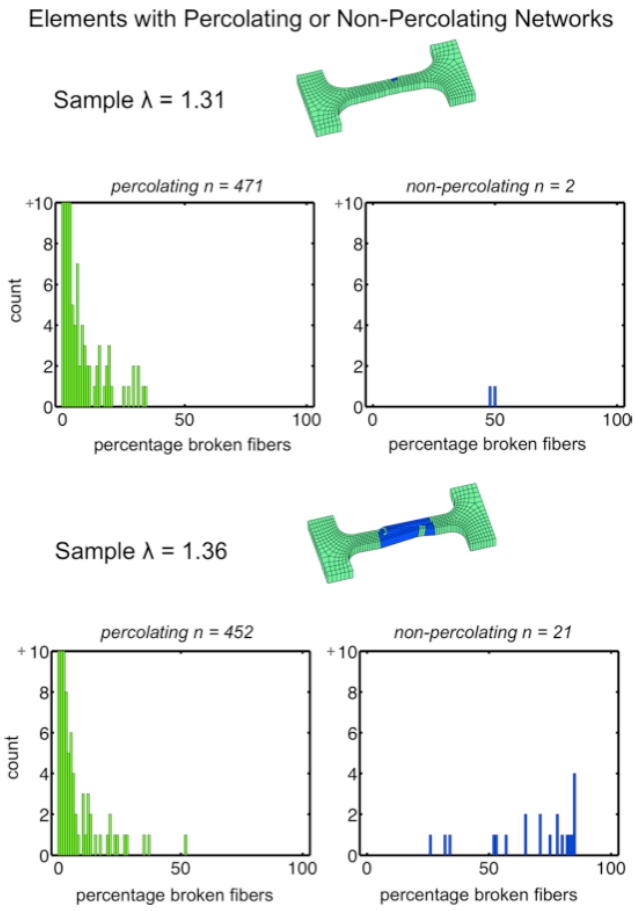

Fig. 3.5: Comparison of broken fiber percentages in elements with and without percolating RVE networks at different grip-to-grip stretches (λ) for the dogbone geometry.

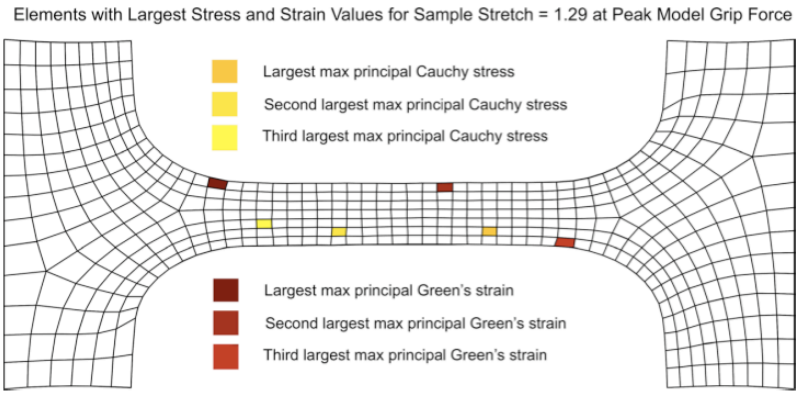

Fig. 3.6: The peak max principal Cauchy stress and the peak max principal Green strain for the dogbone geometry plotted over the deformed finite element mesh at the point of greatest grip force in the model.

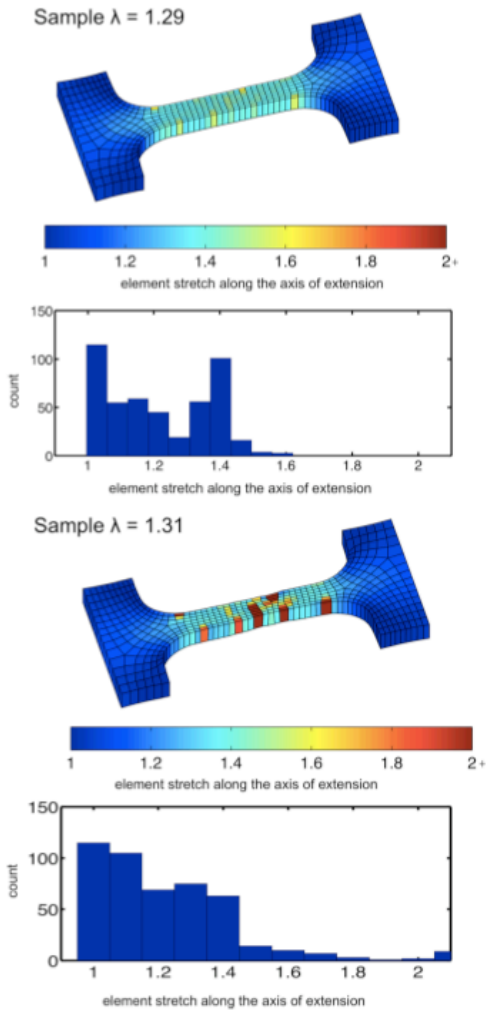

Fig. 3.7: Element stretch (along the axis of extension) plotted over the deformed mesh for the model dogbone geometry. The element stretch is also represented via corresponding histograms at a given sample stretch (λ) for the dogbone geometry.

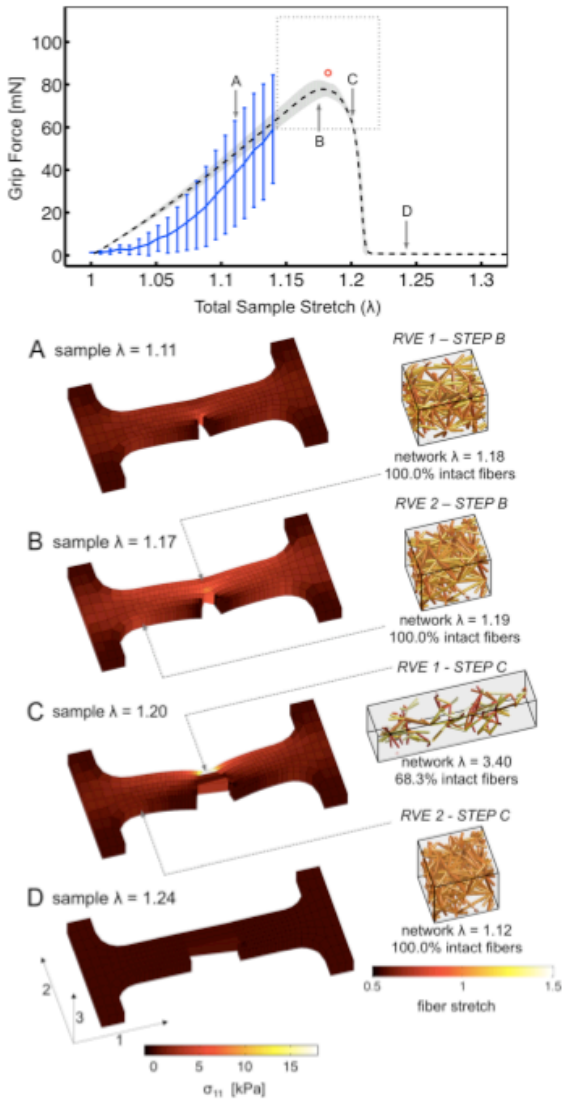

Fig. 3.8: Notched sample: comparison of the grip force against the total sample stretch (λ) for the experiment (solid line ends at first sample failure) and model prediction (dashed line is the mean result and shaded area represents the 95% confidence interval for n=3 independent simulations). Error bars represent the 95% confidence interval for the experimental mean (n=5). The quadrant defined by the dotted lines represents the 95% confidence interval for the peak experimental force and the 95% confidence interval for the experimental strain at peak force. The center of the quadrant is marked with a circle. The macroscopic stress in the model for select points (*A–D*) along the graph is depicted. Two fiber networks illustrating regional differences in the failure mechanics are shown.

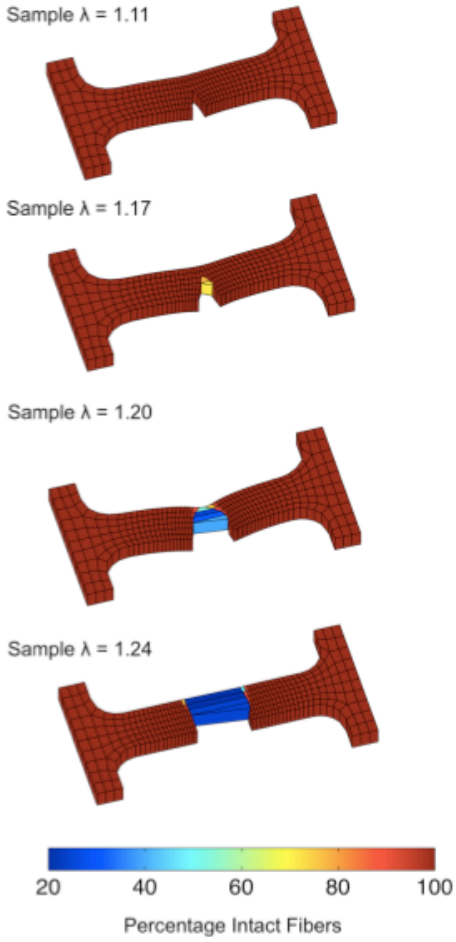

Fig. 3.9: Percentage of intact fibers per element varies at different grip-to-grip sample stretches (λ) for the notched geometry model. Percentage of intact fibers were averaged over all RVE networks within each element.

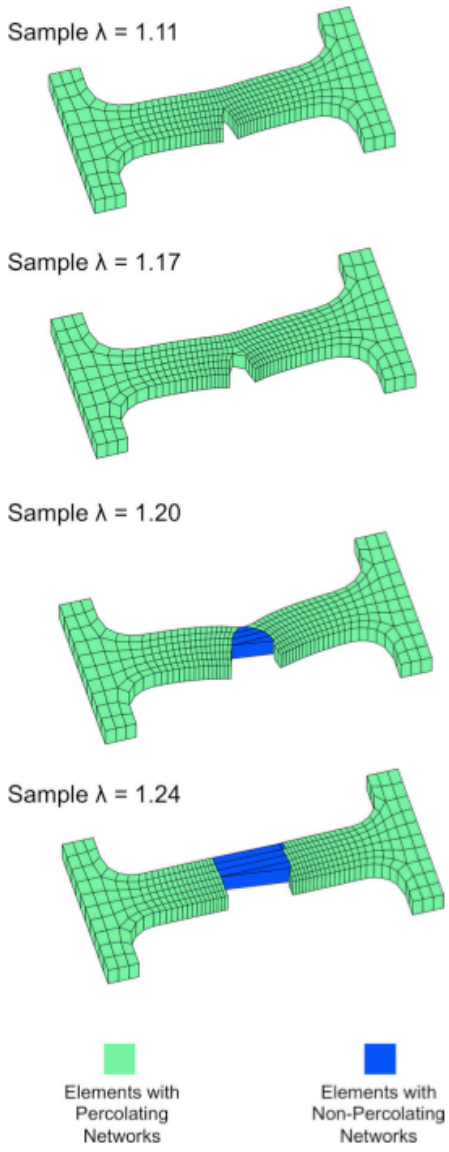

Fig. 3.10: Elements with non-percolating networks frame areas of damage for the modeled sample at different grip-to-grip stretches (λ) for the notched geometry. A percolating RVE was defined as a network that contained a connected fiber segment that spanned both RVE faces normal to the axis of loading.

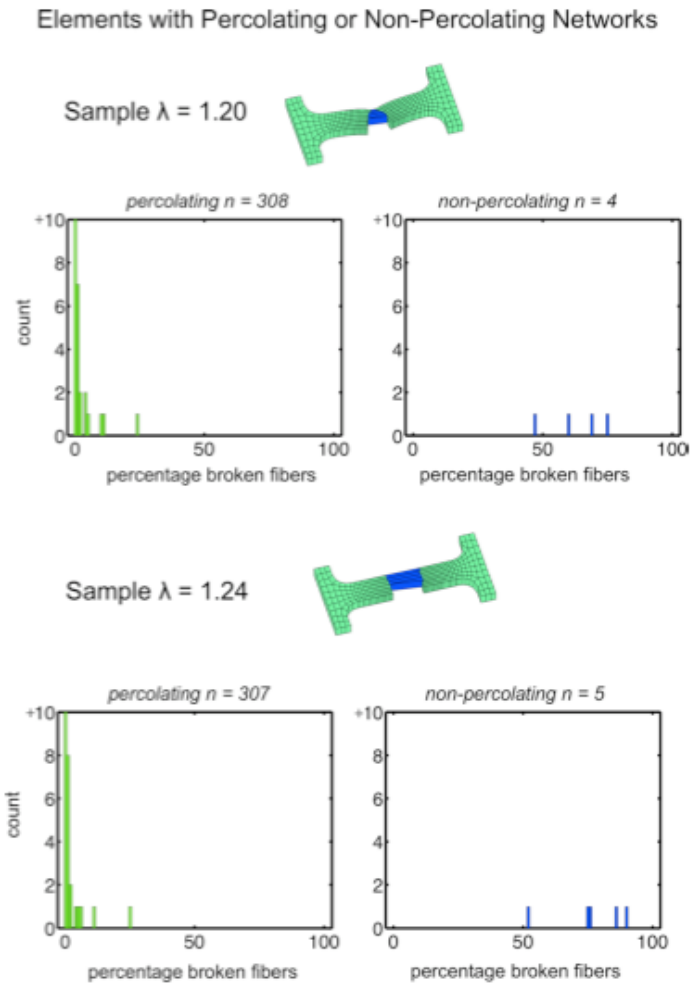

Fig. 3.11: Comparison of broken fiber percentages in elements with and without percolating RVE networks at different notched model grip-to-grip stretches.

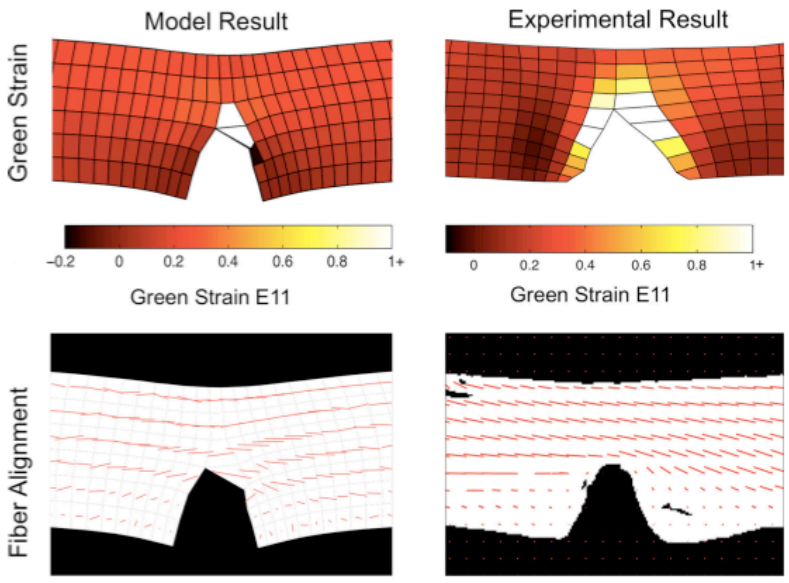

Fig. 3.12: Comparison of the model and experiment for the Green strain and collagen fiber alignment (alignment vectors normalized by maximum strength of alignment) at the point of peak grip force for the deformed notch geometry for two independent experimental samples.

4. Microscale Fiber Network Alignment Affects Macroscale Failure Behavior in Simulated Collagen Tissue Analogs

The content of this chapter was previously published as a research article in the *Journal of Biomechanical Engineering* by Hadi and Barocas (Hadi and Barocas, 2013a).

4.1 Introduction

The role of fiber architecture in soft tissue failure has been demonstrated by recent experimental (Anssari-Benam et al., 2012; Keyes et al., 2011; Quinn and Winkelstein, 2011) and computational (Ayturk et al., 2012; Hamed et al., 2012; Kao et al., 2011; Ritter et al., 2009) studies. Delineating the specific relationship between microstructure and macroscopic failure response in tissues, however, has proven to be a major challenge. Issues still remain with the non-affinity of fiber motion even in prefailure mechanics, making a more complex multiscale approach attractive and even necessary for certain problems (Hadi et al., 2012a) in spite of the additional computational demands.

Important work has been done in linking variations in microstructure to material failure in non-biological contexts, such as the work of Wang and Sastry (Wang and Sastry, 2000) on failure in random fiber networks and that of Zhang et al. (Zhang et al., 2010) on failure in fiber-reinforced plastics, but there has been a gap in the context of engineered and native tissues. As our understanding of the microstructural properties of healthy and diseased tissues continues to grow (Hang and Barber, 2011; Ito et al., 2005), we need

improved multiscale mechanical models for tissue damage and failure that can link microstructural variation to differing macroscale failure outcomes.

Towards this end, we recently adapted our multiscale finite element (FE) model of collagen gel mechanics to include failure of individual fibers within micronetworks (Hadi et al., 2012b), with that initial study demonstrating that the model can match experimental results in terms of force-displacement data and average fiber kinematics. In the current study, we explore how changes in model fiber network alignment lead to changes in the macroscopic behavior of the tissue.

4.2 Methods

4.2.1 Microscale Model

Our multiscale model consists of a macroscale FE continuum material linked to the mechanical response of microscale representative volume element (RVE) networks of discrete collagen fibers (which are allowed to fail when stretched beyond a critical value) situated at each Gauss point within the continuum (Chandran and Barocas, 2007; Stylianopoulos and Barocas, 2007). In the present study, we varied the microstructure of RVE fiber networks by changing their fiber alignment — both direction and degree of alignment — for a series of fiber failure simulations using a notched dogbone geometry.

Isotropic RVE networks of interconnected collagen fibers were created from the edges of Delaunay tessellations generated from a random set of seed points in a four-unit cube

(using a Matlab implementation of the Quickhull (Barber et al., 1996) algorithm) and then clipped to a unit cube to reduce boundary artifacts. Fiber alignment along one axis was generated by linearly scaling the coordinates of isotropic networks along that axis and then clipping to a unit cube. Rotation of networks was performed by coordinate transformation before clipping to a unit cube. Fibers were interconnected via freely rotating pin-joints at fiber-to-fiber nodes. For all simulations, networks contained a mean of 500–550 fibers, and a unique, randomly generated RVE network was used for each element within the model. All Gauss points for a given element used the same micrometer scale RVE network.

The force F_f acting along each discrete fiber within a collagen network was calculated as

$$F_f = E_f A_f (\exp(B \cdot \varepsilon_G) - 1) / B \qquad (4\text{-}1)$$

where E_f is the fiber small-strain tensile modulus, A_f is the fiber cross-sectional area, B is a nonlinearity parameter, and ε_G is the fiber Green strain (calculated as $(\lambda_f^2 - 1) / 2$). The constitutive equation was adapted from the work of Billiar and Sacks on the pre-failure mechanics of a collagenous tissue (Billiar and Sacks, 2000) and has been used previously to model a range of tissue analogs (Lai et al., 2012b; Lake et al., 2012a; Sander et al., 2009b). Damage was introduced at the fiber scale in our model by diminishing the fiber stiffness to a near-zero value when fiber stretch had exceeded a critical value. Once a

fiber had failed within the model, its modulus was irreversibly set to the near-zero value for the duration of the simulation.

The volume-averaged Cauchy stress σ_{ij} within each RVE was calculated as

$$\sigma_{ij} = \frac{1}{V}\int_V \sigma_{ij}^L \, dV = \frac{1}{V}\sum_{bc} x_i f_j \tag{4-2}$$

where *bc* is the set of all RVE boundary fiber cross-links, *x* is the boundary fiber cross-link coordinate, *f* is the force acting on the boundary fiber cross-link, σ^L is the local microscale stress, *V* is the RVE volume, and index notation applies. As was done previously (Stylianopoulos and Barocas, 2007), a scaling term for the microscale stress within the model adjusted for variations in RVE network length while maintaining the correct collagen volume fraction.

Fiber alignment within networks was quantified as

$$\Omega_{ij} = \frac{\sum L_{fiber} n_i n_j}{L_{total}} \tag{4-3}$$

where Ω is the fiber orientation tensor (Sander et al., 2009a; Sander and Barocas, 2009c), L_{fiber} is the length of a single fiber, *n* is the unit vector along the fiber, and $L_{total,}$ is the

total network length. By this measure, a completely isotropic network would have all diagonal components in the Ω orientation tensor comprised of $\Omega_{11} = \Omega_{22} = \Omega_{33} = 0.33$.

4.2.2 Macroscale Model

At the continuum scale, the force balance based on the volume-averaged stress from RVE deformations at each Gauss point was expressed as (Chandran and Barocas, 2007)

$$\sigma_{ij,j} = \frac{1}{V}\oint_{\partial V}(\sigma_{ij}^{L} - \sigma_{ij})u_{k,i}n_k \, dS \tag{4-4}$$

where n is the normal vector to the RVE boundary, and u is the displacement of the RVE boundary.

A notched dogbone macroscale FE mesh was used, consisting of 624 hexahedral elements with trilinear basis functions for a total of 5,792 microscale RVE networks (Fig. 4.1). The mesh was on the scale of several millimeters (44.0 mm in its longest axis) and was gripped statically at one end and stretched incrementally from the opposing grip to a stretch ratio of 1.5. A notched geometry was chosen based on its previous use in the damage model (Hadi et al., 2012b) and its ability to standardize the point of macroscopic failure within the model for each simulation.

4.2.3 Study Design

Degree and Direction of Alignment in Homogeneous Networks

Several simulations varying microscale fiber alignment and network rotation were run using the macroscopic notched dogbone stretched to failure along axis 1 (Fig. 4.1). Three types of network orientation were considered: isotropic (Ω_{11}= Ω_{22}= Ω_{33}=0.33), uniaxially aligned (Ω_{11}= 0.53, Ω_{22}=0.23, Ω_{33}=0.23), and transverse biaxially aligned (Ω_{11}= 0.43, Ω_{22}=0.13, Ω_{33}=0.43; the network is transverse isotropic in the 1-3 plane but is tested in the 1-2 plane). For each of the three cases, the network was also rotated 0º, 45º, and 90º around the 3-axis, producing a total of nine different cases to be analyzed.

Effect of Layering Networks and Merging Networks of Different Alignments

Two simulations of crisscrossed fibers with composite +45º and −45º rotated aligned networks were also run for comparison using either (a) the two-layer macroscale FE mesh with alternating layers (in axis 3) composed of networks rotated +45º in one layer and −45º in another layer or (b) merged RVE networks throughout the mesh which contained two populations of both +/−45º rotated fibers within each single network (Fig. 4.1). Prior to rotation (by either +45º or −45º relative to the extension axis 1) the mean network orientation tensor values for networks were Ω_{11}=0.6, Ω_{22}=0.1, and Ω_{33}=0.3. These composite models were then compared to the all +45º or all −45º rotated network cases for the notched dogbone failure simulation.

For all simulations, similar parameters from our previous study (Hadi et al., 2012b) were used: a fiber modulus (E_f) of 7.4 MPa, a fiber nonlinearity parameter (B) of 0.25, a collagen density of 1.8 mg/ml, a fiber stretch failure threshold (λ_{crit}) of 1.42, and a fiber

diameter of 100 nm (Lai et al., 2012b). Since there were almost 3 million unique fibers modeled in each of the simulations for the present study, a parallel computation strategy at the Minnesota Supercomputing Institute was employed using multiple processors to reduce computation time. Simulations were parallelized using 32 processors with wall times approaching 14–15 hours for each simulation case.

4.3 Results

4.3.1 Varying Alignment in Homogeneous Networks

At the macroscale, uniaxially aligned networks produced the greatest grip force prior to failure, followed by biaxially aligned networks and then by isotropic networks (Fig. 4.2a). The uniaxially aligned case, however, failed at the smallest grip displacement, followed by the biaxial case and then by the isotropic case, which failed at the largest grip displacement. Qualitatively, the general trend in the force-displacement response was similar for each case and included a monotonic rise in force, a sharp peak in the force, and then a rapid loss of grip force as the dogbone failed (Fig. 4.2a). At a fixed grip displacement of 7.0 mm, each case (uniaxial, biaxial, isotropic) generated different macroscopic stress fields (Figs. 4.2c–4.2e), though, as expected, the stress concentrated at the notch tip in all cases. The force-displacement plot for each case was integrated and the areas (signifying the mechanical work to produce the deformation) were compared (Fig. 4.2b). The work values followed the trend in peak force, with the uniaxial case generating the largest work and the isotropic case generating the smallest work under the force-displacement curve. However, whereas there was over a 50% difference between

the greatest and least peak force values, there was a smaller spread of approximately 25% between the greatest and least work values.

At the microscale, fibers in the uniaxial case experienced the sharpest rise and the largest peak value in mean fiber stretch plotted against the macroscopic dogbone grip-to-grip stretch (Fig. 4.3a). The isotropic case experienced the smallest mean fiber stretch and the most shallow rise in fiber stretch, and with the biaxial case bracketed between the uniaxial and isotropic cases. For this analysis, and for all subsequent analysis of the microscale fiber properties in our simulations, a subset of notch-adjacent elements was chosen (Fig. 4.3d) as a sample set. The biaxial case followed closely by the uniaxial experienced the largest loss of fibers over the failure stretch (Fig. 4.3b). The isotropic case experienced the smallest loss of fibers. Similar to fiber stretch, the uniaxial case also experienced the sharpest rise in mean fiber alignment parallel to the axis of extension (measured via Ω_{11}) but peaked at a smaller sample stretch as compared to the biaxial or isotropic cases (Fig. 4.3c). A single microscale network from the notch-adjacent element set was plotted to visualize differences among the different simulation cases at various grip displacements (Fig. 4.4). While the network initially appeared to deform uniformly across simulation type at a small grip displacement (3.0 mm), a displacement near the peak grip force value (7.2 mm) produced quite different outcomes based on network alignment. At 7.2 mm, the uniaxially aligned network had entirely failed (the collagen network no longer percolated across the axis of extension) while the biaxial network was

on the verge of failure, and the isotropic network lagged the other two alignment cases in terms of fiber stretch (Fig. 4.4).

After rotating these three network types (uniaxial, biaxial, isotropic) by 45º and 90º, we constructed interpolated contour plots of peak force, displacement at peak force, and mechanical energy (integral of the force-displacement curve) as functions of initial fiber orientation and network rotation (Fig. 4.5). The largest peak forces generated by the model occurred when fibers were aligned parallel to the direction of the extension. Conversely, the greatest strains at peak force occurred with networks that contained fibers largely oriented perpendicular to the direction of extension. The plot demonstrates that while the initial fiber network helps shape the overall failure response of the dogbone, rotation of networks can produce similar responses for different initial fiber alignments (Fig. 4.5).

4.3.2 Layering Networks and Merging Networks of Different Alignments

The model produced significantly different macroscale force-displacement responses by using either (a) all +45º or all −45º networks or (b) merged or alternating layers of +45º and −45º networks (Fig. 4.6a). Using alternating layers or merged networks produced the largest peak forces but at the smallest corresponding strains at peak force. Both the homogenous +45º and −45º cases produced smaller peak forces but at greater strains. The merged and alternating layer cases resulted in peak forces and strains at peak force that fell within 5% of one another, following qualitatively similar force-stretch trajectories.

The deformation work (area under the force-displacement curves) also varied relative to the peak force generated in each case, but as seen previously when comparing alignment, the relative spread in work was less than the spread in peak force values across simulation cases (Fig. 4.6b).

The macroscale deformation field also differed among the cases (Figs. 4.6c, 4.6d, 4.6e). In the alternating layer case, the deformation of the dogbone around the notch defect appeared largely symmetric. However, in the +45º and −45º cases, the deformation of the dogbone was clearly asymmetric around the notch defect. In the +45º case, greater element-wise deformation along the axis of extension (based on the E_{11} component of the element Green strain) occurred in the region in the (+) axis 1 direction relative to the notch. Conversely, in the −45º case, greater deformation fell in the (–) axis 1 direction relative to the notch. Notch failure appeared to propagate in a path roughly parallel to the alignment of the network relative to the direction of extension for the +45º and −45º off-axis alignments (Figs. 4.6f and 4.6g).

At the microscale, these four cases (+45º, all −45º, merged, or alternating layers) produced varying trends in mean fiber stretch, fiber failure, and in the Ω_{11} fiber orientation parameter (alignment along the axis of extension) as plotted against the macroscale stretch (Fig. 4.7). In terms of fiber stretch, the merged and layered cases produced the largest mean fiber stretches and the sharpest rise in fiber stretch, closely following each other along the entire macroscopic stretch. Both the +45º and −45º cases

lagged behind in terms of stretch magnitude and in the rate of increase in the fiber stretch but peaked at larger macroscopic stretches prior to failure as compared to the layered and merged cases (Fig. 4.7a). The merged and layered cases also showed a steeper rise in fiber loss as compared to the homogeneous cases, but the layered case appeared to lose approximately 20−25% fewer fibers over the stretch (Fig. 4.7b). The +45º and −45º cases lost fibers at similar rates over the sample stretch. The greatest microscale differences between the homogeneous (+/−45º networks) and composite cases (layered or merged networks) appeared in comparisons of the change in the Ω_{11} parameter (Fig. 4.7c). There was a much more gradual increase in the Ω_{11} value for the +45º or −45º cases as compared to the composite cases, with a smaller peak occurring at a greater macroscale stretch.

Microscale variation in the fiber stretch distributions for the composite cases was also evident (Fig. 4.8). The mean and standard deviation of the fiber stretch varied between the homogeneous +45º and the merged cases at equivalent grip displacements (5.1 and 7.2 mm chosen for comparison). At equivalent grip forces (40 mN), however, the peak fiber stretch and median values within the distributions were nearly equivalent as compared to distinct differences at equivalent grip displacements. For both cases, the spread in microscopic fiber stretch increased at larger macroscopic stretches.

4.4 Discussion

Microstructural differences in networks affected the macroscale failure of our simulated collagen networks in several key ways. In terms of fiber alignment, our notched dogbones populated with microscale networks aligned parallel to the direction of extension failed at smaller macroscopic strains but generated larger peak forces prior to failure as compared to the isotropic case (Fig. 4.2). In terms of merging and layering networks, dogbones populated with homogenously aligned rotated networks at +45º or −45º failed at larger strains and smaller peak forces as compared to alternating alignment layers or networks with merged alignments (Fig. 4.6). Alternating layers or using merged networks to incorporate heterogeneity in alignment appeared to generate similar macroscale (local and grip-to-grip deformation) and microscale outcomes (fiber stretch and fiber orientations) (Figs. 4.6 and 4.7). Using homogeneous +45º or −45º aligned rotated networks lead to failure propagation appeared to follow the direction of off-axis alignment as macroscale and microscale stretch and failure appeared to follow the microscale fiber alignment of the dogbone (Fig. 4.6).

Much of the variation in macroscale failure outcomes from differences in microscale fiber alignment and network type appeared to arise from differences in the microscale stretch, reorientation, and rearrangement of fibers (Figs. 4.3, 4.7, 4.8). Initial alignment and rotation of networks determined the ability of fibers to reorient and realign in response to macroscopic deformations. Fibers in networks initially aligned parallel to the axis of extension had limited opportunity to rotate and realign, leading to macroscopic

failure at smaller strains compared to the isotropic case. However, since such fibers were already aligned in the direction of the loading, there was a rapid recruitment (and subsequent loss) of fibers that contributed to larger macroscopic grip forces along the axis of extension prior to macroscopic failure as compared to the isotropic case (Fig. 4.3). The converse held true for networks with fibers aligned perpendicular to the axis of loading (Fig. 4.5). When fibers were aligned largely perpendicular to extension, macroscale failure occurred at greater strains but at diminished grip forces. Heterogeneity in alignment (layered or merged in RVE networks) changed the stiffness, peak force at failure, and strain at peak force (Fig. 4.4). Differences in microscale fiber reorientation between these two cases were also apparent (Figs. 4.6−4.8).

Our work on modeling variation in macroscopic failure from microstructural differences in a simulated collagen material has direct relevance and potential applications in understanding failure at various length scales in native and engineered tissues. In native and engineered surrogates (Nerurkar et al., 2009) for annulus fibrosus, the crisscrossing of alternating layers of differing collagen fiber alignment appear fundamental to the mechanics of the tissue. In particular, Nerurkar et al. have developed a model system for exploring the mechanical role of alternating layers of fibers of varying alignment in engineered cell-seeded annulus fibrosus surrogates and have observed significant mechanical effects from crisscrossing layers of differing fiber alignment (Nerurkar et al., 2007). The effects of crisscrossing alignment layers was also apparent in our model and could be further explored by directly examining microscale (fiber alignment, fiber

stretch, fiber orientation) and macroscale (grip force, local stress, local deformation) simulated outcomes that may help to understand the complex multiscale mechanics of heterogeneous and anisotropic tissues. In addition, the role of connections between aligned layers must be explored further. The model can potentially be applied to help understand the role of microstructural differences in the mechanical failure of other soft tissues where spatial homogeneity or heterogeneity in fiber alignment plays a significant mechanical role, such as the supraspinatus tendon (Lake et al., 2009).

While differences in collagen fiber alignment play a role in prescribing macroscale failure outcomes, the model must be expanded to consider the role of fiber-to-fiber connectivity, intrafibrillar matrix, and multiple protein networks in order to model the failure of fiber reinforced native and engineered soft tissues. Our group has previously explored the role of matrix in the prefailure behavior of collagen tissue analogs (Lake et al., 2012a), and similar approaches can be used to include matrix into our current failure model. Significant work experimentally characterizing or modeling the mechanics of multiple protein fiber systems such as those incorporating collagen with fibrin or collagen with elastin has been done by several groups (Cummings et al., 2004; Lai et al., 2012b), and can be incorporated into our current model by modifying the constitutive equation for fibers, modifying the failure mechanisms based on fiber type, and potentially include a fiber interaction component. This initial study was limited to uniaxial extension, and multiaxial extension would be another important test in understanding the failure mechanics of tissue analogs subjected to physiologically relevant loading and in

understanding the multiscale mechanics of the system over a broader range of deformations and with new sample geometries.

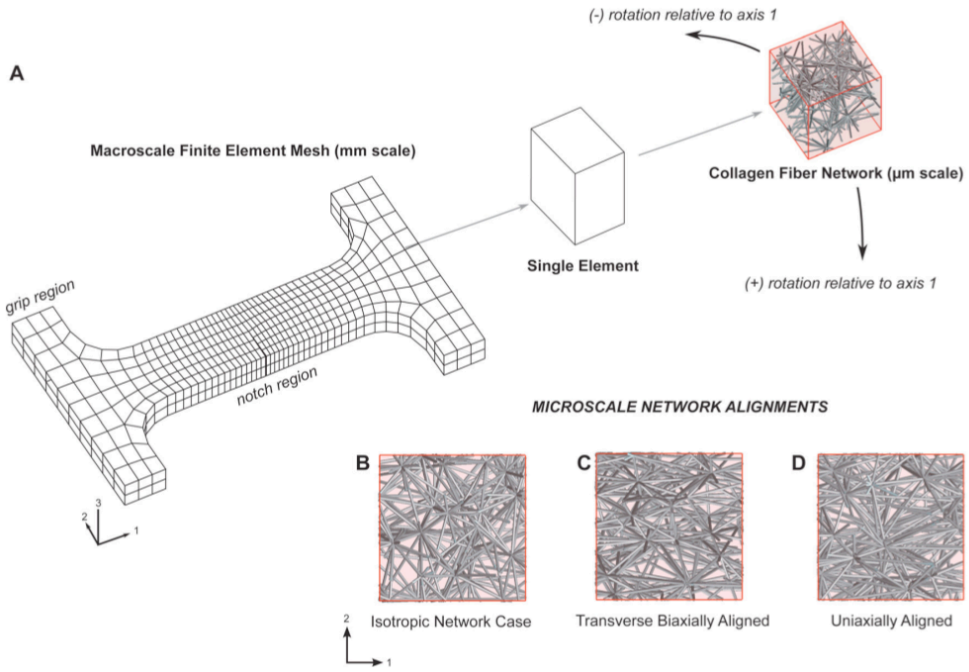

Fig. 4.1: (A) Multiscale damage model consisted of a millimeter-scale finite element continuum (in a notched dogbone geometry) with representative volume elements of micrometer-scale collagen fiber networks of varying alignment at each Gauss point. Fibers were allowed to fail when stretched beyond a critical value. The model contained 624 finite elements, with 8 Gauss points per element, and with over 500 fibers in each network. The dogbone was fixed at one grip and extended under displacement control from the opposite grip along axis 1 to a final stretch ratio of 1.5. Microscale network fiber alignments were characterized using the orientation tensor, Ω, and were subsequently rotated relative to the axis of extension. (B) Isotropic networks had initial orientation tensor values $\Omega_{11}=\Omega_{22}=\Omega_{33}=0.33$. (C) Transverse biaxially aligned networks had orientation values $\Omega_{11}=0.43$, $\Omega_{22}=0.13$, and $\Omega_{33}=0.43$. (D) Uniaxially aligned networks had orientation values $\Omega_{11}=0.53$, $\Omega_{22}=0.23$, and $\Omega_{33}=0.23$.

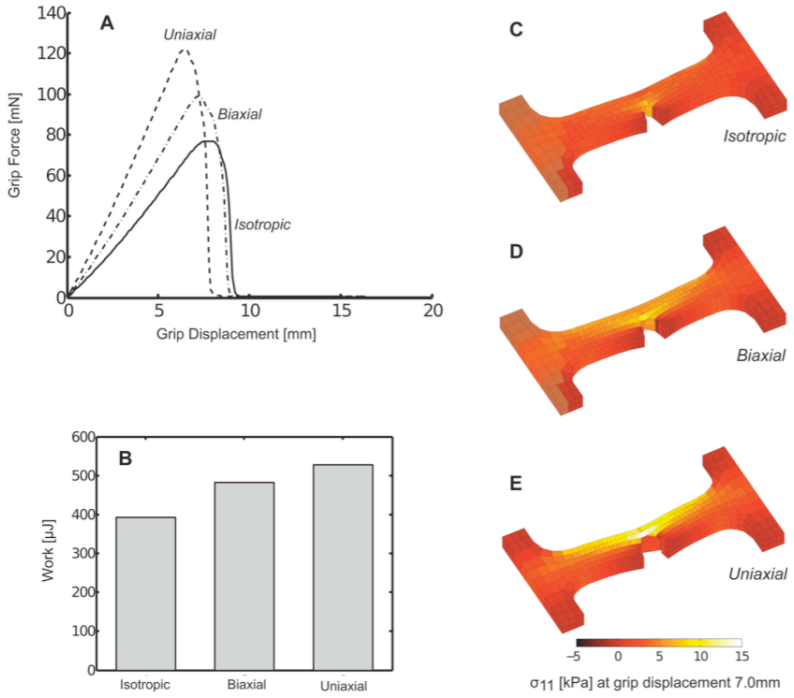

Fig. 4.2: (A) Macroscopic grip force varied based on model microscale fiber alignments as dogbone samples were uniaxially stretched to failure. (B) The corresponding mechanical work for these deformations also varied by alignment case. (C–E) At the same grip displacement of 7.0 mm, differences in the stress and deformation for each case were apparent.

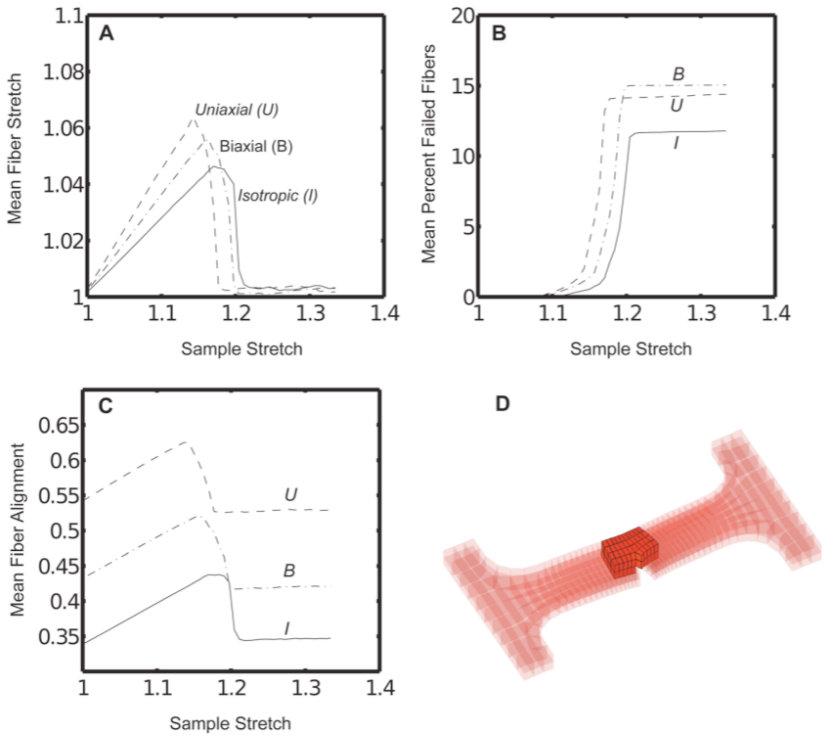

Fig. 4.3: (A) The mean fiber stretch, (B) the mean percentage of failed fibers, and (C) the mean fiber orientation parameter Ω_{11} varied over the macroscale sample stretch for each fiber alignment case. (D) Fibers were analyzed from a region of notch-adjacent elements. The same region was used to generate plots in Figs. 4.7 and 4.8.

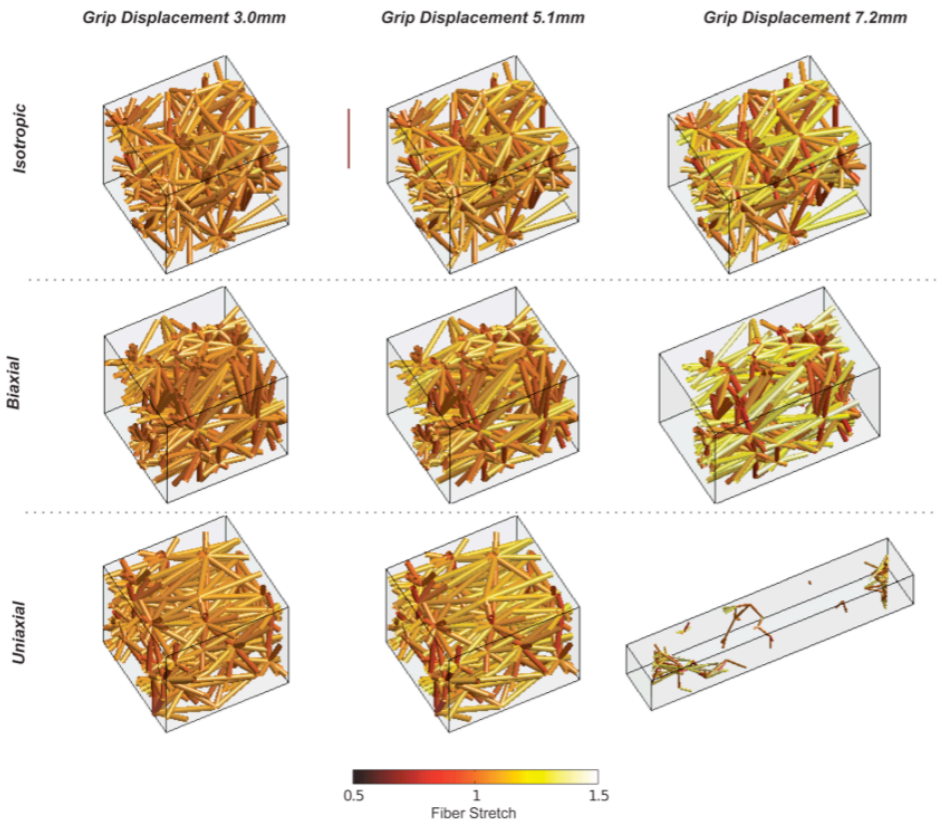

Fig. 4.4: A single microscale network in the model experienced distinct fiber stretches and failure at varying grip displacements for each alignment case. The network was selected from a notch-adjacent element.

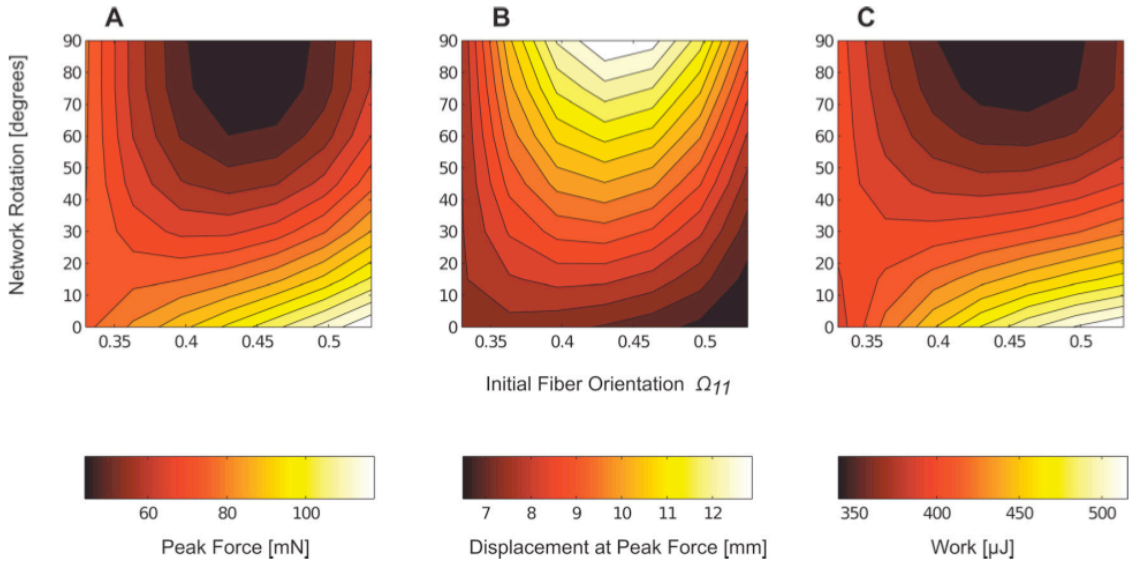

Fig. 4.5: Contour plots of the macroscale (A) peak grip force, (B) displacement at peak grip force, and (C) work were interpolated as functions of the initial network fiber orientation parameter Ω_{11} and the network rotation. The largest forces occurred when fibers were aligned parallel to extension, and the largest pre-failure strains when fibers were aligned perpendicular to extension.

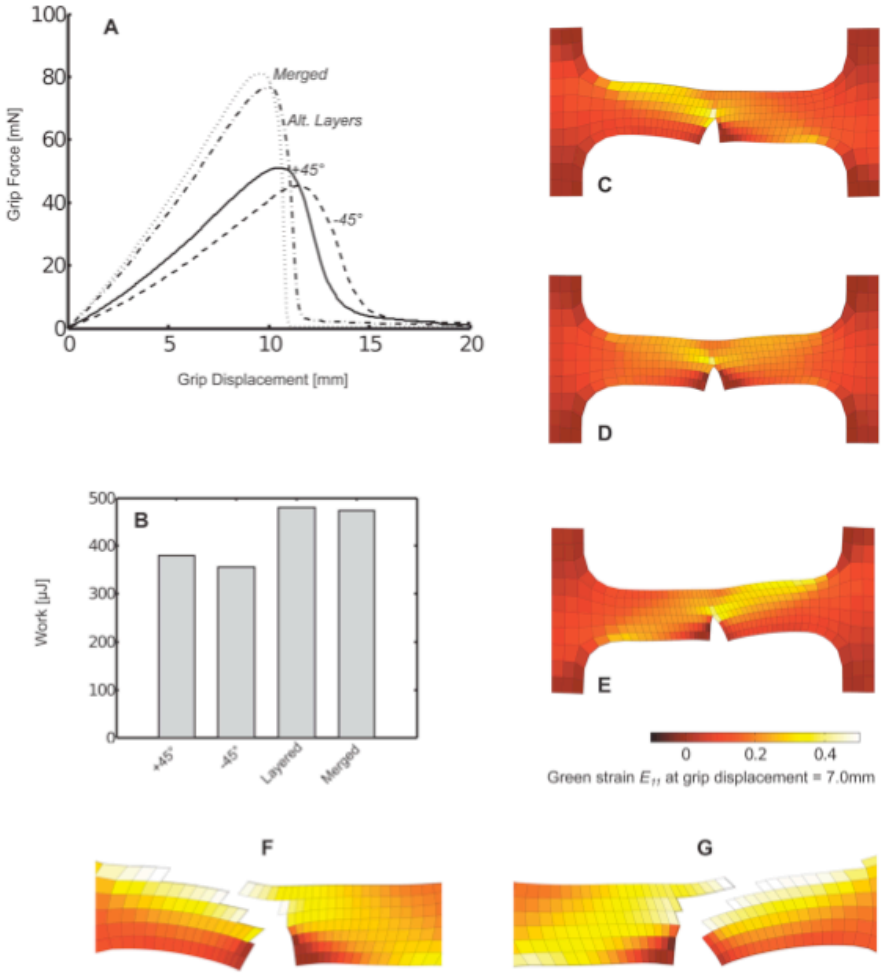

Fig. 4.6: (A) Macroscopic grip force varied based on differing microscale composite or uniform fiber alignments as dogbone samples were uniaxially stretched to failure. (B) The corresponding mechanical work for these deformations also varied based on the composite or uniform fiber alignment type. (C–E) At the same grip displacement of 7.0mm, differences in the macroscopic Green strain were apparent between the (C) all +45º rotated aligned networks, (D) layered +45º/−45º networks, and (E) all −45º networks cases. To illustrate the propagation of failure along the direction of fiber alignment for the (F) all +45º and (G) all −45º cases, elements with the greatest fiber losses (approximately the top 10%) were removed from plots of notch strains at a grip displacement of 10.8 mm.

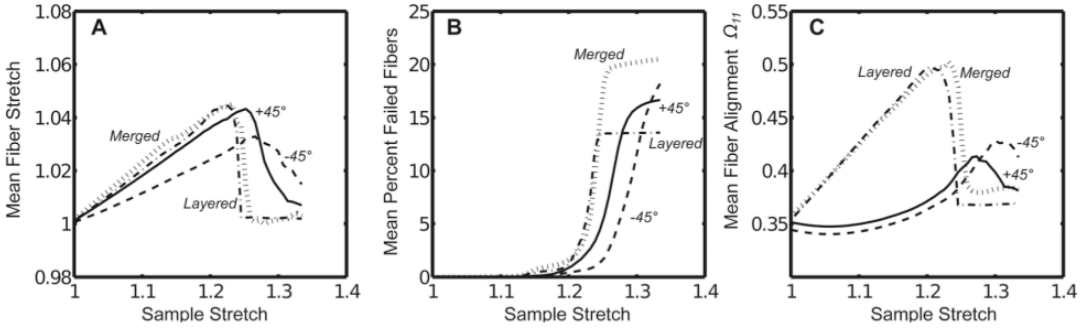

Fig. 4.7: (A) The mean fiber stretch, (B) the mean percentage of failed fibers, and (C) the mean fiber orientation parameter Ω_{11} varied over the macroscale sample stretch for each composite or uniform fiber alignment case. Fibers were analyzed from the notch-adjacent elements depicted in Fig. 4.3.

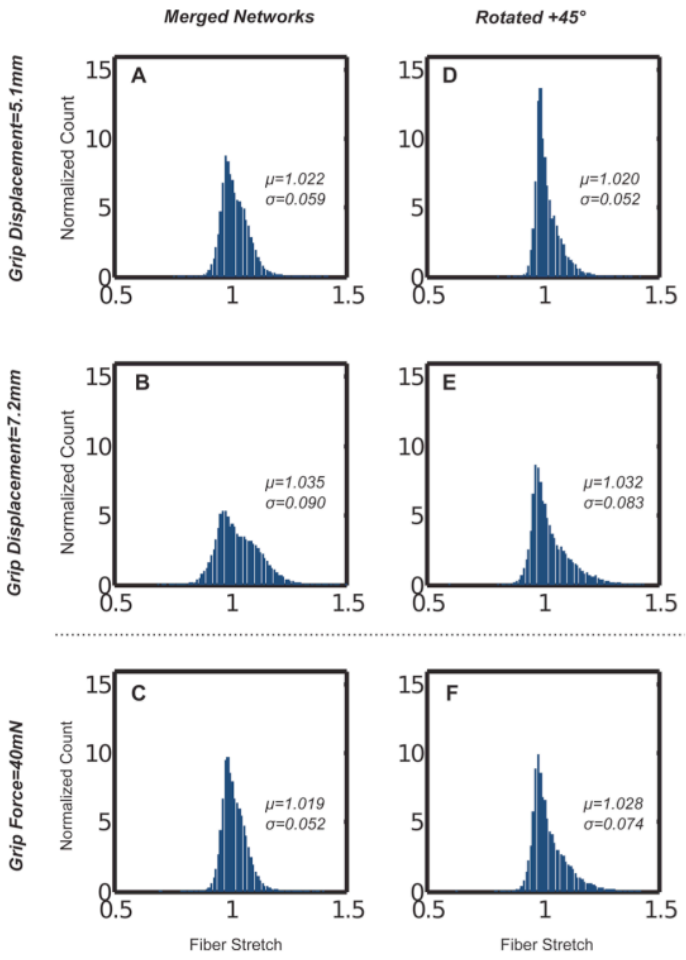

Fig. 4.8: Fiber stretch distributions varied for the (A–C) merged and (D–F) rotated aligned network cases at equivalent grip displacements but were similar at equal grip forces. Fibers were analyzed from the notch-adjacent elements depicted in Fig. 4.3.

5. Mechanics of a Fiber Network within a Non-Fibrillar Matrix: Model and Comparison with Collagen-Agarose Co-Gels

The content of this chapter was published as a research article in the *Annals of Biomedical Engineering* by Lake, Hadi, Lai, and Barocas (Lake et al., 2012a).

5.1 Introduction

In order to understand fully the functional mechanics of soft tissues, it is necessary to characterize the mechanical properties of each tissue constituent and elucidate how they interact and function together. While the mechanical role of collagen (the primary structural component of connective tissues) is often evaluated, less is known about the role of non-fibrillar matrix (NFM, e.g., proteoglycans, glycosaminoglycans, cells, etc.), which varies compositionally across tissue types. Our recent work (Lake et al., 2011a; Lake et al., 2011b) evaluated collagen-agarose tissue analogs (with agarose as a representative NFM) in uniaxial tension and indentation to characterize the contribution of the NFM under different loading scenarios. In these studies, agarose was selected to represent non-fibrillar matrix because of several advantageous characteristics, namely its biocompatibility, uncharged nature, and ability to intersperse between fibers of a collagen gel without disrupting the collagen network (Ulrich et al., 2010). Results demonstrated that the NFM contributes significantly to the elastic and viscoelastic mechanical response and structural reorganization of soft tissues in a concentration-dependent manner, even in tensile testing in which collagen is normally assumed to be the predominant contributor.

While these studies have provided useful information, the mechanism by which NFM interacts with the collagen network on the microscale to alter the macroscale composite tissue properties remains unknown. Thus, the objective for the current work was to use a two-component microstructural model of the collagen-agarose system under quasi-static loading to elucidate the interaction between the collagen and the agarose during uniaxial extension of the co-gel.

Various approaches have been used to incorporate structural information into mechanical models of soft tissues. Three broad categories of model can be identified: isolated fiber (Ault et al., 1992; Cortes et al., 2012; Driessen et al., 2005; Guerin and Elliott, 2007; Holzapfel et al., 2000; Horowitz et al., 1988a; Horowitz et al, 1988b; Kiviranta et al., 2006; Lanir, 1979; Martufi and Gasser, 2011; Nagel and Kelly, 2010; O'Connell et al., 2009; Quapp et al., 1988; Raghupathy et al., 2009; Wagner et al., 2004; Wagner et al., 2011), regular-fiber-cell (Arruda et al., 1993; Bischoff et al., 2002; Kabla et al., 2007; Kuhl et al., 2005; Purohit et al., 2011; Sander et al., 2006; Susilo et al., 2010), and large-network (Kang et al., 2011; Nachtrab et al., 2011; Ritter et al., 2009; Sander et al., 2009c; Stein et al., 2010; Storm et al., 2005; Stylianopoulos and Barocas, 2007a). Isolated-fiber models, often expressed in terms of a continuum strain-energy function, are characterized by each fiber in the tissue behaving independently of the others and moving affinely with the macroscopic deformation. Regular-fiber-cell models involve a small unit cell (4-20 fibers) that is assumed to repeat within the tissue. These models capture some of the complex mechanical behavior of a tissue but can still be converted to a closed-form

stress-strain (or strain energy) expression. Fibers within regular-fiber-cell models may be able to move non-affinely, but the cells themselves deform with the macroscopic boundary. Finally, large-network models involve a network of hundreds to thousands of fibers, often arranged randomly, that interact fully with each other. In this case, the network must be large enough that different networks with the same overall structural properties (alignment, crosslink density, etc.) produce the same stress-strain results even if the detailed structures are quite different. Highly non-affine kinematics exhibited by interacting fibers are consistent with reports that collagen fiber kinematics in native tissues do not follow the affine assumption (Billiar and Sacks, 1997; Gilbert et al., 2006; Guerin and Elliott, 2006; Hepworth et al., 2001; Lake et al., 2012b).

Each of these three modeling approaches exhibit specific advantages, and models constructed at each domain size (isolated fiber, regular-fiber-cell, large-network) have provided insight into the mechanical behavior of a variety of materials, including native soft tissues (Ault et al., 1992; Cortes et al., 2011; Driessen et al., 2003; Driessen et al., 2005; Driessen et al., 2008; Driessen et al., 2004; Horowitz et al., 1988a; Horowizt et al., 1988c; Julkenen et al., 2009; Kiviranta et al., 2006; Maceri et al., 2010; Martufi and Gasser, 2011; Nagel and Kelly, 2010; Stylianopoulos and Barocas, 2007a), biological tissue analogs (Driessen et al, 2007; Nachtrab et al., 2011; Nagel and Kelly, 2011; Purohit et al., 2011; Ritter et al., 2009; Stein et al., 2010; Storm et al., 2005; Susilo et al., 2010), and biomimetic synthetic materials (Amoroso et al., 2011; Kabla and Mahadevan, 2007). In addition to representing the collagen component, several previous models have

also considered the contribution of the NFM. Within models based on non-interacting fibers, NFM has been represented, often via a neo-Hookean or Mooney-Rivlin formulation, as a summed contribution to the collagen stress (Cortes and Elliott, 2012; Driessen et al., 2005; Guerrin and Elliott, 2007; Holzapfel et al., 2000; Martufi and Gasser, 2011; Nagel and Kelly, 2010; O'Connell et al., 2009; Quapp et al., 1998, Tang et al., 2009; Wagner and Lotz, 2004). Since each fiber in these models functions independently (of other fibers and the NFM) at the local level, interactions between tissue constituents cannot be evaluated. To capture such interactions, some models have included an additional term to incorporate the stress contribution due to interactions between the collagen network and NFM (Guerin and Elliott, 2007; O'Connell et al. 2009; Peng et al., 2006; Wagner and Lotz, 2004). When the fiber architecture is precise and well known, the form of the interaction contribution can be suggested by the structure of the tissue (as in (Guerin and Elliott, 2007) amongst others). Unfortunately, for an unstructured fiber network the appropriate definition for the interaction term is unknown. For regular-fiber-cell models, the general tendency is to evaluate the collagen network alone, but a few studies have incorporated a “bulk” term to describe the contribution from non-collagenous material (Bischoff et al., 2002; Kuhl et al., 2005). To date, however, these models have focused on the fiber component and have not been used to specifically evaluate the role of NFM or how it interacts with fibrillar material to alter the composite tissue response. Similarly, large-network models have not generally included a representation of NFM. One exception is a previous study performed by our group (Stylianopoulos and Barocas, 2007a), in which a neo-Hookean NFM term was

incorporated in parallel with collagen networks in a multiscale model to simulate the mechanical behavior of decellularized arteries. The current study employs a modified version of our previous approach, but constructed more closely with experimental data and with a more specific focus on microstructural properties and relationships. Therefore, the purpose of this study was to apply a large-network-based modeling approach to experimental co-gel data to evaluate the role of non-fibrillar matrix and the nature of microstructural collagen-matrix interactions in soft connective tissues.

5.2 Methods

5.2.1 Material of Interest

A microscale model was developed for collagen-agarose co-gels, of which experimental data was presented previously (Lake et al., 2011a). Although the fabrication and testing of the gels are described elsewhere, a brief description is provided here as part of the development of the model. Collagen-agarose co-gels composed of 1.0 mg/mL collagen and 0% (NoAg), 0.125% (LoAg) or 0.25% (HiAg) w/v agarose were cast in dog-bone shaped Teflon molds (Fig. 5.1a) and allowed to gel. Agarose, which constituted the NFM of this tissue analog system, formed an interspersed, web-like matrix within the collagen network (Ulrich et al., 2010; Lake et al., 2011a). Co-gels were subjected to a four-step incremental stress-relaxation tensile test, wherein the load, tissue strain, and cross-sectional area were recorded throughout testing, and quantitative polarized light imaging (QPLI) was used to quantify collagen fiber alignment and kinematics. The present study

focused on the equilibrium (relaxed) data from the final step of these tests, corresponding to ~10% tensile strain.

5.2.2 Model Formulation

While several different types of computational networks have been used to represent collagen (e.g., random growth (Sander et al., 2009b; Stylianopoulos and Barocas, 2007a), confocal microscopy reconstruction (Stein et al., 2010), scanning electron microscopy (D'Amore et al., 2010) reconstruction), Voronoi networks were used in this study. Such networks were recently shown to provide a close approximation to collagen gel behavior (Nachtrab et al., 2011), and the sparse arrangement and low nodal degree of Voronoi networks allowed for generation of networks that exhibited very large Poisson's ratio values (~3) similar to those measured experimentally for our collagen-agarose co-gels (Lake et al., 2011a). Previous studies using other network types (Sander et al., 2006; Stylianopoulos and Barocas, 2007a; Susilo et al., 2010) have been unable to achieve Poisson's ratio values as large as those measured experimentally for tissue analogs, which are likely caused by significant network reorientation, compaction and densification of the network, and exudation of interstitial fluid. In the present study, networks were created by randomly placing seed points within a representative volume element (RVE), generating a 3D Voronoi tessellation about these points, and placing nodes at the intersections of Voronoi edges (Fig. 5.1b). Networks were created in Matlab (Natick, MA) using the VORONOIN function, an implementation of the widely-used Qhull code. In order to ensure that results were not dependent on a specific placement of

seed points, five different networks were created and evaluated in this study (i.e., n=5 for each simulation group) with ~700 fibers per network. Using an assumed fiber diameter of 70 nm, collagen density of 1.34 g/mL, and the experimental collagen concentration (1 mg/mL), the average edge length in undeformed RVEs was computed (Stylianopoulos and Barocas, 2007a) to be ~20 μm; consequently, average RVE volume was ~8,000 μm^3. Generated Voronoi networks were isotropic, so a pre-stretch was applied along the x-axis, and the RVEs were clipped to the original size, such that initial network alignment approximated the anisotropic alignment of co-gels measured via QPLI. The number of seed points (and hence, number of fibers) was adjusted until the Poisson's ratio of stretched RVEs equaled values for NoAg gels. Nodes at fiber intersection points were modeled as freely rotating pin joints, and fibers were modeled as one-dimensional nonlinear springs, with the force on each fiber defined as (Billiar and Sacks, 2000; Gasser et al, 2006; Holzapfel et al., 2000; Sander et al., 2009b; Stylianopoulos and Barocas, 2007a):

$$F = \frac{E_f A}{B}(e^{B\varepsilon} - 1) \qquad (1)$$

where E_f is the elastic modulus of the fibers at infinitesimal strain, A is the fiber cross-sectional area, B is a nonlinearity constant, and ε is the fiber Green strain given by $\varepsilon = 0.5(\lambda_f^2 - 1)$. Parameter values for the fiber constitutive equation were used as previously (Sander et al., 2009b) (fiber radius=35 nm; B=3.8), where the fiber modulus value E_f was set at 6.5 MPa in order to produce total stress values (calculated as defined below)

approximately equal to experimentally-measured values for the NoAg group. With the fiber forces thus defined, the volume-averaged Cauchy stresses from the collagen network at each RVE surface were computed by (Chandran and Barocas, 2007; Stylianopoulos and Barocas, 2007b):

$$\sigma_{ij}^{col} = \frac{1}{V} \sum_{bnd\ nodes} x_i F_j \tag{2}$$

with V as the RVE volume and x_i corresponding to the position of each fiber (with force F_j) on a given RVE boundary.

As done in our previous study (Stylianopoulos and Barocas, 2007a), the non-fibrillar matrix (NFM) was represented using a compressible neo-Hookean solid formulation. Assuming no shear, Cauchy stress due to the NFM was defined as (Holzapfel, 2000):

$$\sigma^{nfm} = G\left(\frac{\lambda^2}{J} - J^{-2\beta-1}\right) \tag{3}$$

where G is the NFM shear modulus, λ is the RVE stretch, J is the Jacobian, $\beta = \nu_m/(1-2\nu_m)$, and ν_m is the Poisson's ratio of the matrix. Since the model represents the mechanical response at equilibrium (after relaxation and drainage of any pressurized interstitial water), ν_m was taken to be 0.1 (Nagel and Kelly, 2010). Values for G were specified by extrapolating experimental data for the shear modulus of pure agarose gels (Benkherourou et al., 1999) to concentration values used in our study such that $G = 0$,

110 and 720 Pa for NoAg, LoAg, and HiAg, respectively. In this way, the only difference between models representing the three experimental groups was in the specific value used for shear modulus. All other variables (e.g., organization of the Voronoi collagen network, parameter values for the fibers) were consistent across the three different co-gel models. The total stresses in the composite model were calculated by summing the contributions from the collagen network and the NFM (Fig. 5.1c) in a parallel manner:

$$\sigma^{tot} = < \sigma^{col} > + \sigma^{nfm} \quad (4)$$

5.2.3 Model Solution

A 10% strain was applied to each RVE in the 1-direction (λ_1=1.1), while the 2- and 3-directions had stress-free surfaces (Fig. 5.2). After the step displacement, the position of the internal nodes and the position of the unloaded boundaries (2- and 3-faces) were solved for using Newton's method to ensure force balance at each internal node and minimal normal stresses on the free surfaces (i.e., σ_{22} and σ_{33}; Fig. 5.2). For all three groups (NoAg, LoAg, HiAg), simulations were evaluated for each of the five networks. For each run of the microscale model, the total normal stress in the loaded direction (σ_{11}) and the Poisson's ratio of the composite RVE were computed and compared to experimental co-gel data. In addition, the stresses due to each component ($<\sigma_{11}^{col}>$, σ_{11}^{nfm}) and the amount of stretch on each fiber (λ_f) were evaluated along with 3D maps

showing network orientation and fiber stretch. All model simulations were performed in Matlab, with a run time of a few minutes.

A second set of simulations was performed to explore the parameter space of the NFM neo-Hookean term. To characterize the parameter space, the shear modulus and Poisson's ratio were varied across a range of values (G = 1, 10, 110, 330, 720, 1310 Pa; v = 0, 0.05, 0.1, 0.15, 0.2, 0.25, 0.3, 0.35, 0.4, 0.45, 0.49), and RVEs were evaluated for each combination of parameter values.

5.2.4 Statistical Analysis

A one-way ANOVA was utilized to compare mean fiber stretches across groups and post-hoc *t*-tests were used to identify statistically significant specific comparisons. Bonferroni corrections were applied when making multiple comparisons.

5.3 Results

The model-predicted values of Poisson's ratio and total stress (in the 1-direction) compared well with experimental values (Fig. 5.3a and Fig. 5.3b, respectively). Data trends showed qualitative agreement, indicating that the microscale model made good, if not exact, predictions of the experimental data. An examination of the relative proportion of the total stress contributed by each component (Fig. 5.3c) yielded a very small NFM contribution in the LoAg samples (average = 3.8% of total stress), and a larger NFM contribution for the HiAg samples (average = 18.6% of total stress).

Representative network maps at 10% strain showed that fiber orientation and fiber stretch varied significantly across different groups (Fig. 5.4). In these plots, gray fibers are unstretched relative to the undeformed case ($\lambda_f = 1$), red fibers are in tension ($\lambda_f > 1$), and blue fibers are in compression ($\lambda_f < 1$). As the amount of NFM increased (from NoAg to LoAg to HiAg), the number of blue and gray fibers decreased and the intensity of red fibers increased, demonstrating an overall increase in fiber stretch due to the NFM. Fiber stretch was also evaluated quantitatively by comparing frequency distributions (Fig. 5.5a) and mean fiber stretch values (Fig. 5.5b), where significant differences were observed between the groups ($p<0.001$). Another observation from the network maps was the difference in volume change due to the presence/quantity of NFM; NoAg RVEs compacted significantly in the lateral directions, while the HiAg RVEs strongly resisted volume change (Fig. 5.4). Importantly, the NFM's resistance to volume change (also demonstrated by decreasing Poisson's ratio) likely resulted in the increased fiber stretches by not allowing the fibers to reorient in the direction of loading and compact the lateral boundaries.

Parameter space plots (Fig. 5.6 and 5.7) demonstrate how output values changed as a function of the two parameters in the neo-Hookean NFM term (Poisson's ratio v_m and shear modulus G). Interestingly, at low G values and moderate v_m values, the NFM stress (σ^{nfm}) was negative (Fig. 5.6a), indicating a compressive stress contribution from the NFM. With this transition from compressive to tensile stress, the parameter space for

σ^{nfm} included a boundary along which the stress contribution from the NFM was zero (dashed line, Fig. 5.6a). The collagen network stress (σ^{col}) and the total stress (σ^{tot}) increased with increasing G (Fig. 5.6b and 5.6c, respectively). For all stress measures, increasing the value of ν_m had minimal impact at high G, but made a more significant impact at low values of G (Fig. 5.6, right column). In a similar manner, parameter maps for RVE Poisson's ratio and fiber stretch (Fig. 5.7a and 5.7b, respectively) demonstrated relatively consistent values when G>300 Pa, but much greater variation in values at low G. As Poisson's ratio of the NFM (ν_m) increased, the composite Poisson's ratio decreased and λ_f increased. Furthermore, there was an inverse relationship between RVE Poisson's ratio and mean fiber stretch (Fig. 5.7c).

5.4 Discussion

In this study, a network-based microscale model was developed and fit to experimental data from collagen-based tissue analogs. After adding (in parallel) a term to describe the mechanical contribution from the non-fibrillar matrix (NFM), the model was able to predict qualitatively the composition-dependent mechanical response of collagen-agarose co-gels in tension (Fig. 5.3a and 5.3b). The microscale model utilized here allowed for the characterization of how the collagen fiber network (represented via Voronoi networks) was reoriented and stretched differentially as a function of increasing NFM.

Our experimental studies of collagen-agarose co-gels (Lake et al., 2011a; Lake et al., 2011b) suggested that agarose served a volume-preserving role in co-gel deformation.

Similarly, the neo-Hookean term representing the NFM contribution in our microscale model increased resistance to volume change. Specifically, lateral compaction in the 2- and 3-directions that occurred during a stretch in the 1-direction decreased as a function of NFM concentration, as measured by average Poisson's ratios from model simulations (Fig. 5.3a) and by comparing deformed dimensions of representative network maps (Fig. 5.4). As lateral compaction decreased, the reorientation of the fibers towards the direction of loading was limited, leading to increased stretching of the fibers (Fig. 5.4 and 5.5). In fact, further simulations yielded data that showed a distinct correlation between Poisson's ratio of the RVE and mean fiber stretch (Fig. 5.7c). Parameter space plots show how these measures changed as parameter values for the NFM term (shear modulus G and NFM Poisson's ratio ν_m) were varied across a full range of values (Fig. 5.7a and 5.7b). At high G (~400 Pa and above), RVE Poisson's ratio and fiber stretch remained relatively consistent, even when ν_m was varied significantly; however, at low G these values were highly dependent on changes in G and ν_m.

The stress contribution due to the NFM was computed as predicted for the three sample groups: while trivially zero for the NoAg samples, the NFM stress was very small for the LoAg samples and moderate for the HiAg samples (Fig. 5.3c). Further exploration of the neo-Hookean NFM parameter space demonstrated a transition to negative (compressive) stress for the matrix at low shear modulus and moderate Poisson's ratio (Fig. 5.6a). Although a compressive state in the unloaded (2- and 3-) directions is intuitive (in opposition to the collapsing collagen network due to the Poisson effect), a compressive

NFM stress in the 1-direction is somewhat unexpected. Such a result indicates that, instead of providing a reaction-force-type response to the deformation (as the collagen network does), the NFM force acts in the direction of the grip and decreases the magnitude of the composite tensile stress. While this notion is initially counterintuitive, previous computational studies (Horowitz et al., 1988a; Horowitz et al., 1988b) have demonstrated a similar result for the hydrostatic pressure term in a fiber-based incompressible model, and our experimental co-gel data (Lake and Barocas, 2011a) suggested this possibility since peak stress values decreased with increasing amounts of NFM (i.e., agarose). In addition, our previous fiber-matrix multiscale model of artery mechanics (Stylianopoulos and Barocas, 2007a) predicted that the non-collagenous matrix would be in compression in order to prevent the collapse (i.e., lateral compaction) of the collagen network. Thus, a compressive NFM stress in the loading direction due to pressurization of the composite material is plausible at certain parameter values of the NFM component.

A possible mechanism for compression of the NFM, and for how the NFM transitions to a tensile stress at different parameter values, is represented using a simple schematic (Fig. 5.8). For simplicity, a 2D representation of the 3D physical system is used. When collagen-only (NoAg) samples are stretched (Fig. 5.8a), the collagen provides a reaction force (F_1^{col}) in resistance to the deformation in the 1-direction, while the stress-free 2-boundary exhibits no net force (i.e., $F_2^{col} = 0$). When added to the collagen network, NFM contributes to the composite mechanical response in two ways (Fig. 5.8b): through

a reaction force (F^{nfm}) that resists deformation and through an isotropic pressure (P^{nfm}) that resists volume change. The presence of P^{nfm} balances the transverse tension in the collagen network F_2^{col} to help maintain volume and satisfy the zero total stress condition on the 2-boundary. In samples with small shear modulus (G) and moderate to high Poisson's ratio (v_m) values (Fig. 5.8b), F_1^{nfm} is relatively small because of low G, so P^{nfm} dominates, resulting in a negative (i.e., compressive) total stress from the NFM (σ_1^{nfm}). On the other hand, at large G and/or small v_m (Fig. 5.8c), the high shear modulus increases the magnitude of F^{nfm} over that of the P^{nfm}, resulting in a positive (i.e., tensile) total σ_1^{nfm}.

Collagen-based tissue analogs and some collagenous native tissues (e.g., tendon and ligament) can exhibit very high Poisson's ratio in uniaxial tension experiments (Hewitt et al., 2001; Lake, 2009; Lake and Barocas, 2011a; Lynch et al., 2003). Poisson's values as high as 2-3 are due to a high degree of network reorientation towards the loading direction (Lake et al., 2011a; Lake et al., 2009), significant compaction and densification of the network due to fibers buckling under transverse strain (Kabla and Mahadevan, 2007), and significant exudation of interstitial fluid (Adeeb et al., 2004; Wellen et al., 2004). Although one recent study presented a micromechanical finite element model that was able to predict high Poisson's ratios using crimped fibers in a super-helical organization (Reese et al., 2010), previous regular-fiber-cell and large-network models have only been able to achieve maximum Poisson's ratio values of ~1 (Sander et al., 2006; Stylianopoulos and Barocas, 2007b; Susilo et al., 2010), thereby failing to replicate

the high values measured experimentally (Stein et al., 2010; Susilo et al., 2010). Voronoi networks, which were previously reported to show quantitative agreement to collagen networks (Nachtrab et al., 2011), contain fewer fiber-fiber crosslinks than other network types used in previous models, thereby allowing for greater fiber reorganization and subsequent network compaction under load. In the present study, Voronoi networks representing the collagen-only gels exhibited Poisson's ratios of ~3 in agreement with experimental data.

One difficultly in extending this modeling approach towards characterizing native tissues is identification of an appropriate mathematical formulation and corresponding material properties for the non-fibrillar matrix (NFM). As in several previous studies (Ulrich et al., 2010; Driessen et al., 2005; Holzapfel et al., 2000; Driessen et al., 2005; Holzapfel, 2000; Martufi and Gasser, 2011; Nagel and Kelly, 2010; Nagel and Kelly, 2011; Quapp et al., 1998; Stylianopoulos and Barocas, 2007a; Tang et al., 2009) the current work represented the NFM using a simple neo-Hookean solid with two input parameters: shear modulus and Poisson's ratio. The model was compared to experimental data at the equilibrium phase of a stress-relaxation test, so a low Poisson's value of 0.1 was used (Nagel and Kelly, 2010). In addition, since the model was constructed to represent collagen-agarose co-gels, values for the shear modulus were based on properties of agarose-only gels tested experimentally (Benkherourou et al., 1999), which are comparable to those used in other tissue modeling studies (Driessen et al., 2005; Holzapfel, 2000; Julkunen et al., 2009; Kiviranta et al., 2006). For native tissues, defining these parameters is more

difficult because the NFM term, as presently defined, lumps all non-collagenous material together (i.e., there is no single definition of NFM), making tissue-specific definition of these parameters challenging, and the experimental measurement of NFM properties very difficult. Certainly this topic merits further investigation.

This study is not without limitations. Due to the parallel construction of the microscale model, our approach did not allow for examination of fiber-matrix interactions internal to each RVE, which likely result in a heterogeneous strain and stress fields throughout the sample. Ongoing work by our group is developing a coupled fiber-matrix microscale model that will allow for characterization of these internal interactions. Another difficulty lies in appropriately matching the initial fiber orientation of the Voronoi networks to experimental data. We used a method described previously (Sander et al., 2009b) to match 3D network organization to the 2D experimental measures of sample alignment (using polarized light imaging), but the appropriate definition for the proportionality constant used in this analysis remains unclear. In spite of these concerns, the model developed and used in this study matched experimental observations well and demonstrated a mechanism by which pressurization of the NFM reduces lateral contraction of the collagen network and leads to a negative (compressive) stress in the NFM (σ_{11}^{nfm}) even though the composite tissue is in tension.

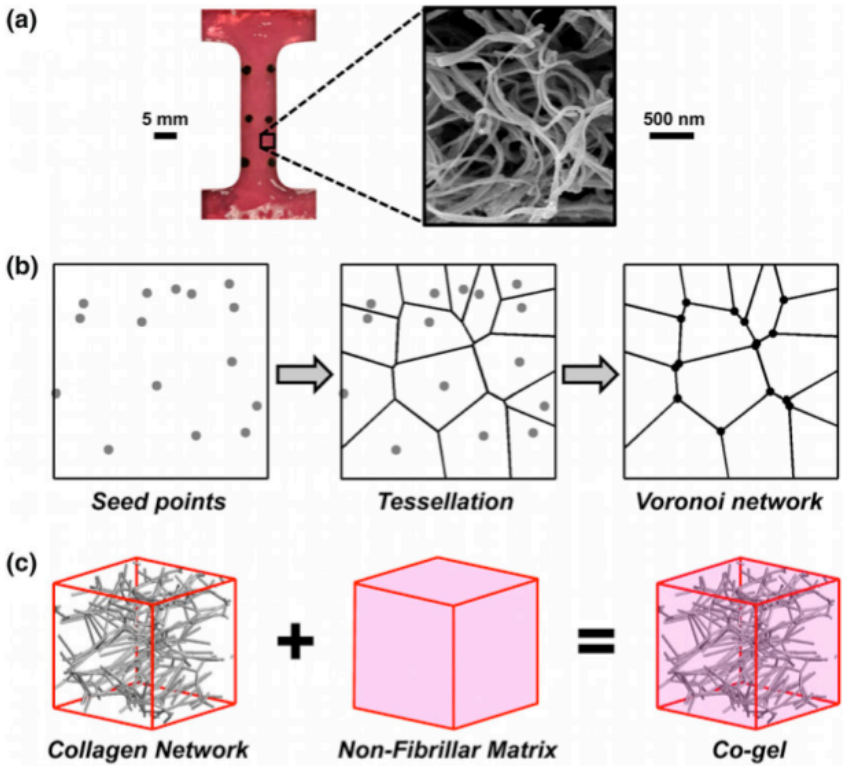

Fig. 5.1: A microscale network model was used to simulate the response of collagen-agarose soft tissue analogs. (A) Representative dog-bone shaped collagen gel tested experimentally[35] and scanning electron micrograph showing the reconstituted collagen network. (B) Computational networks were generated by randomly placing seed points within a representative volume element (RVE), generating a Voronoi tessellation about those seed points, and placing pin joint nodes at each fiber-fiber connection (schematic shows 2D network for clarity; actual Voronoi networks were 3D). (C) Collagen-agarose co-gels were modeled by adding the contributions from the collagen network and the non-fibrillar matrix in parallel.

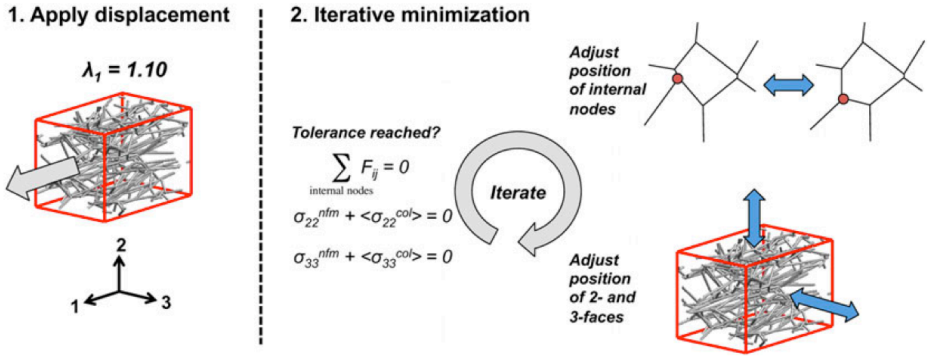

Fig. 5.2: After applying a stretch of 1.1 in the 1-direction, an iterative minimization scheme adjusted the position of the internal nodes and of the 2- and 3-direction surfaces until a tolerance was reached for the nodal force balance and stress-free boundaries.

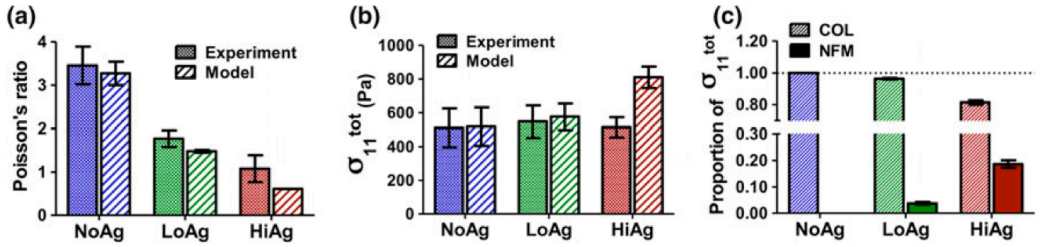

Fig. 5.3: Model-predicted values of (A) Poisson's ratio and (B) Cauchy stress in the 1-direction showed qualitative comparison with experimental values; (C) while stress in the NoAg samples was due (trivially) to collagen (COL) alone, the non-fibrillar matrix (NFM) contributed a small and moderate proportion of the total stress to the LoAg and HiAg groups, respectively (plots show mean ± 95%CI; n=5-7/group)

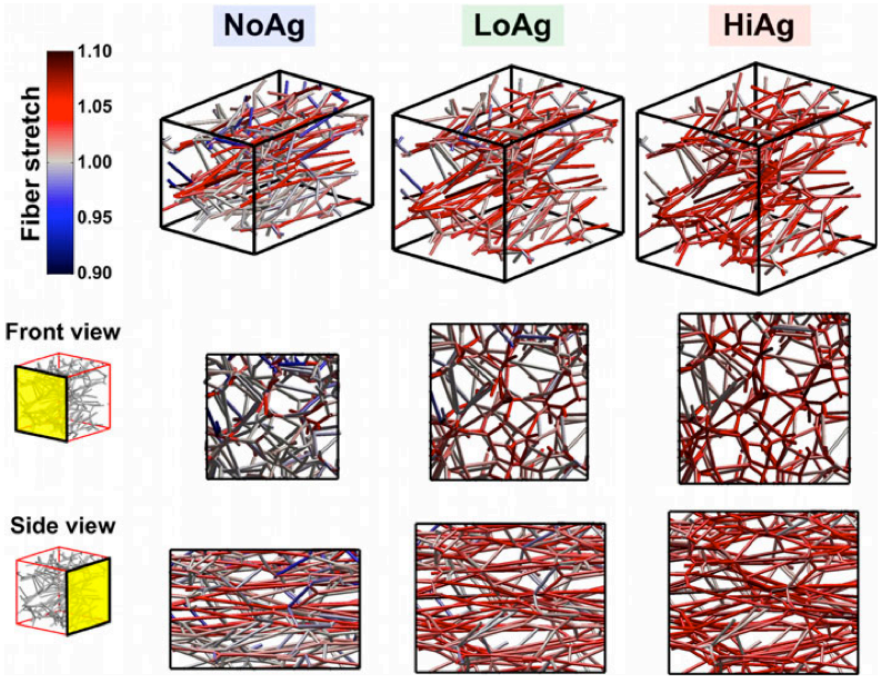

Fig. 5.4: 3D maps (and 2D projections) show how network organization and fiber stretch for a representative network changed as a function of NFM quantity: the amount of network compaction decreased and relative fiber stretch increased as NFM increased from NoAg to LoAg to HiAg (gray = unstretched relative to undeformed case, red = tensile stretch, blue = compressive stretch)

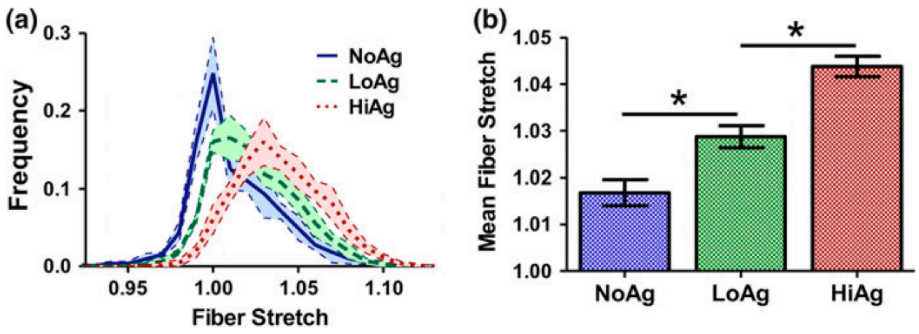

Fig. 5.5: Fiber stretch increased with increasing NFM composition, as demonstrated by (A) frequency distribution curves and (B) mean fiber stretch values (mean± 95%CI; n=5/group; * = significant differences)

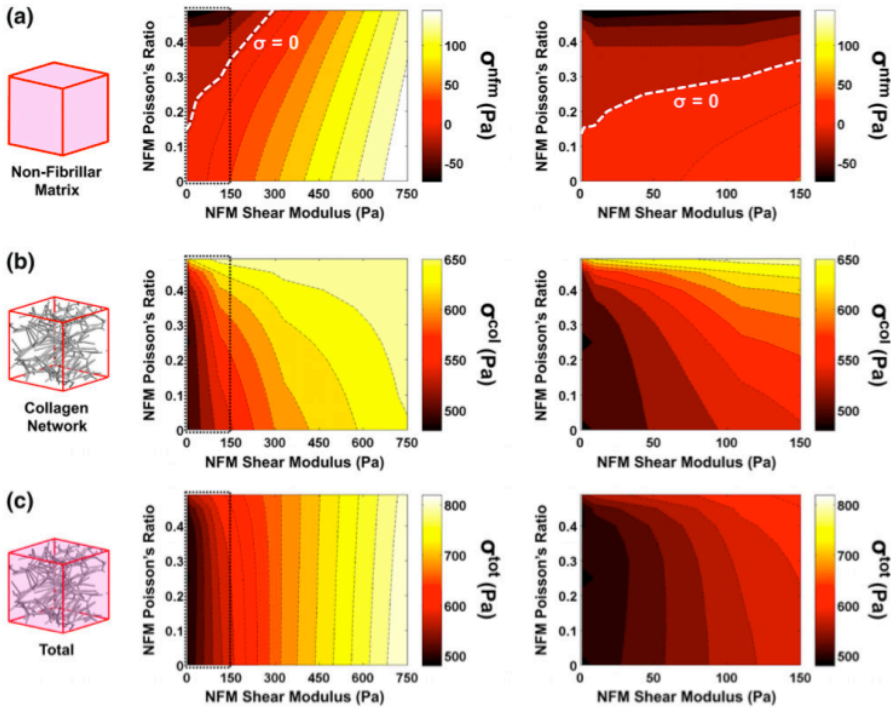

Fig. 5.6: Parameter space plots demonstrate how the (A) NFM stress, (B) collagen stress and (C) total stress changed as a function of varying the two NFM input parameters of shear modulus and Poisson's ratio (left = full parameter space; right = zoomed in low shear modulus region); of particular interest was the span of the NFM stress from negative to positive values, including the boundary (dashed line) where the contribution from the NFM was zero (mean values plotted; n=5/group)

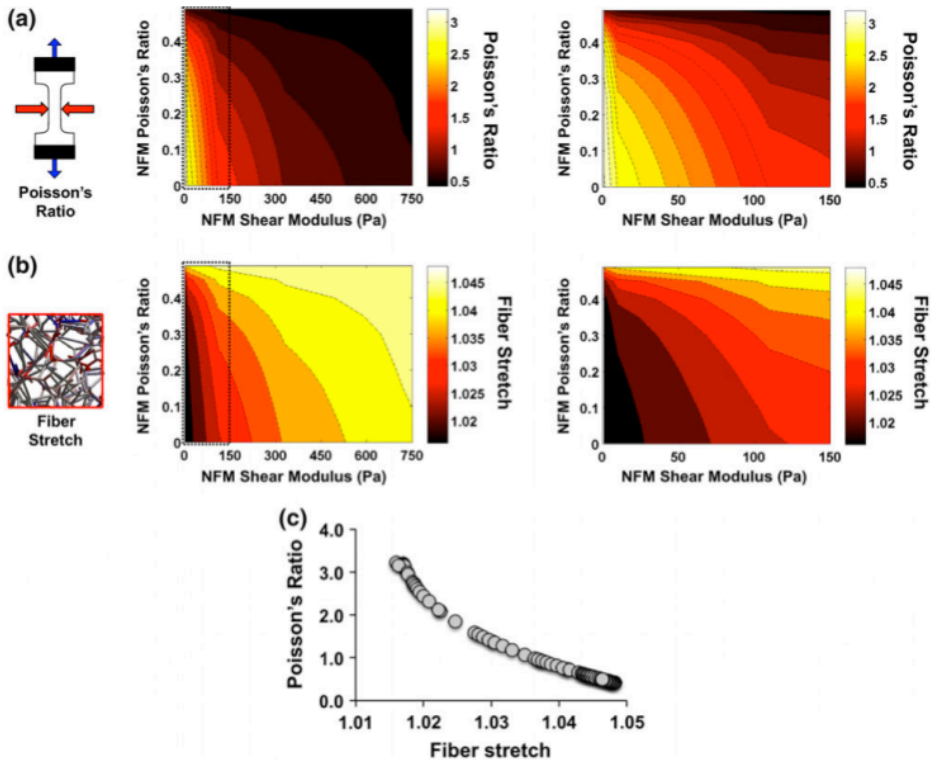

Fig. 5.7: Parameter space plots demonstrate how the (A) RVE Poisson's ratio and (B) fiber stretch changed as a function of varying the two NFM input parameters of shear modulus and Poisson's ratio (left = full parameter space; right = zoomed in low shear modulus region; mean values plotted; n=5/group); (C) there was a strong correlation between Poisson's ratio and fiber stretch values

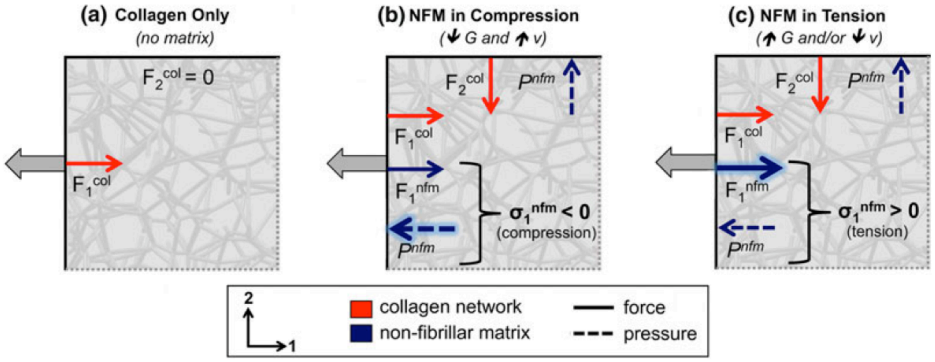

Fig. 5.8: 2D schematic demonstrating the proposed mechanism for the observed results. In the collagen-only (NoAg) case (left), collagen provided a reaction force (F_1^{col}) while the forces on the non-loaded boundary were zero. At low shear modulus and high Poisson's ratio (middle), the pressure due to the NFM resisting volume change (P^{nfm}) was greater than the NFM reaction force (F_1^{nfm}), resulting in a negative (compressive) stress from the NFM. At high shear modulus and/or low Poisson's ratio (right), the NFM reaction force (F_1^{nfm}) dominated over the pressure term (P^{nfm}), resulting in a positive (tensile) stress from the NFM.

6. Generating Random Fiber Network Topologies That Mimic Previously Characterized Networks

The content of this chapter is based on a previously submitted research abstract for the *ASME 2013 Summer Bioengineering Conference* (Hadi and Barocas, 2013b).

6.1 Introduction

Fibrous proteins, such as collagen and elastin, form the underlying structure of many soft tissues. These proteins form micrometer-scale networks of varying topology that play a role in governing the mechanics of tissues at larger length scales (Roeder et al., 2002). The relationship between a network's topology and its mechanics, however, are poorly understood. This disconnect presents an important challenge in constructing realistic multiscale models of tissues informed by collagen network micrographs and subsequently reconstructed networks (Stein et al., 2008). Accurate multiscale simulations may require thousands to millions of such unique networks. It is imperative that a method be developed to generate random networks that are functionally similar to ones derived experimentally.

In the current study, we present probabilistic methods (a Monte Carlo as well as a Metropolis generation scheme) for generating de novo networks that mimic the mechanical properties of previously characterized networks. We chose Delaunay and Voronoi networks as model targets because they have been used successfully to model

the mechanics of collagenous tissues (Lake et al., 2012a) and since their topologies are well characterized. Understanding the role of topology in network mechanics is fundamental to building improved models of the mechanics of fibrous soft tissues--models that can aid in the rational design of engineered tissues or that can help assess the mechanical impact of damage or disease on native tissues.

6.2 Methods

6.2.1 Network Generation

Monte Carlo Fiber Length Method Generation Scheme

We began by creating a set of Delaunay and Voronoi networks (n=20) that served as target networks to mimic via our network generation schemes. These target networks were generated from a random set of seed points in a 2-unit cube that were tessellated as Delaunay or Voronoi networks. Resulting networks consisted of nodes (network vertices) and fibers (network edges). The fiber length distributions from these target networks were used to generate fiber-length-specific probability distributions for each network type. Using a Monte Carlo scheme, we then generated Delaunay-like and Voronoi-like networks from the calculated fiber-length-specific probabilities. Briefly, each possible fiber from a random set of nodes in a 2-unit cube was iterated over, and a random value was drawn for each fiber and compared to its length-specific probability in order to accept or reject the fiber. The total set of possible fibers was traversed until a critical number matching the mean number of target fibers was exceeded. All networks were

characterized in terms of their fiber length distributions and nodal degree (number of fibers intersecting at each node).

Metropolis Generation Scheme

A Metropolis scheme (similar to methods employed in simulated annealing as in Laarhoven and Aarts, 1987) was also used to generate random mimetic Voronoi networks, since our previous efforts in applying a Monte Carlo fiber length generation scheme to these networks proved to have mixed results in matching fiber length and nodal degree distributions. In our Metropolis algorithmic scheme (Metropolis et al., 1953), a set of nodal positions was first extracted from an actual Voronoi network that had been generated from a random set of seed points in a 2-unit cube (n=3). From this set of nodes, fibers were turned on/off using a Metropolis scheme. In this scheme, possible fibers were randomly selected and turned on/off if adding/subtracting the fiber reduced the total system energy. If the change (turning the fiber on/off) increased the total system energy, the change could have still been enacted based on a random draw from 0-1 that was compared against a test probability (p) that was exponentially related (where $p = \exp[-k \Delta E]$ and scaled via a chosen parameter k=0.25) to the change in energy (ΔE) of the system (e.g. the larger the positive change in energy, the smaller the chance that the fiber would actually be added). Otherwise, the change was not enacted. The goal of the scheme was to diminish the total system energy by turning fibers on/off based on their contributions to the system energy. The system energy was calculated as the total of the (a) the sum of squared errors between the current and target nodal degree distributions

and (b) the sum of squared errors between the current and target fiber length distribution. This method thus made use of both fiber length as well as nodal degree distributions. The algorithm was started with an initial state of zero fibers. Once this algorithm converged to an equilibrium energy, the 2-unit cube network (n=3) was clipped to a 1-unit cube (to reduce edge effects) and then compared to actual Voronoi networks.

6.2.2 Mechanical Characterization of Networks

Networks were clipped to a 1-unit cube and stretched along a single axis with free transverse surfaces. The resulting stress-strain responses and Poisson ratios were compared. Fiber force was modeled as:

$$F = EA(\exp[B\,\varepsilon_G] - 1)/B \qquad (6\text{-}1)$$

where F (fiber force) varies with E (small-strain fiber modulus=13.9 MPa), B (fit constant=3.8), A (fiber area), and ε_G (fiber Green strain) with values from a prior model fit for collagen (Sander et al., 2009b). The network stress was calculated using a volume-averaging scheme as described in (Stylianopoulos and Barocas, 2007b).

6.3 Results and Discussion

Voronoi and Delaunay fiber length distributions represented a small subset of all possible fiber lengths within their set of network nodes (Fig. 6.2). Delaunay fibers comprised 3.6% while Voronoi fibers comprised only 0.2% of all possible fibers. Fiber-length-

specific probabilities for each case (Fig. 6.3) also varied, with Voronoi networks comprised of smaller fibers with less spread than Delaunay ones. It is important to note that Figure 6.3 is not a probability density function. It represents the fraction of possible fibers in the graphs that actually exist for any given length.

Monte Carlo Fiber Length Generation Scheme

Delaunay-like networks generated via the Monte Carlo fiber length method compared favorably to the actual case in terms of fiber length and nodal degree distributions (Fig. 6.4). However, the generated networks showed greater spread in nodal degree (stdev=2.13), though the degree distribution mode and means were similar.

Generated Voronoi-like networks compared favorably to the actual case in terms of fiber length distributions but failed to mimic the fixed nodal degree of actual networks (Fig. 6.5). However, the generated mean nodal degree (mean degree=4.03) was similar to the actual (degree=4.00) singular value.

Generated Delaunay networks closely matched their target networks in terms of their stress-stretch and Poisson response (Fig. 6.6). However, generated Voronoi networks showed greater deviation from target values, with a smaller Poisson ratio and a smaller peak Cauchy stress σ_{11} at a 30% network stretch, likely due to differences in nodal degree.

Metropolis Generation Scheme

Voronoi networks generated via the Metropolis scheme (Fig. 6.7) closely matched actual nodal degree and fiber length distributions for target Voronoi networks (Fig. 6.8). This is not surprising given that dissimilarity in the actual and target nodal degree and fiber length distributions was used to calculate the system energy for the generating algorithm. Also, nodal positions from target networks were used as starting points in the algorithm. The generating algorithm converged to an equilibrium energy after several million iterations (Fig. 6.9).

However, the mechanical response of these generated networks were quite dissimilar from actual Voronoi networks (Fig. 6.10). Over a 20% fixed face network stretch in the 1-axis, the Cauchy σ_{11} for the mimetic networks reached less than 15% of the peak stress generated by the target Voronoi networks. This is especially surprising given that the nodal degree distribution for the generated networks includes some high degree nodes (degree > 4) as compared to actual networks. Part of this diminished stiffness may be due to the non-uniform distribution of fibers throughout the generated network volume as compared to actual Voronoi networks. This appears to give rise to clusters of fibers in generated networks that are only loosely connected to each other within the volume, which may lead to fiber rotation and displacement (and diminished fiber forces generated) rather than fiber stretch during network deformations.

Conclusion

Our fiber-length based random network generation scheme (Monte Carlo method) produced Delaunay analogs that mimicked target networks in terms of fiber length, nodal degree, and mechanics. Generated Voronoi networks (also via the Monte Carlo method) showed distinct differences from targets, likely due to a variant degree distribution and sparse fibers. The Metropolis scheme produced generated Voronoi fiber length and nodal degree distributions that better matched actual Voronoi networks. However, the mechanical response of these networks were quite dissimilar from actual networks (far less stiff over a 20% fixed-face network stretch) despite these topological similarities.

We conclude that specifying a length distribution and total fiber density may not be sufficient in determining mechanical properties and that nodal degree must also be considered. Spectral methods and additional network statistics (such as tortuosity, mean path length, and fiber density throughout the network volume) may prove to be vital in generating improved mimetic networks.

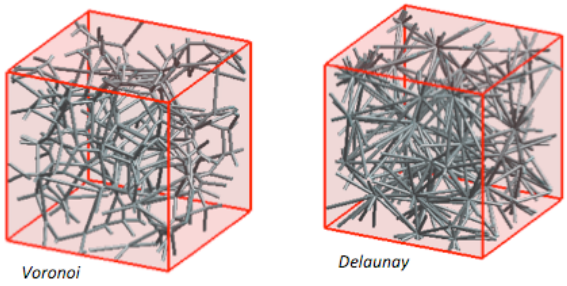

Fig. 6.1: Sample clipped Delaunay and Voronoi networks. Both network topologies (which are well characterized, readily generated, and already used to model fibrous tissues) were used as targets for our network generation scheme in the current study.

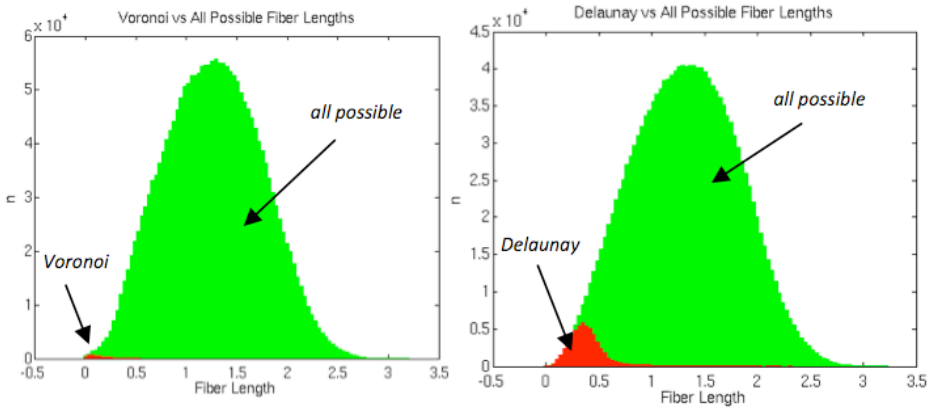

Fig. 6.2: Fiber length distributions (lengths of all possible fibers between network nodal positions) varied by network type. Voronoi fibers represented a much smaller portion of possible fiber lengths, owing to a smaller nodal degree (nodal degree = 4) as compared to networks generated by Delaunay triangulations (mean nodal degree ≈ 16).

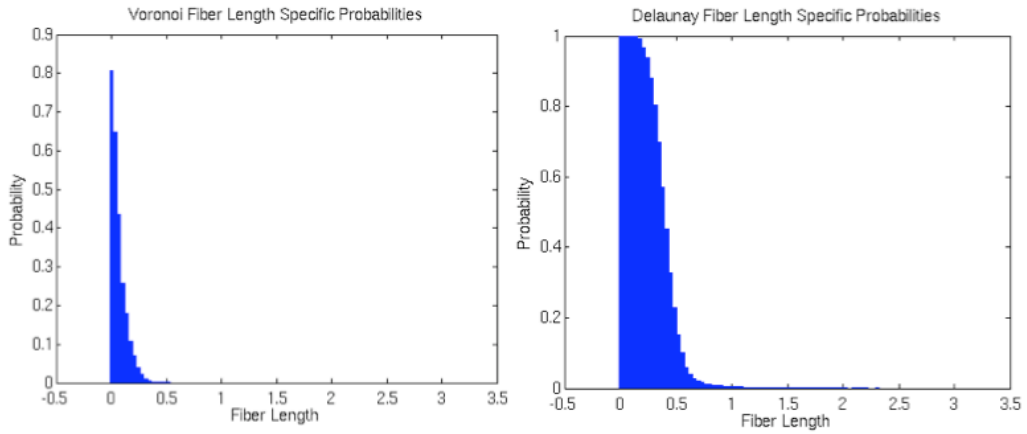

Fig. 6.3: Fiber-length-specific probability differed by network type. These are not probability density functions, but rather, represent the percentage of extant fibers of a given length taken from all possible fibers of similar length.

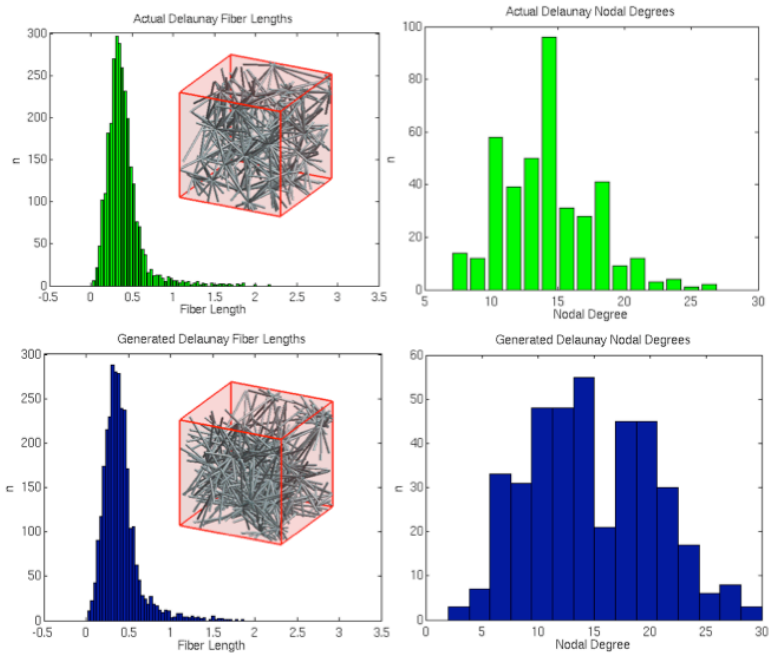

Fig. 6.4: Generated Delaunay networks (created via the Monte Carlo scheme) compared to actual networks with fiber length and nodal degree distributions plotted alongside a representative network for each case.

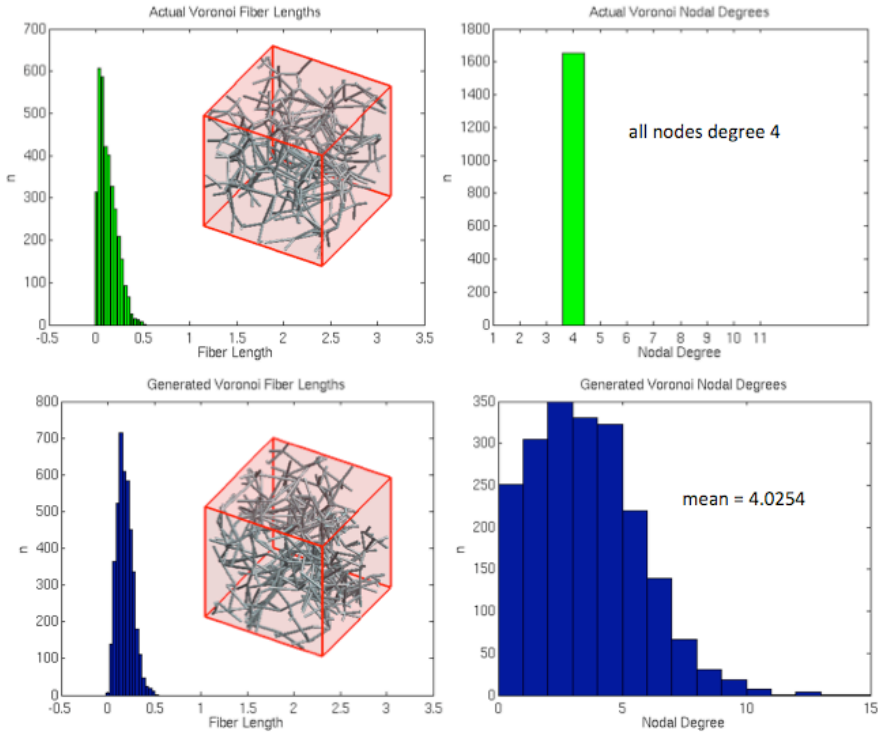

Fig. 6.5: Generated Voronoi networks (created via the Monte Carlo scheme) compared to actual networks with fiber length and nodal degree distributions plotted alongside.

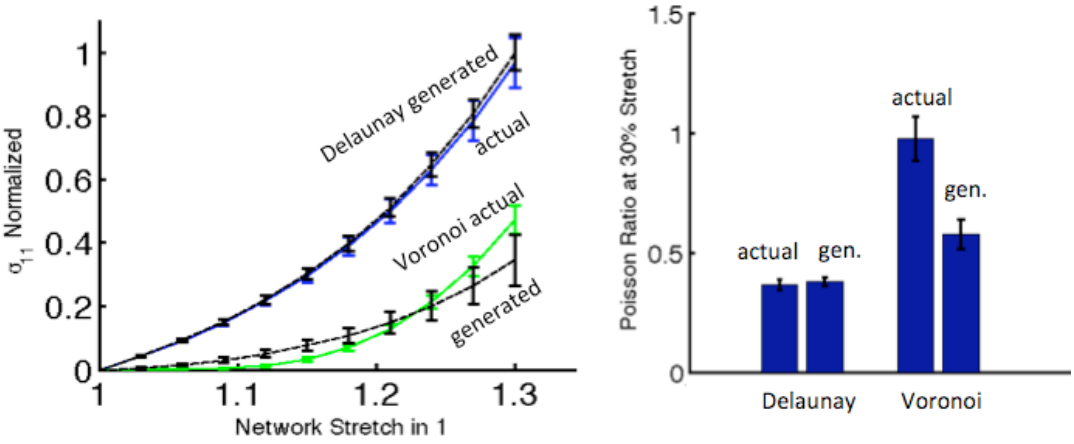

Fig. 6.6: Network stress-stretch response and Poisson ratios for generated networks (created via the Monte Carlo scheme) and for actual networks (95% CIs given).

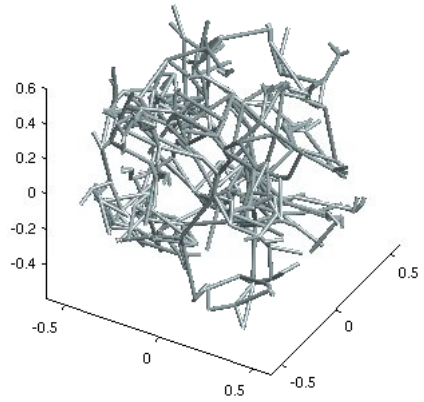

a) network generated by Metropolis method

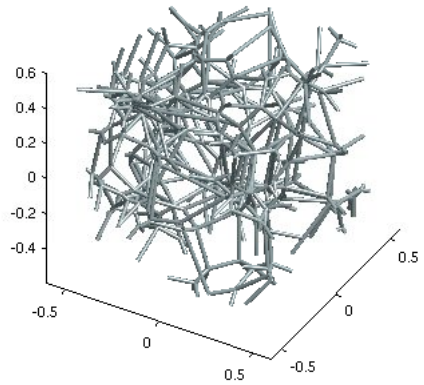

b) actual Voronoi network

Fig. 6.7: Generated Voronoi network (created via the Metropolis scheme) plotted above an actual Voronoi network for comparison. Both networks have similar nodal degree and fiber length distributions as well as fiber orientation tensors, but still retain visual dissimilarities.

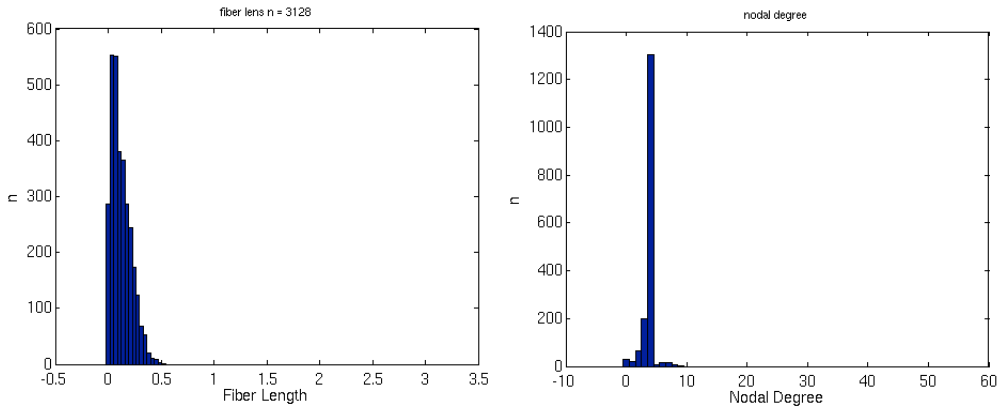

Fig. 6.8: Fiber length and nodal degree distributions for a generated Voronoi network (created via the Metropolis scheme) closely resemble actual Voronoi distributions.

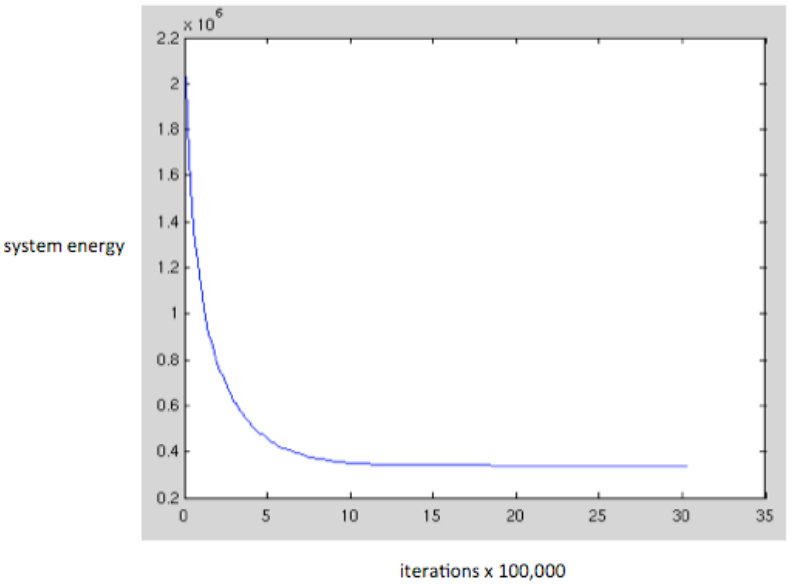

Fig. 6.9: System energy in the Metropolis network generation scheme reaches equilibrium over several million iterations of the generation algorithm.

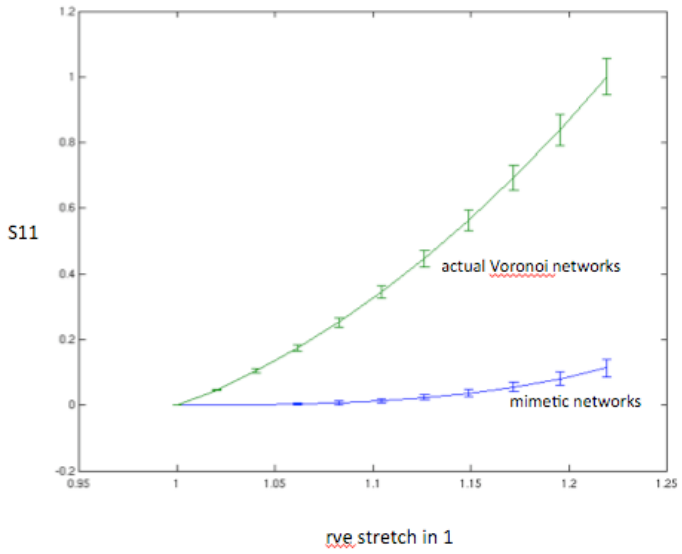

Fig. 6.10: The mechanical response of generated Voronoi networks (created via the Metropolis scheme) as compared to actual Voronoi networks. The network Cauchy S_{11} is plotted for a fixed face stretch for each network type (95% CIs given).

7. Conclusions and Future Work

The multiscale models for the degradation, damage, and failure of collagen-based materials presented in the current dissertation help frame an understanding of these processes in native and engineered soft tissues. Fiber-based rules at the microscale (such as strain-dependent diameter change or stretch-dependent failure) can substantially affect the macroscale mechanics of collagenous tissues and tissue analogs (Hadi et. 2012a; Hadi et al., 2012b). Microscale properties, such as fiber alignment or network topology, also play a major role in determining macroscale properties such as maximum strain at failure or measures of material stiffness for tissues (Hadi and Barocas, 2013a). Non-fibrillar components, such as matrix and cells, shape the pre-failure mechanics of tissues and likely also affect the failure properties of tissues (Lake et al., 2012a; Lai et al., 2013).

One logical extension to the studies presented would be to the consider the role of non-fibrillar and non-collagenous components in tissue failure. Native and engineered tissues can contain multiple fibers (such as elastin and fibrin) and multiple non-fibrillar components (cells and proteoglycans) that may fail dissimilarly to collagen fibers (Black et al., 2008; Ritter et al., 2009). Many of these components likely fail prior to the failure of collagen fibers and may play a large role in determining the failure properties of tissues. Modeling the failure of these components in tandem with the failure of collagen fibers may allow for the modeling of more complex tissue systems. Insight into the

microstructural failure of non-fibrillar tissue components could also help build improved models for tissue failure over multiple length scales.

Another area for future work is in the area of generating mimetic networks for multiscale tissue models. The approaches presented in this dissertation for generating mimetic networks for Delaunay and Voronoi networks are compelling, but lack fidelity in many instances (Hadi and Barocas, 2013b). It is also not certain if such methods would be applicable to physiologic collagen networks in native and engineered tissues. Testing these methods with networks reconstructed from confocal microscopy of actual tissues would be important future work in helping validate and extend these approaches to real biological networks (Stein et al., 2008; Lai et al., 2012a). Several network properties (statistical or perhaps derived through spectral methods) that have yet to be considered in the present studies may offer vastly improved approaches or metrics for generating mimetic networks for target networks of interest.

Bibliography

Ackbarow, T., Sen, D., Thaulow, C., Buehler, M. J., 2009. Alpha-helical protein networks are self-protective and flaw-tolerant. PLoS One 4, 6015.

Adeeb, S., Ali, A., Shrive, N., Frank, C., Smith, D., 2004. Modelling the behaviour of ligaments: a technical note. Computer Methods in Biomechanics and Biomedical Engineering 7, 33.

Adiguzel, E., Ahmad, P. J., Franco, C., Bendeck, M. P., 2009. Collagens in the progression and complications of atherosclerosis. Vascular Medicine 14, 73.

Amoroso, N. J., D'Amore, A., Hong, Y., Wagner, W. R., Sacks, M. S., 2011. Elastomeric electrospun polyurethane scaffolds: the interrelationship between fabrication conditions, fiber topology, and mechanical properties. Advanced Materials 23, 106.

Anssari-Benam, A., Gupta, H. S., Screen, H. R., 2012. Strain transfer through the aortic valve. Journal of Biomechanical Engineering 134, 061003.

Arruda, E. M., Boyce, M. C., 1993. A three-dimensional constitutive model for the large stretch behavior of rubber elastic materials. Journal of the Mechanics and Physics of Solids 41, 389.

Ault, H. K., Hoffman, A. H., 1992. A composite micromechanical model for connective tissues: Part I--theory. Journal of Biomechanical Engineering 114, 137.

Ault, H. K., Hoffman, A. H., 1992. A composite micromechanical model for connective tissues: Part II--application to rat tail tendon and joint capsule. Journal of Biomechanical Engineering 114, 142.

Ayturk, U. M., Gadomski, B., Schuldt, D., Patel, V., Puttlitz, C. M., 2012. Modeling degenerative disk disease in the lumbar spine: A combined experimental, constitutive, and computational approach. Journal of Biomechanical Engineering 134, 101003.

Barber, C. B., Dobkin, D. P., Huhdanpaa, H., 1996. The quickhull algorithm for convex hulls. ACM Transactions on Mathematical Software (TOMS) 22, 469.

Barocas, V. H., Tranquillo, R. T., 1997. An anisotropic biphasic theory of tissue-equivalent mechanics: the interplay among cell traction, fibrillar network deformation, fibril alignment, and cell contact guidance. Journal of Biomechanical Engineering 119, 137.

Bates, J. H. T., 2007. A recruitment model of quasi-linear power-law stress adaptation in lung tissue. Annals of Biomedical Engineering 35, 1165.

Becker, A. M., Ziff, R. M., 2009. Percolation thresholds on two-dimensional Voronoi networks and Delaunay triangulations. Physical Review E 80, 041101.

Benkherourou, M., Rochas, C., Tracqui, P., Tranqui, L., Guméry, P. Y., 1999. Standardization of a method for characterizing low-concentration biogels: elastic properties of low-concentration agarose gels. Journal of Biomechanical Engineering 121, 184.

Bhole, A. P., Flynn, B. P., Liles, M., Saeidi, N., Dimarzio, C. A., Ruberti, J. W., 2009. Mechanical strain enhances survivability of collagen micronetworks in the presence of collagenase: implications for load-bearing matrix growth and stability. Philosophical Transactions of the Royal Society A 367, 3339.

Billiar, K. L., Sacks, M. S., 2000. Biaxial mechanical properties of the native and glutaraldehyde-treated aortic valve cusp: Part II—A structural constitutive model. Journal of Biomechanical Engineering 122, 327.

Billiar, K. L., Sacks, M. S., 1997. A method to quantify the fiber kinematics of planar tissues under biaxial stretch. Journal of Biomechanics 30, 753.

Bischoff, J. E., Arruda, E. M., Grosh, K., 2002. A microstructurally based orthotropic hyperelastic constitutive law. Journal of Applied Mechanics 69, 570.

Black, L. D., Allen, P. G., Morris, S. M., Stone, P. J., Suki, B., 2008. Mechanical and failure properties of extracellular matrix sheets as a function of structural protein composition. Biophysical Journal 94, 1916.

Bonet, J., Wood, R. D., 1997. Nonlinear continuum mechanics for finite element analysis. Cambridge University Press, 1st edition.

Breuls, R. G. M., Sengers, B. G., Oomens, C. W. J., Bouten, C. V. C., Baaijens, F. P. T., 2002. Predicting local cell deformations in engineered tissue constructs: a multilevel finite element approach. Journal of Biomechanical Engineering, 124, 198.

Buehler, M. J., 2006. Nature designs tough collagen: Explaining the nanostructure of collagen fibrils. Proceedings of the National Academy of Sciences 103, 12285.

Burridge, K., Fath, K., Kelly, T., Nuckolls, G., Turner, C., 1988. Focal adhesions: transmembrane junctions between the extracellular matrix and the cytoskeleton. Annual Review of Cell Biology 4, 487.

Chan, C. E., Odde, D. J., 2008. Traction dynamics of filopodia on compliant substrates. Science 322, 1687.

Chandran, P. L., Barocas, V. H., 2007. Deterministic material-based averaging theory model of collagen gel micromechanics. Journal of Biomechanical Engineering 129, 137.

Chandran, P. L., Barocas, V. H., 2006. Affine versus non-affine fibril kinematics in collagen networks: theoretical studies of network behavior. Journal of Biomechanical Engineering 128, 259.

Chandran, P. L., Barocas, V. H., 2004. Microstructural mechanics of collagen gels in confined compression: poroelasticity, viscoelasticity, and collapse. Journal of Biomechanical Engineering 126, 152.

Cheng, V. W. T., Screen, H. R. C., 2007. The micro-structural strain response of tendon. Journal of Materials Science 42, 8957.

Collins, J. M., Ramamoorthy, K., Silveira, A. D., Patston, P., Mao, J. J., 2005. Expression of matrix metalloproteinase genes in the rat intramembranous bone during postnatal growth and upon mechanical stresses. Journal of Biomechanics 38, 485.

Cortes, D. H. and Elliott, D. M., 2012. Extra-fibrillar matrix mechanics of annulus fibrosus in tension and compression. Biomechanics and Modeling in Mechanobiology 11, 781.

Coughlin, M. F., Stamenović, D., 1998. A tensegrity model of the cytoskeleton in spread and round cells. Journal of Biomechanical Engineering 120, 770.

Cumming, B., McElwain, D., Upton, Z., 2010. A mathematical model of wound healing and subsequent scarring. Journal of the Royal Society Interface 7, 19.

Cummings, C. L., Gawlitta, D., Nerem, R. M., Stegemann, J. P., 2004. Properties of engineered vascular constructs made from collagen, fibrin, and collagen–fibrin mixtures. Biomaterials 25, 3699.

D'Amore, A., Stella, J. A., Wagner, W. R., Sacks, M. S., 2010. Characterization of the complete fiber network topology of planar fibrous tissues and scaffolds. Biomaterials 31, 5345.

De Vita, R., Slaughter, W. S., 2007. A constitutive law for the failure behavior of medial collateral ligaments. Biomechanics and Modeling in Mechanobiology 6, 189.

Driessen, N. J., Bouten, C. V., Baaijens, F. P., 2005. A structural constitutive model for collagenous cardiovascular tissues incorporating the angular fiber distribution. Journal of Biomechanical Engineering 127, 494.

Driessen, N. J., Cox, M. A., Bouten, C. V. Baaijens, F. P., 2008. Remodeling of the angular collagen fiber distribution in cardiovascular tissues. Biomechanics and Modeling in Mechanobiology 7, 93.

Driessen, N. J., Wilson, W., Bouten, C. V., Baaijens, F. P., 2004. A computational model for collagen fibre remodelling in the arterial wall. Journal of Theoretical Biology 226, 53.

Driessen, N. J., Mol, A., Bouten, C. V., Baaijens, F. P., 2007. Modeling the mechanics of tissue-engineered human heart valve leaflets. Journal of Biomechanics 40, 325.

Driessen, N. J., Boerboom, R. A., Huyghe, J. M., Bouten, C. V., Baaijens, F. P., 2003. Computational analyses of mechanically induced collagen fiber remodeling in the aortic heart valve. Journal of Biomechanical Engineering 125, 549.

Durrant, L. A., Archer, C. W., Benjamin, M., Ralphs, J. R., 1999. Organisation of the chondrocyte cytoskeleton and its response to changing mechanical conditions in organ culture. Journal of Anatomy 194, 343.

Eastwood, M., Mudera, V. C., Mcgrouther, D. A., Brown, R. A., 1998. Effect of precise mechanical loading on fibroblast populated collagen lattices: morphological changes. Cell Motility and the Cytoskeleton 40, 13.

Eggli, P. S., Hunzinker, E. B., Schenk, R. K., 1988. Quantitation of structural features characterizing weight- and less-weight-bearing regions in articular cartilage: a stereological analysis of medical femoral condyles in young adult rabbits. Anatomical Record 222, 217.

Engler, A. J., Sen, S., Sweeney, H. L., Discher, D. E., 2006. Matrix elasticity directs stem cell lineage specification. Cell 126, 677.

Ernst, G., Vogler, M., Huhne, C., Rolfes, R., 2010. Multiscale progressive failure analysis of textile composites. Composites Science and Technology 70, 61.

Evans, M. C., Barocas, V. H., 2009. The modulus of fibroblast-populated collagen gels is not determined by final collagen and cell concentration: experiments and an inclusion-based model. Journal of Biomechanical Engineering 131, 101014.

Flynn, B. P., Bhole, A. P., Saeidi, N., Liles, M., DiMarzio, C. A., Ruberti, J. W., Orgel, J. P. R. O., 2010. Mechanical Strain Stabilizes Reconstituted Collagen Fibrils against Enzymatic Degradation by Mammalian Collagenase Matrix Metalloproteinase 8 (MMP-8). PloS One 5, e12337.

Fung, Y. C., 1993. Biomechanics: Mechanical Properties of Living Tissues. Springer: New York, 2nd Edition.

Fung, Y. C., 1967. Elasticity of Soft Tissues in Simple Elongation. American Journal of Physiology 213, 1532.

Galis, Z. S., Khatri, J. J., 2002. Matrix metalloproteinases in vascular remodeling and atherogenesis: the good, the bad, and the ugly. Circulation Research 90, 251.

Gasser, T. C., Ogden, R. W., Holzapfel, G. A., 2006. Hyperelastic modelling of arterial layers with distributed collagen fibre orientations. Journal of the Royal Society Interface 3, 15.

Gibson, L. J., Ashby, M. F., 1997. Cellular Solids: Structure and Properties. Cambridge University Press: United Kingdom, 2nd edition.

Gilbert, T. W., Sacks, M. S., Grashow, J. S., Savio, L. Y. W., Badylak, S. F., Chancellor, M. B., 2006. Fiber kinematics of small intestinal submucosa under biaxial and uniaxial stretch. Journal of Biomechanical Engineering 128, 890.

Goffin, J. M., Pittet, P., Csucs, G., Lussi, J. W., Meister, J. J., Hinz, B., 2006. Focal adhesion size controls tension-dependent recruitment of α-smooth muscle actin to stress fibers. The Journal of Cell Biology 172, 259.

Guerin, H.L., Elliott, D. M., 2007. Quantifying the contributions of structure to annulus fibrosus mechanical function using a nonlinear, anisotropic, hyperelastic model. Journal of Orthopaedic Research 25, 508.

Guerin, H. A., Elliott, D. M., 2006. Degeneration affects the fiber reorientation of human annulus fibrosus under tensile load. Journal of Biomechanics 39, 1410.

Guilak, F., Mow, V. C., 2000. The mechanical environment of the chondrocyte: a biphasic finite element model of cell–matrix interactions in articular cartilage. Journal of Biomechanics 33, 1663.

Hadi, M. F., Sander, E. A., Ruberti, J. W., Barocas, V. H., 2012a. Simulated remodeling of loaded collagen networks via strain-dependent enzymatic degradation and constant-rate fiber growth. Mechanics of Materials 44, 72.

Hadi, M. F., Sander, E. A., Barocas, V. H., 2012b. Multiscale model predicts tissue-level failure from collagen fiber-level damage. Journal of Biomechanical Engineering 134, 091005.

Hadi, M. F., Barocas, V. H., 2013a. Microscale fiber network alignment affects macroscale failure behavior in simulated collagen tissue analogs. Journal of Biomechanical Engineering 135, 021026.

Hadi, M. F., Barocas, V. H., 2013b. Generating random fiber network topologies that mimic previously characterized networks. SBC2013-14615, ASME Summer Bioengineering Conference, Sunriver, OR.

Hadjipanayi, E., Mudera, V., Brown, R. A., 2009. Guiding cell migration in 3d: a collagen matrix with graded directional stiffness. Cell Motility and the Cytoskeleton 66, 121.

Hamed, E., Jasiuk, I., Yoo, A., Lee, Y. H., Liszka, T., 2012. Multi-scale modelling of elastic moduli of trabecular bone. Journal of the Royal Society Interface 9, 1654.

Hang, F., Barber, A. H., 2011. Nano-mechanical properties of individual mineralized collagen fibrils from bone tissue. Journal of the Royal Society Interface 8, 500.

Hashin, Z., 1962. The elastic moduli of heterogeneous materials. Journal of Applied Mechanics 29, 143.

Hepworth, D. G., Steven-Fountain, A., Bruce, D. M., Vincent, J. F., 2001. Affine versus non-affine deformation in soft biological tissues, measured by the reorientation and stretching of collagen fibres through the thickness of compressed porcine skin. Journal of Biomechanics 34, 341.

Hewitt, J., Guilak, F., Glisson, R., Vail, T. P., 2001. Regional material properties of the human hip joint capsule ligaments. Journal of Orthopaedic Research 19, 359.

Holmes, J. W., Borg, T. K., Covell, J. W., 2005. Structure and mechanics of healing myocardial infarcts. Annual Review of Biomedical Engineering 7, 223.

Holzapfel, G.A., Gasser, T. C., Ogden, R. W., 2000. A new constitutive framework for arterial wall mechanics and a comparative study of material models. Journal of Elasticity 61, 1.

Holzapfel, G.A., 2000. Nonlinear Solid Mechanics: A Continuum Approach for Engineering. John Wiley and Sons: New Jersey, 1st edition.

Horowitz, A., Lanir, Y., Yin, F. C., Perl, M., Sheinman, I., Strumpf, R. K., 1988a. Structural three-dimensional constitutive law for the passive myocardium. Journal of Biomechanical Engineering 110, 200.

Horowitz, A., Sheinman, I., Lanir, Y., 1988b. Nonlinear incompressible finite element for simulating loading of cardiac tissue--Part II: Three dimensional formulation for thick ventricular wall segments. Journal of Biomechanical Engineering 110, 62.

Horowitz, A., Sheinman, I., Lanir, Y., 1988c. Nonlinear incompressible finite element for simulating loading of cardiac tissue--Part I: Two dimensional formulation for thin myocardial strips. . Journal of Biomechanical Engineering 110, 57.

Hu, J. J., Baek, S., Humphrey, J. D., 2007. Stress–strain behavior of the passive basilar artery in normotension and hypertension. Journal of Biomechanics 40, 2559.

Huang, D., Chang, T. R., Aggarwal, A., Lee, R. C., Ehrlich, H. P., 1993. Mechanisms and dynamics of mechanical strengthening in ligament-equivalent fibroblast-populated collagen matrices. Annals of Biomedical Engineering 21, 289.

Humphrey, J. D., 2003. Review paper: continuum biomechanics of soft biological tissues. Proceedings of the Royal Society of London. Series A: Mathematical, Physical and Engineering Sciences 459, 3.

Humphrey, J. D., Yin, F. C., 1989. Constitutive relations and finite deformations of passive cardiac tissue II: stress analysis in the left ventricle. Circulation Research 65, 805.

Hurschler, C., Loitz-Ramage, B., Vanderby Jr, R., 1997. A structurally based stress-stretch relationship for tendon and ligament. Journal of Biomechanical Engineering 119, 392.

Guilak, F., Mow, V. C., 2000. The mechanical environment of the chondrocyte: a biphasic finite element model of cell–matrix interactions in articular cartilage. Journal of Biomechanics 33, 1663.

Isambert, H., Maggs, A. C., 1996. Dynamics and rheology of actin solutions. Macromolecules 29, 1036.

Ito, S., Ingenito, E. P., Brewer, K. K., Black, L. D., Parameswaran, H., Lutchen, K. R., Suki, B., 2005. Mechanics, nonlinearity, and failure strength of lung tissue in a mouse model of emphysema: possible role of collagen remodeling. Journal of Applied Physiology 98, 503.

Janmey, P. A., McCulloch, C. A., 2007. Cell mechanics: integrating cell responses to mechanical stimuli. Annual Review of Biomedical Engineering 9, 1.

Jhun, C. S., Evans, M. C., Barocas, V. H., Tranquillo, R. T., 2009. Planar Biaxial Mechanical Behavior of Bioartificial Tissues Possessing Prescribed Fiber Alignment. Journal of Biomechanical Engineering 131, 081006.

Julkunen, P., Harjula, T., Marjanen, J., Helminen, H. J., Jurvelin, J. S., 2009. Comparison of single-phase isotropic elastic and fibril-reinforced poroelastic models for indentation of rabbit articular cartilage. Journal of Biomechanics 42, 652.

Kabla, A., Mahadevan, L., 2007. Nonlinear mechanics of soft fibrous networks. Journal of the Royal Society Interface 4, 99.

Kang, J., Steward, R. L., Kim, Y., Schwartz, R. S., LeDuc, P. R., Puskar, K. M., 2011. Response of an actin filament network model under cyclic stretching through a coarse grained Monte Carlo approach. Journal of Theoretical Biology 274, 109.

Kao, P. H., Lammers, S., Tian, L., Hunter, K., Stenmark, K. R., Shandas, R., Qi, H. J., 2011. A microstructurally-driven model for pulmonary artery tissue. Journal of Biomechanical Engineering 133, 051002.

Keten, S., Bertaud, J., Sen, D., Xu, Z., Ackbarow, T., Buehler, M. J., 2010. Multiscale modeling of biological protein materials–deformation and failure. Trends in Computational Nanomechanics 9, 473.

Keyes, J. T., Haskett, D. G., Utzinger, U., Azhar, M., Vande Geest, J. P., 2011. Adaptation of a planar microbiaxial optomechanical device for the tubular biaxial microstructural and macroscopic characterization of small vascular tissues. Journal of Biomechanical Engineering 133, 075001.

Kiviranta, P., Rieppo, J., Korhonen, R. K., Julkunen, P., Toyras, J., Jurvelin, J. S., 2006. Collagen network primarily controls poisson's ratio of bovine articular cartilage in compression. Journal of Orthopaedic Research 24, 690.

Kuhl, E., Garikipati, K., Arruda, E. M., Grosh, K., 2005. Remodeling of biological tissue: Mechanically induced reorientation of a transversely isotropic chain network. Journal of the Mechanics and Physics of Solids 53, 1552.

Laarhoven, P. J. M. van, Aarts, E. H. L., 1987. Simulated Annealing: Theory and Applications. Springer: New York, 1st edition.

Lai, V. K., Hadi, M. F., Tranquillo, R. T., Barocas, V. H., 2013. A multiscale approach to modeling the passive mechanical contribution of cells in tissues. Journal of Biomechanical Engineering, accepted May 2013.

Lai, V. K., Frey, C. R., Kerandi, A. M., Lake, S. P., Tranquillo, R. T., Barocas, V. H., 2012a. Microstructural and Mechanical Differences Between Digested Collagen–Fibrin Co-Gels and Pure Collagen and Fibrin Gels. Acta Biomaterialia 8, 4031.

Lai, V. K., Lake, S. P., Frey, C. R., Tranquillo, R. T., Barocas, V. H., 2012b. Mechanical behavior of collagen-fibrin co-gels reflects transition from series to parallel interactions with increasing collagen content. Journal of Biomechanical Engineering 134, 011004.

Lake, S. P., Hadi, M. F., Lai, V. K., Barocas, V. H., 2012a. Mechanics of a fiber network within a non-fibrillar matrix: Model and comparison with collagen-agarose co-gels. Annals of Biomedical Engineering 40, 2111.

Lake, S. P., Cortes, D. H., Kadlowec, J. A., Soslowsky, L. J., Elliott, D. M., 2012b. Evaluation of affine fiber kinematics in human supraspinatus tendon using quantitative projection plot analysis. Biomechanics and Modeling in Mechanobiology 11, 197.

Lake, S. P., Barocas, V. H., 2011a. Mechanical and structural contribution of non-fibrillar extracellular matrix in uniaxial tension: a collagen-agarose co-gel model. Annals of Biomedical Engineering 39, 1891.

Lake, S. P., Hald, E. S., Barocas, V. H., 2011b. Collagen-agarose co-gels as a model for collagen-matrix interaction in soft tissues subjected to indentation. Journal of Biomedical Materials Research Part A, 99, 507.

Lake, S. P., Miller, K. S., Elliott, D. M., Soslowsky, L. J., 2010. Tensile properties and fiber alignment of human supraspinatus tendon in the transverse direction demonstrate inhomogeneity, nonlinearity, and regional isotropy. Journal of Biomechanics 43, 727.

Lake, S. P., Miller, K. S., Elliott, D. M., Soslowsky, L. J., 2009. Effect of fiber distribution and realignment on the nonlinear and inhomogeneous mechanical properties of human supraspinatus tendon under longitudinal tensile loading. Journal of Orthopaedic Research 27, 1596.

Lake, S.P., 2009. Anisotropic, inhomogeneous and non-linear structure-function of human supraspinatus tendon, in Ph.D. Thesis, University of Pennsylvania: Philadelphia, PA.

Lanir, Y., 1979. A structural theory for the homogeneous biaxial stress-strain relationships in flat collagenous tissues. Journal of Biomechanics 12, 423.

Lauer-Fields, J. L., Juska, D., Fields, G. B., 2002. Matrix metalloproteinases and collagen catabolism. Peptide Science 66, 19.

Legant, W. R., Miller, J. S., Blakely, B. L., Cohen, D. M., Genin, G. M., Chen, C. S., 2010. Measurement of mechanical tractions exerted by cells in three-dimensional matrices. Nature Methods 7, 969.

Liao, H., Belkoff, S. M., 1999. A failure model for ligaments. Journal of Biomechanics 32, 183.

Luo, X. J., Stylianopoulos, T., Barocas, V. H., Shephard, M. S., 2009. Multiscale computation for bioartificial soft tissues with complex geometries. Engineering with Computers 25, 87.

Lynch, H. A., Johannessen, W., Wu, J. P., Jawa, A., Elliott, D. M., 2003. Effect of fiber orientation and strain rate on the nonlinear uniaxial tensile material properties of tendon. Journal of Biomechanical Engineering 125, 726.

Maceri, F., Marino, M., Vairo, G., 2010. A unified multiscale mechanical model for soft collagenous tissues with regular fiber arrangement. Journal of Biomechanics 43, 355.

Madden, J. W., Peacock Jr, E. E., 1971. Studies on the biology of collagen during wound healing. 3. Dynamic metabolism of scar collagen and remodeling of dermal wounds. Annals of Surgery 174, 511.

Maksym, G. N., Fredberg, J. J., Bates, J. H. T., 1998. Force heterogeneity in a two-dimensional network model of lung tissue elasticity. Journal of Applied Physiology 85, 1223.

Marquez, J. P., Genin, G. M., Zahalak, G. I., Elson, E. L., 2005a. The relationship between cell and tissue strain in three-dimensional bio-artificial tissues. Biophysical Journal 88, 778.

Marquez, J. P., Genin, G. M., Zahalak, G. I., Elson, E. L., 2005b. Thin bio-artificial tissues in plane stress: the relationship between cell and tissue strain, and an improved constitutive model. Biophysical Journal 88, 765.

Martufi, G., Gasser, T. C., 2011. A constitutive model for vascular tissue that integrates fibril, fiber and continuum levels with application to the isotropic and passive properties of the infrarenal aorta. Journal of Biomechanics 44, 2544.

Metropolis, N., Rosenbluth, A. W., Rosenbluth, M. N., Teller, A. H., Teller, E., 1953. Equations of state calculations by fast computing machines. Journal of Chemical Physics 21, 1087.

Moger, C., Arkill, K., Barrett, R., Bleuet, P., Ellis, R., Green, E., Winlove, C. P., 2009. Cartilage collagen matrix reorientation and displacement in response to surface loading. Journal of Biomechanical Engineering 131, 031008.

Nachtrab, S., Kapfer, S. C, Arns, C. H., Madadi, M., Mecke, K., Schroder-Turk, G. E., 2011. Morphology and linear-elastic moduli of random network solids. Advanced Materials 23, 2633.

Nagel, T., Kelly, D. J., 2010. The influence of fiber orientation on the equilibrium properties of neutral and charged biphasic tissues. Journal of Biomechanical Engineering 132, 114506.

Nagel, T., Kelly, D. J., 2012. Remodelling of collagen fibre transition stretch and angular distribution in soft biological tissues and cell-seeded hydrogels. Biomechanics and Modeling in Mechanobiology 11, 325.

Nerurkar, N. L., Baker, B. M., Sen, S., Wible, E. E., Elliott, D. M., Mauck, R. L., 2009. Nanofibrous biologic laminates replicate the form and function of the annulus fibrosus. Nature Materials 8, 986.

Nerurkar, N. L., Elliott, D. M., Mauck, R. L., 2007. Mechanics of oriented electrospun nanofibrous scaffolds for annulus fibrosus tissue engineering. Journal of Orthopaedic Research 25, 1018.

Nerurkar, N. L., Ramasubramanian, A., Taber, L. A., 2006. Morphogenetic adaptation of the looping embryonic heart to altered mechanical loads. Developmental Dynamics 235, 1822.

O'Connell, G. D., Guerin, H. L., Elliott, D. M., 2009. Theoretical and uniaxial experimental evaluation of human annulus fibrosus degeneration. Journal of Biomechanical Engineering 131, 111007.

Ofek, G., Wiltz, D. C., Athanasiou, K. A., 2009. Contribution of the cytoskeleton to the compressive properties and recovery behavior of single cells. Biophysical Journal 97, 1873.

Padala, M., Sacks, M. S., Liou, S. W., Balachandran, K., He, Z., Yoganathan, A. P., 2010. Mechanics of the mitral valve strut chordae insertion region. Journal of Biomechanical Engineering 132, 081004.

Palmer, J. S., Boyce, M. C., 2008. Constitutive modeling of the stress–strain behavior of f-actin filament networks. Acta Biomaterialia 4, 597.

Pan, B., Asundi, A., Xie, H., Gao, J., 2009. Digital image correlation using iterative least squares and pointwise least squares for displacement field and strain field measurements. Optics and Lasers in Engineering 47, 865.

Pardo, A., Selman, M., 2005. MMP-1: the elder of the family. The International Journal of Biochemistry and Cell Biology 37, 283.

Peng, X. Q., Guo, Z. Y., Moran, B., 2006. An anisotropic hyperelastic constitutive model with fiber-matrix shear interaction for the human annulus fibrosus. Journal of Applied Mechanics 73, 815.

Phillippi, J. A., Pasta, S., Vorp, D. A., 2011. Biomechanics and pathobiology of aortic aneurysms. Biomechanics and Mechanobiology of Aneurysms 7, 67.

Pins, G. D., Huang, E. K., Christiansen, D. L., Silver, F. H., 1997. Effects of static axial strain on the tensile properties and failure mechanisms of self-assembled collagen fibers. Journal of Applied Polymer Science 63, 1429.

Pizzo, A. M., Kokini, K., Vaughn, L. C., Waisner, B. Z., Voytik-Harbin, S. L., 2005. Extracellular matrix (ECM) microstructural composition regulates local cell-ECM biomechanics and fundamental fibroblast behavior: a multidimensional perspective. Journal of Applied Physiology 98, 1909.

Purohit, P. K., Litvinov, R. I., Brown, A. E., Discher, D. E., Weisel, J. W., 2011. Protein unfolding accounts for the unusual mechanical behavior of fibrin networks. Acta Biomaterialia, 7, 2374.

Quapp, K. M., Weiss, J. A., 1998. Material characterization of human medial collateral ligament. Journal of Biomechanical Engineering, 120, 757.

Quinn, K. P., Winkelstein, B. A., 2008. Altered collagen fiber kinematics define the onset of localized ligament damage during loading. Journal of Applied Physiology 105, 1881.

Quinn, K. P., Winkelstein, B. A., 2011. Detection of altered collagen fiber alignment in the cervical facet capsule after whiplash-like joint retraction. Annals of Biomedical Engineering 39, 2163.

Raghupathy, R., Witzenburg, C., Lake, S. P., Sander, E. A., Barocas, V. H., 2011. Identification of regional mechanical anisotropy in soft tissue analogs. Journal of Biomechanical Engineering 133, 091011.

Raghupathy, R., Barocas, V. H., 2009. A closed-form structural model of planar fibrous tissue mechanics. Journal of Biomechanics 42, 1424.

Ramasubramanian, A., Taber, L. A., 2008. Computational modeling of morphogenesis regulated by mechanical feedback. Biomechanics and Modeling in Mechanobiology 7, 77.

Reese, S. P., Maas, S. A., Weiss, J. A., 2010. Micromechanical models of helical superstructures in ligament and tendon fibers predict large poisson's ratios. Journal of Biomechanics 43, 1394.

Ritter, M. C., Jesudason, R., Majumdar, A., Stamenovic, D., Buczek-Thomas, J. A., Stone, P. J., Nugent, M. A., Suki, B., 2009. A zipper network model of the failure mechanics of extracellular matrices. Proceedings of the National Academy of Sciences 106, 1081.

Robinson, P. S., Tranquillo, R. T., 2009. Planar biaxial behavior of fibrin-based tissue-engineered heart valve leaflets. Tissue Engineering Part A 15, 2763.

Robinson, P. S., Johnson, S. L., Evans, M. C., Barocas, V. H., Tranquillo, R. T., 2008. Functional tissue-engineered valves from cell-remodeled fibrin with commissural alignment of cell-produced collagen. Tissue Engineering Part A 14A, 83.

Roeder, B. A., Kokini, K., Sturgis, J. E., Robinson, J. P., Voytik-Harbin, S. L., 2002. Tensile mechanical properties of three-dimensional type I collagen extracellular matrices with varied microstructure. Journal of Biomechanical Engineering 124, 214.

Roy, S., Silacci, P., Stergiopulos, N., 2005. Biomechanical properties of decellularized porcine common carotid arteries. American Journal of Physiology Heart and Circulatory Physiology 289, H1567.

Ruberti, J. W., Hallab, N. J., 2005. Strain-controlled enzymatic cleavage of collagen in loaded matrix. Biochemical and Biophysical Research Communications 336, 483.

Sacks, M. S., Schoen, F. J., Mayer Jr, J. E., 2009. Bioengineering challenges for heart valve tissue engineering. Biomedical Engineering 11, 289.

Sander, E. A., Downs, J. C., Hart, R. T., Burgoyne, C. F., Nauman, E. A., 2006. A cellular solid model of the lamina cribrosa: Mechanical dependence on morphology. Journal of Biomechanical Engineering 128, 879.

Sander, E. A., Hadi, M. F., Barocas, V. H., 2011. Multiscale mechanical models for understanding microstructural damage in fibrous tissues. SBC2011-53781, ASME 2011 Summer Bioengineering Conference, Farmington, PA.

Sander, E. A., Barocas, V. H., 2008. Biomimetic collagen tissues: collagenous tissue engineering and other applications. Collagen: Structure and Mechanics, Springer: New York, 1st edition, 475-504.

Sander, E. A., Stylianopoulos, T., Tranquillo, R. T., Barocas, V. H., 2009a. Image-based biomechanics of collagen-based tissue equivalents: Multiscale models compared to fiber alignment predicted by polarimetric imaging. IEEE Engineering in Medicine and Biology Magazine: The Quarterly Magazine of the Engineering in Medicine & Biology Society 28, 10.

Sander, E. A., Stylianopoulos, T., Tranquillo, R. T., Barocas, V. H., 2009b. Image-based multiscale modeling predicts tissue-level and network-level fiber reorganization in stretched cell-compacted collagen gels. Proceedings of the National Academy of Sciences 106, 17675.

Sander, E., Barocas, V. H., 2009c. Comparison of 2D fiber network orientation measurement methods. Journal of Biomedical Materials Research Part A 88, 322.

Sander, E. A., Stein, A. M., Swickrath, M. J., Barocas, V. H., 2010. Out of Many, One: Modeling Schemes for Biopolymer and Biofibril Networks. Challenges and Advances in Computational Chemistry and Physics 9, 557.

Sastry, A., Cheng, X., Wang, C., 1998. Mechanics of stochastic fibrous networks. Journal of Thermoplastic Composite Materials 3, 288.

Satcher Jr, R. L., Dewey Jr, C. F., 1996. Theoretical estimates of mechanical properties of the endothelial cell cytoskeleton. Biophysical Journal 71, 109.

Shen, Z. L., Dodge, M. R., Kahn, H., Ballarini, R., Eppell, S. J., 2008. Stress-strain experiments on individual collagen fibrils. Biophysical Journal 95, 3956.

Spencer, T. J., Hidalgo-Bastida, L. A., Cartmell, S. H., Halliday, I., Care, C. M., 2012. In silico multi-scale model of transport and dynamic seeding in a bone tissue engineering perfusion bioreactor. Biotechnology and Bioengineering 110, 1221.

Stamenovic, D., Coughlin, M. F., 2000. A quantitative model of cellular elasticity based on tensegrity. Journal of Biomechanical Engineering 122, 39.

Stamenovic, D., Fredberg, J. J., Wang, N., Butler, J. P., Ingber, D. E., 1996. A microstructural approach to cytoskeletal mechanics based on tensegrity. Journal of Theoretical Biology 181, 125.

Stein, A. M., Vader, D. A., Jawerth, L. M., Weitz, D. A., Sander, L. M., 2008. An algorithm for extracting the network geometry of three-dimensional collagen gels. Journal of Microscopy 232, 462.

Stein, A. M., Vader, D. A., Weitz, D. A., Sander, L. M., 2010. The micromechanics of three-dimensional collagen-I gels. Complexity 16, 22.

Stevenson, M. D., Sieminski, A. L., McLeod, C. M., Byfield, F. J., Barocas, V. H., Gooch, K. J., 2010. Pericellular conditions regulate extent of cell-mediated compaction of collagen gels. Biophysical Journal 99, 19.

Storm, C., Pastore, J. J., MacKintosh, F. C., Lubensky, T. C., Janmey, P. A., 2005. Nonlinear elasticity in biological gels. Nature 435, 191.

Stylianopoulos, T., Barocas, V. H., 2007a. Multiscale, structure-based modeling for the elastic mechanical behavior of arterial walls. Journal of Biomechanical Engineering 129, 611.

Stylianopoulos, T., Barocas, V. H., 2007b. Volume-averaging theory for the study of the mechanics of collagen networks. Computer Methods in Applied Mechanics and Engineering 196, 2981.

Subramanian, A., Lin, H. Y., 2005. Crosslinked chitosan: its physical properties and the effects of matrix stiffness on chondrocyte cell morphology and proliferation. Journal of Biomedical Materials Research Part A 75A, 742.

Susilo, M. E., Roeder, B. A., Voytik-Harbin, S. L., Kokini, K., Nauman, E. A., 2010. Development of a three-dimensional unit cell to model the micromechanical response of a collagen-based extracellular matrix. Acta Biomaterialia 6, 1471.

Taber, L. A., Humphrey, J. D., 2001. Stress-modulated growth, residual stress, and vascular heterogeneity. Journal of Biomechanical Engineering 123, 528.

Tang, H., Buehler, M. J., Moran, B., 2009. A constitutive model of soft tissue: From nanoscale collagen to tissue continuum. Annals of Biomedical Engineering 37, 1117.

Tower, T. T., Neidert, M. R., Tranquillo, R. T., 2002. Fiber alignment imaging during mechanical testing of soft tissues. Annals of Biomedical Engineering 30, 1221.

Ulrich, T. A., Jain, A., Tanner, K., MacKay, J. L., Kumar, S., 2010. Probing cellular mechanobiology in three-dimensional culture with collagen-agarose matrices. Biomaterials 31, 1875.

Varner, V. D., Voronov, D. A., Taber, L. A., 2010. Mechanics of head fold formation: investigating tissue-level forces during early development. Development 137, 3801.

Wagner, D. R., Lotz, J. C., 2004. Theoretical model and experimental results for the nonlinear elastic behavior of human annulus fibrosus. Journal of Orthopaedic Research 22, 901.

Wagner, H. P., Humphrey, J. D., 2011. Differential passive and active biaxial mechanical behaviors of muscular and elastic arteries: Basilar versus common carotid. Journal of Biomechanical Engineering 133, 051009.

Wang, C. W., Sastry, A. M., 2000. Structure, mechanics and failure of stochastic fibrous networks: Part II—Network simulations and application. Journal of Engineering Materials and Technology 122, 460.

Wang, N., Naruse, K., Stamenovic, D., Fredberg, J. J., Mijailovich, S. M., Tolic-Norrelykke, I. M., Polte, T., Mannix, R., Ingber, D. E., 2001. Mechanical behavior in living cells consistent with the tensegrity model. Proceedings of the National Academy of Sciences 98, 7765.

Weber, K. T., 1997. Extracellular matrix remodeling in heart failure: a role for de novo angiotensin II generation. Circulation 96, 4065.

Weinberg, E. J., Shahmirzadi, D., Mofrad, M. R. K., 2010. On the multiscale modeling of heart valve biomechanics in health and disease. Biomechanics and Modeling in Mechanobiology 9, 373.

Wellen, J., Helmer, K. G., Grigg, P., Sotak, C. H., 2004. Application of porous-media theory to the investigation of water adc changes in rabbit achilles tendon caused by tensile loading. Journal of Magnetic Resonance 170, 49.

Wren, T. A., Yerby, S. A., Beaupré, G. S., Carter, D. R., 2001. Mechanical properties of the human achilles tendon. Clinical Biomechanics 16, 245.

Yeung, T., Georges, P. C., Flanagan, L. A., Marg, B., Ortiz, M., Funaki, M., Zahir, N., Ming, W., Weaver, V., Janmey, P. A., 2005. Effects of substrate stiffness on cell

morphology, cytoskeletal structure, and adhesion. Cell Motility and the Cytoskeleton 60, 24.

Zahalak, G. I., Wagenseil, J. E., Wakatsuki, T., Elson, E. L., 2000. A cell-based constitutive relation for bio-artificial tissues. Biophysical Journal 79, 2369.

Zahedmanesh, H., Lally, C., 2012. A multiscale mechanobiological modelling framework using agent-based models and finite element analysis: application to vascular tissue engineering. Biomechanics and Modeling in Mechanobiology 11, 363.

Zareian, R., Church, K. P., Saeidi, N., Flynn, B. P., Beale, J. W., Ruberti, J. W., 2010. Probing collagen/enzyme mechanochemistry in native tissue with dynamic, enzyme-induced creep. Langmuir 26, 9917.

Zhang, B., Yang, Z., Wu, Y., Sun, H., 2010. Hierarchical multiscale modeling of failure in unidirectional fiber-reinforced plastic matrix composite. Materials and Design 31, 2312.

Zhang, L., Lake, S. P., Lai, V. K., Picu, C. R., Barocas, V. H., Shephard, M. S., 2013. A coupled fiber-matrix model demonstrates highly inhomogeneous microstructural interactions in soft tissues under tensile load. Journal of Biomechanical Engineering 135, 011008.

Zohdi, T., 2007. A computational framework for network modeling of fibrous biological tissue deformation and rupture. Computer Methods in Applied Mechanics and Engineering 196, 2972.

Appendix I: A Multiscale Approach to Modeling the Passive Mechanical Contribution of Cells in Tissues

The content of this chapter was previously published as a research article in the *Journal of Biomechanical Engineering* by Lai, Hadi, Tranquillo, and Barocas (Lai et al., 2013).

Introduction

Understanding the mechanics of biological and bioengineered tissues is difficult; unlike synthetic composite materials (e.g. laminates), tissues are comprised of different components (cells, fibrous protein networks, proteoglycans) that are distributed inhomogeneously, exhibit non-linear mechanical behavior (Fung, 1967; Humphrey, 2003), and can be highly anisotropic. In particular, cells play a complex role in the mechanics of native and bioengineered tissues. In addition to a *passive* component of cells as inclusions within an extracellular matrix (ECM), *active* mechanical contributions also exist from the interactions between cells with the surrounding ECM (e.g., compaction, remodeling).

Early phenomenological and continuum modeling approaches to understand tissue biomechanics (Fung, 1967; Humphrey and Yin, 1989) considered both the cell and the matrix as continuous materials. Evolution of such models has generally involved incorporation of microstructural detail and/or cellular phenomenon to develop improved constitutive laws, e.g., models that incorporate fiber orientation distributions to capture anisotropic behavior of the ECM surrounding the cells (Gasser et al., 2006; Hu et al.,

2007; Wagner and Humphrey, 2011), incorporation of "anisotropy tensors" to account for cell orientation within a tissue (Barocas and Tranquillo, 1997; Marquez et al., 2005a, 2005b; Zahalak et al., 2000), or a mathematical model motivated by localized variations in the pericellular region (Guilak and Mow, 2000; Stevenson et al., 2010). In addition, multi-level finite element approaches have been used to account for tissue inhomogeneity by discretizing cells from the surrounding ECM to consider cells as separate entities (Breuls et al., 2002). While such models have had some success in predicting tissue mechanics, the lack of microstructural detail in their formulation limits their ability to explore the respective contributions and interactions between different components within a tissue. In contrast, structural approaches attempt to understand tissue biomechanics by incorporating microstructural details directly into the model to elucidate composition-structure-function relationships in biological tissues. One such model is the tensegrity approach by Ingber and co-workers, who proposed that cytoskeletal filaments and the ECM form a tensegrity structure in combination with one another (Coughlin and Stamenović, 1998; Stamenovic and Coughlin, 2000; Stamenović et al., 1996; Wang et al., 2001). The cellular solid model considered the cytoskeletal filaments as struts forming the edges of a cubic cell that can bend and stretch under deformation (Gibson and Ashby, 1999; Satcher Jr and Dewey Jr, 1996; Susilo et al., 2010). Biopolymer models (Isambert and Maggs, 1996; Storm et al., 2005) utilize flexible polymer theories by treating the single segments of the network as worm-like chains; Boyce and co-workers extended the concept to create an eight-chain volume-averaged network model (Palmer and Boyce, 2008). The above-mentioned models, while beginning to incorporate network

microstructure detail into the model formulation, contain simplified network representations that assume ordered periodicity within the network.

Research in our group focuses on developing a comprehensive model to predict the mechanical behavior of biological and bioengineered tissues via a multiscale approach, with the fibrillar components of the ECM represented as large random interconnected networks. Multiscale modeling allows integration of the microstructural details of different components into the modeling framework, hence capturing better the structural and mechanical complexities that exist in a tissue, and relating structure and mechanics on the microstructural level to overall tissue mechanics at the macroscopic level. Recent efforts in extending this model have focused on the ECM, with the fibrous material (e.g. collagen) represented by a fiber network, and other non-fibrous components (e.g. proteoglycans) represented as a solid Neo-Hookean material. This framework has been successfully used to model tissues and tissue equivalents, e.g., arteries (Stylianopoulos and Barocas, 2007), collagen-agarose co-gels (Lake et al., 2012a; Zhang et al., 2013), as well as model tissue damage (Hadi et al., 2012). A significant gap in this model, however, is the absence of cells, which are integral components in most tissues. The current work represents an improvement of the multiscale model via the addition of cells, and investigates the passive mechanical contribution of cells to overall tissue mechanics. As such, it constitutes an extension of our early study on passive cellular contribution based on Hashin's solution (Hashin, 1962) for a composite of rigid inclusions in a homogeneous, linear, and isotropic elastic matrix.

Materials and Methods

Multiscale Model Formulation

Cells were modeled as dilute, non-interacting spherical inclusions embedded within a fibrous ECM network. Cells were assumed to be dilute and non-interacting, such that they could be considered as organized in a periodic lattice (Fig. 1a). As such, a simplified mesh geometry containing a sphere in a box was sufficient to describe the cell-matrix system. Finite element mesh generation was performed in Abaqus (Dassault Systèmes Americas Corp., Waltham, MA); the cell was represented by an eighth of a sphere contained within a cube, with three symmetry planes as shown in Figure 1b. Three mesh geometries, corresponding to 5, 10, and 15% cell by volume, were created. For each case, tensile tests of up to 10% stretch in the *1*-direction were simulated by imposing displacement of 0.5% stretch per step on the positive *1*-face over 20 steps; stress-free boundary conditions were prescribed on the positive 2- and 3- faces by allowing compaction on these faces (Fig. 1b).

Our multiscale model couples the macroscopic scale (i.e. finite element mesh representing the tissue level) with the microscopic scale (representing the fibrous ECM network) via volume-averaging; a summary of the methodology is described here, with more detailed description found in (Chandran and Barocas, 2007; Stylianopoulos and Barocas, 2007). Briefly, each of the eight Gauss points in every element is associated with a unique representative volume element (RVE) comprised of a network of randomly

oriented fibrils (Fig. 1b), with the fibrils interconnected at cross-links represented by freely-rotating pin-joints. Initial guesses for the displacements of each RVE boundary are determined by linear interpolation of the nodal displacements to every Gauss point within the element; in turn, these nodal displacements are determined by the imposed macroscopic boundary conditions as described in Figure 1b. Force balances within each RVE are solved instead of a constitutive equation at each Gauss point. At static equilibrium, the vector sum of forces exerted by fibrils connected at each cross-link is zero, and the macroscopic (averaged) RVE Cauchy stress tensor, σ_{ij}^{macro}, can be computed by the forces exerted by the fibrils on the RVE boundaries:

$$\sigma_{ij}^{macro} = \frac{1}{V}\int_V \sigma_{ij}^{micro} dV = \frac{1}{V}\sum_{\substack{boundary \\ crosslinks}} x_i F_j \tag{1}$$

where V is the RVE volume, x_i is the i-th component of the coordinate where the fibril intersects the boundary, and F_j is the j-th component of the force acting on the boundary by the fibril. σ_{ij}^{micro} is the microscopic stress tensor of individual fibrils in the network; for a single fiber intersecting with a boundary,

$$\oint_{dV} \sigma_{ij}^{micro} n_i dS = F_j \tag{2}$$

where F_j is as defined above, and n_i is the unit normal of the boundary intersected by the fibril in question. The force exerted by each fibril, F, is governed by the exponential constitutive equation (Billiar and Sacks, 2000; Fung, 1993):

$$F = \frac{A}{B}\left(exp\left(BE_f\right) - 1\right) \tag{3}$$

In the above equation, A and B are material constants for each individual fibril. The constant A is a measure of fibril stiffness, and B captures the degree of non-linearity in mechanical behavior of individual fibrils. E_f is the fibril Green strain computed from the fibril stretch ratio, λ_f:

$$E_f = \frac{1}{2}\left(\lambda_f^2 - 1\right) \tag{4}$$

At small strains (i.e., as $\lambda_f \rightarrow 1$), a Taylor series expansion around $E_f = 0$ reduces equation 3 to a linear elastic fibril. The components of this force in each direction (F_j in equation 1) are computed by multiplying the force F (in equation 3) with the respective directional cosines for each fibril. Solving the macroscopic force balance yields the following expression for the divergence of the macroscopic Cauchy Stress tensor:

$$\sigma_{ij,i}^{macro} = \frac{1}{V}\oint_{dV}\left(\sigma_{ij}^{micro} - \sigma_{ij}^{macro}\right)u_{k,i}n_k dS \tag{5}$$

where u_k is the RVE boundary displacement and n_k is the unit normal vector, and σ_{ij}^{macro} defined in equation 1; equation 2 allows calculation of the integral of σ_{ij}^{micro} in terms of the boundary forces. The final deformation of each RVE at each Gauss point is dependent on the solution of equation 5 upon convergence.

Model Specification

Rigid Cell

Cells were first modeled as rigid inclusions by fixing all the nodes in the spherical region of the mesh. These simulations were motivated by our previous work on fibroblast-populated collagen gels, which compared experimental data to an analytical solution of

an inclusion-based model (Hashin, 1962). While we acknowledge that cells are generally deformable, this set of simulations allowed for direct comparison between our multiscale model predictions and this analytical solution. Developed by Hashin, this theory of linear elastic spherical inclusions embedded in an elastic, homoegeneous, isotropic matrix gave analytical expressions for approximating the composite bulk modulus (K^*) and shear modulus (G^*) from material constants of the inclusion (K_p, G_p), matrix (K_m, G_m, Poisson's ratio ν_m), and volume fraction of inclusions (c). In the limit of rigid inclusions (i.e. $K_p, G_p \rightarrow \infty$), these expressions reduce to (Evans and Barocas, 2009)

$$\frac{K^*}{K_m} = 1 + \frac{3(1-\nu_m)c}{(1+\nu_m)(1-c)} \tag{6}$$

$$\frac{G^*}{G_m} = 1 + \frac{15(1-\nu_m)c}{2(4-5\nu_m)(1-c)} \tag{7}$$

Three different cases were considered for the surrounding ECM: (1) linear elastic material (Hookean), (2) hyperelastic material (Neo-Hookean), and (3) a network of fibers, using our multiscale model as described above. Simulations for these three ECM cases were performed with rigid cell volume fractions of 0%, 5%, 10% and 15%. In the no-cell case (i.e., 0% cell volume fraction), results for the linear elastic and Neo-Hookean matrix cases were obtained directly from their respective constitutive equations (equations 8 and 9 below); for the case of the ECM containing a network of fibers, the mesh for 5% cell volume fraction was used, with all elements (including the cell elements) assigned as ECM elements. The linear elastic matrix was governed by Hooke's law:

$$\sigma_{ij}^{matrix} = 2G_m\varepsilon_{ij} + \frac{2G_m\nu_m}{(1-2\nu_m)}\varepsilon_{kk}\delta_{ij} \quad (8)$$

where ε_{ij} is the small strain tensor. These simulations were run in Matlab (The Mathworks, Inc., Natick, MA) using a custom code. The form of the Neo-Hookean equation used is (Bonet and Wood, 1997; Stylianopoulos and Barocas, 2007)

$$\sigma_{ij}^{matrix} = \frac{G_m}{J}\left(B_{ij} - \delta_{ij}\right) + \frac{2G_m\nu_m}{J(1-2\nu_m)}(\ln J)\delta_{ij} \quad (9)$$

where J is the determinant of the deformation tensor $F_{ij} \equiv \partial x_i/\partial X_j$, and B_{ij} is the left Cauchy-Green deformation tensor given by $B_{ij} = F_{ik}F_{jk}$. For these elastic models, the matrix shear modulus was set at G_m, = 4.2kPa, similar in magnitude to the value used to model the non-fibrillar matrix of the arterial wall (Roy et al., 2005; Stylianopoulos and Barocas, 2007). While soft tissues typically exhibit high Poisson's ratios in tension, often values greater than 1 (Cheng and Screen, 2007; Lake and Soslowsky, 2010; Lynch and Elliott, 2003), equations (6) to (9) are governed by elasticity theory and are only valid for Poisson's ratios ranging between -1 and 0.5; as such, the matrix Poisson's ratio was set at $\nu_m = 0.3$ for these models.

For an ECM comprising of a fibrous network, a Voronoi network of fibrils was used, generated from Voronoi tessellation about random seed points. Voronoi networks have a connectivity of four at each cross-link, similar to experimental observations of average connectivity in acellular collagen gels from confocal microscopy (Lai et al., 2012a). In addition, Voronoi networks have been used successfully to predict network mechanics in collagen gels (Nachtrab et al., 2011). All Voronoi networks generated contained

approximately 350 fibrils; each element was assigned a unique Voronoi network (with this same network for all 8 Gauss points within that element) randomly chosen from a set of 100 different networks. Hence, all 8 RVEs in each element have the same microstructure. Three simulations were made for the case of a network of fibers, which a different pool of 100 Voronoi networks used for each run. Values for materials constants *A* and B were 340nN and 2.5 respectively, obtained from previous experimental result for pure collagen gels (Lai et al., 2012b). For the Neo-Hookean and network cases, simulations were run using a 128-processor cluster at the Minnesota Computing Institute, with wall times on the order of 12 hours.

Cell Containing Network of Filaments

To include cell deformability, the filamentous structures on the cell were modeled using the same Voronoi networks as described above, with the same governing equation 3 for individual filaments. In addition, cells were assumed to be incompressible in the short term (e.g., during the duration of a tensile test). To impose incompressibility, a hydrostatic pressure term, *p*, was added to equation 1 to compute the Cauchy stress in the cell elements:

$$\langle \sigma_{ij}^{cell} \rangle = \frac{1}{V} \sum_{\substack{boundary \\ crosslinks}} x_i F_j - p\delta_{ij} \tag{10}$$

where *p* is the (uniform) pressure in the cell. This pressure, acting similarly to a Lagrange multiplier, represents the effect of the cytosol (i.e., intracellular fluid) on the cell, and was varied to allow the cell to maintain constant *total* volume. Individual elements within the

cell were not required to maintain volume, representing the ability of water to move within the cell but not across the cell membrane at the time scale of interest. The relative stiffness between the cell and matrix regions was changed by altering the value of the material constant A in equation 3:

(a) A_{cell} = 340nN, A_{matrix} = 3400nN – matrix 10 times stiffer than the cell

(b) A_{cell} = 3400nN, A_{matrix} = 340nN – cell 10 times stiffer than the matrix

(c) A_{cell} = 340nN, A_{matrix} = 340nN – same stiffness for cell and matrix

Case (c) did not reduce to a simple box with fibrils of similar properties throughout because of the incompressibility of the cell region. Because of the computational cost of running these multiscale simulations, a coarser 10 vol% finite element mesh containing 608 elements was used; mesh refinement was checked against a finer mesh containing 1812 elements, which resulted in a mean difference of less than 3% in the stress-strain response for case (c). Similar to the rigid cell case with the ECM represented by a network of fibers, each element contained a unique Voronoi network randomly selected from a pool of 100 different networks; for each case, three simulations were run using a different pool for each run. To quantify the orientation of the networks, the network orientation tensor was calculated as

$$\Omega = \frac{1}{l_{total}} \sum l_i \begin{bmatrix} \cos^2 \alpha_i & \cos \alpha_i \cos \beta_i & \cos \alpha_i \cos \gamma_i \\ \cos \alpha_i \cos \beta_i & \cos^2 \beta_i & \cos \beta_i \cos \gamma_i \\ \cos \alpha_i \cos \gamma_i & \cos \beta_i \cos \gamma_i & \cos^2 \gamma_i \end{bmatrix} \quad (11)$$

where l_{total} is the total length of all fibers in the network, l_i is the length of fiber i, and cos α_i, cos β_i, and cos γ_i are the directional cosines of fiber i with respect to the 1, 2, and 3

axis directions respectively. For an isotropic network, $\Omega_{11} = \Omega_{22} = \Omega_{33} = 1/3$, and all off-diagonal components are 0.

Statistical Analysis

Statistical analyses were done using the commercial statistical package in Origin (OriginLab Corporation, Northampton, MA). Comparisons of material properties between two groups were performed using a two-tailed unpaired t-test. For multiple groups, a 1-way ANOVA F-test, coupled with multiple comparisons using the Bonferroni procedure, was used.

Results

Rigid Cell

Plots of the undeformed meshes, as well as Cauchy σ_{11} stress distributions after 10% stretch, are shown in Figure 2, with the rigid cell removed for clarity. As expected, higher stresses were observed with increasing cell volume in all matrix cases, as the proportion of the infinitely stiff cell component increased. Stress concentrated in the matrix at the leading edge of tension in front of the cell, where the effect of the rigid cell was most felt. The largest stresses around this leading edge were observed for the network material cases; in the matrix-only regions above the cell, in contrast, the network material exhibited lower stresses than the linear elastic and Neo-Hookean matrix cases. These results demonstrate the highly non-linear mechanical behavior of the Voronoi networks compared to the Hookean and Neo-Hookean models: larger stresses in the matrix

elements near the cell were contrasted with smaller stresses in the matrix-only region above the cell. It should be emphasized that this effect of large stress gradients within the composite arises from the degree of non-linearity in the network model, and not from the relative stiffness of the fiber network compared to the constitutive models. Since the Hookean and Neo-Hookean models have a linear dependence on G_m, changing G_m will alter the *magnitude* of the stresses developed in the composite; the stress *distributions,* however, within the composite will be unchanged. In comparison, the high degree of non-linearity in the network model will still produce larger differences in stresses within the composite (compared to the Hookean and Neo-Hookean models), with much higher stresses in the leading front of the cell contrasted with smaller stresses in the cell-free region above the cell. Similar stress gradients to our network model may be observed if constitutive models with higher degrees of non-linearity are used, e.g., the Ogden model. Similarly, it is expected that increasing the fiber stiffness parameter A (in equation 3) will increase the magnitude of the stresses developed, while increasing the degree of non-linearity (parameter B) will alter the stress gradients developed within the composite.

This non-linear stress-strain behavior of the network material, similar to the mechanical behavior of soft tissues (Fung, 1967; Humphrey, 2003), is also shown in Figure 3. In contrast, the linear elastic and Neo-Hookean matrix cases showed relatively linear stress-strain characteristics that largely coincided with each other at all cell proportions. While lower stresses were observed in the network material composites for 0, 5 and 10% cell volume cases, rapidly increasing stress in the network material for the 15 vol% cell case

resulted in the overall composite stress overtaking the linear elastic and Neo-Hookean matrix cases at 10% strain. Unlike the smooth stress distributions in the linear elastic and Neo-Hookean matrix cases, greater variations were observed in the network matrix cases, attributed to the different Voronoi networks used for each element: slight differences in network mechanical behavior exist within the set of unique networks even though all networks had approximately the same number of fibers.

Quantitative comparisons of composite elastic modulus (E*) and Poisson's ratio between the different models are shown in Figure 4. Comparison of these material properties for the linear elastic matrix case with the Hashin model showed close agreement at low cell proportions, with larger deviations from the Hashin solution with increasing cell volume. Consistent with the qualitative observations of the stress-strain behavior in Figure 3, the network material exhibited a non-linear increase in composite stiffness with cell volume (Fig. 4a), compared to more gradual increases for the linear elastic and Neo-Hookean matrix cases. These results were consistent with experimental data from our previous study which showed increasing stiffness in our cell-seeded collagen gel tissue equivalents with cell volume fraction (Evans and Barocas, 2009). Results for the composite Poisson's ratio, ν^*, showed values for the network models that were larger than the elastic theory limit of 0.5 for incompressible materials (Fig. 4b). This observation is consistent with our previous studies using these networks (Lake et al., 2012a), and is a consequence of the looseness of the Voronoi network structure which allows the ECM to collapse significantly. That the composite Poisson's ratio, ν^*, decreased with increasing cell

proportion for the linear elastic and Neo-Hookean matrix cases (Fig. 4c) was expected since the rigid cell resisted compaction. The network material case, however, did not exhibit the same decreasing trend in ν^*; in fact, Figure 4c indicated higher Poisson's ratios for all cell proportions compared to the matrix-only (i.e. 0 vol%) case, although the difference was only statistically significant for the 15 vol% cell ($p = 0.047$).

Cell Containing Network of Filaments

Figure 5 shows plots of the Cauchy stress distributions after 10% stretch for the compressible and incompressible cell cases, averaged over the three simulations for each case, with varying relative stiffness for the cell and matrix components as described in Section 3.2. Here, a compressible cell is defined as the case without an intracellular pressure. The mottled appearance of stresses in these models can be attributed to variation among the 100 networks randomly sampled for each element. This phenomenon is especially noticeable in the compressible cell case with equal stiffness values for both the cell and matrix: even though the composite is effectively comprised of Voronoi networks prescribed with the same material properties, the mottled appearance is a consequence of slight differences in mechanical behavior between the networks used in each element. Altering the relative stiffness of the cell and matrix resulted in different stress distributions in the matrix around the cell. In the case of a stiffer cell (top row), higher resistance to the macroscopic stretch from the cellular filament network caused the matrix ahead of the cell in the stretch direction to bear a larger proportion of the overall deformation, hence producing higher matrix stresses around this region compared to the

cell-free region above it. Conversely, in the stiffer matrix case (bottom row), the compliant cell bore a disproportionately larger amount of deformation compared to the matrix ahead of the cell, thereby relieving stress in the matrix compared to the cell-free region above.

In all cases, incorporation of hydrostatic pressure to enforce incompressibility increased the stresses borne by the filament networks in the cell, countered by similar qualitative increases in matrix stresses directly ahead of the cell in the stretch direction, as the matrix bore a larger proportion of the overall stretch. These higher stresses in the cell networks were the result of restricted rotation of the filaments about their cross-links into the direction of stretch due to the outward pressure exerted against the cell membrane, shown qualitatively by the selected RVE plots of fiber stretches in Figure 6A, and quantified by the lower $<\Omega_{11}>$ values for the incompressible cell case in Figure 6B. The added resistance to cell deformation by the pressure consequently decreased the overall Poisson's ratio of the composite in all cases (Fig. 7), but this difference was not significant at the 95% level for the equal stiffness case. Similar to the rigid cell cases, no significant differences in ν^* were observed across all cases of the compressible cell; for the incompressible cell, the Poisson's ratio for the 10x stiffer cell was significantly higher than that of the 10x stiffer matrix ($p = 0.0036$), and equal cell and matrix stiffness cases ($p = 0.0285$).

The traction on the cell surface (averaged over 3 runs) was plotted for both the compressible and incompressible cell in Figure 8. The magnitude of the traction stress from the cell filament network was computed by $n_i n_j \sigma_{ij}$, where n_i and n_j both are the unit normal to each cell surface element, and σ_{ij} is the averaged Cauchy stress tensor of the cell element. Similar traction stress distributions were observed for all compressible cell cases: the cell networks developed large tensile stresses in region facing the 1-direction (i.e., direction of macroscopic stretch – exemplified by region A in the 10x stiffer compressible cell), contrasted with smaller stresses in the regions facing the transverse directions (i.e. regions under the Poisson effect – regions B and C). Since the transverse surfaces were stress-free, the cell regions B and C were expected to be stress-free regardless of the relative stiffness between the cell and the matrix, as confirmed by model simulations using a neo-Hookean formulation for both cell and matrix (data not shown). In the 10x stiffer cell and 10x stiffer matrix cases, however, these regions exhibited non-zero tensile stresses. This result is likely a consequence of the asymmetric mechanical behavior of these networks, which are strong in tension but very weak in compression, hence producing a net positive traction even in these transverse regions. Introduction of the cytoplasmic pressure to render the cell incompressible had the effect of increasing the tensile stresses in the networks throughout the cell. While the overall stress state of the cell ("Network Stress - Pressure" plots in Fig. 8) showed similar stress distributions to those in the compressible cell cases, addition of pressure had the effect of increasing the magnitudes of both the tensile and compressive stresses on the cell, with regions B and C now more evidently under compression, especially in the 10x stiffer matrix case.

Figures 9a and 9b show dimensional changes for the cell in the 1 and 3 directions for the compressible and incompressible cell cases, respectively, with schematic drawings underneath (Figs. 9c – 9h) illustrating the differences in cell shape after deformation, as well as the stresses exerted on the cell surface at static equilibrium. The normalized ratio of cell dimension to overall composite (cell + fiber matrix) dimension on either axis is a measure of the relative deformation of the cell compared to that of the overall composite. On the abscissa, a value greater than 1 means the cell stretch is greater than that of the composite in the 1-direction. Conversely, on the ordinate axis, a value greater than 1 indicates that the cell contracts less in the 3-direction than the matrix. For the compressible cell cases, the equal stiffness case exhibited little change in cell proportion in both directions under stretch, a result that was as expected. The 10x stiffer matrix case showed an increase in cell proportion in the 1-direction, but it did not predict a similar increase in cell deformation in the compressive 3-direction, a result that reinforced the idea that these networks, while strong in tension, had little compressive strength. While the 10x stiffer cell showed expected higher resistance to deformation in both directions, the above result strongly suggested that the increased resistance to compression was not due to a direct increase in cell compressive stiffness, but a consequence of lesser rotation into the direction of stretch due to increased *tensile* stiffness, which prevented compaction of the cell by inhibiting the collapse of the cell's filament network. In the compressible cell cases (Figs. 9c, 9e, 9g), matrix tension in the 1-direction was always balanced by cell tension. For the stiff cell (Fig. 9c), the matrix pushed in on the cell,

whereas for the stiff matrix, σ_{22} was positive for the cell, indicating that the cell was being pulled out by the matrix.

Enforcing cell incompressibility (Figs. 9d, f, h) had the effect of increasing the stresses of the filamentous networks in all cases; this increase in filamentous stress was countered by the cytoplasmic pressure pushing outward against the cell surface, such that the net effect was an increase in cell dimension in the 3-direction in all cases. In the 1-direction, this pressure exerted stress on the cell surface in the same direction as the matrix in tension, but did not cause the cell to elongate in this direction in all cases; in fact, cell dimension decreased for both the 10x stiffer cell and 10x stiffer matrix cases (albeit only a slight decrease in the latter). This observation could be explained by the fact that the intracellular pressure preserves volume by resisting changes to the overall cell shape. Hence, the net effect of this pressure is that the cell bears a smaller proportion of the overall deformation in both the tensile and compressive directions (compared to the case without pressure), as shown from comparison of Figures 9a and 9b. As a result, the filamentous network develops larger tensile stresses (due to restricted rotation into the direction of stretch, shown in Figure 6) that counters the effect of intracellular pressure working in tandem with the ECM tension.

Discussion

This study represented a major improvement to our multiscale model to understand soft tissue biomechanics by incorporating a major component of such tissues: cells. We

acknowledge, however, that several critical assumptions were used in the model development. First, the cell-matrix interface was modeled as continuous even though cells are known to attach to the matrix via discrete focal adhesions (Burridge et al., 1988; Goffin et al., 2006); Guilak and Mow (Guilak and Mow, 2000) asserted that such an assumption was not unreasonable based on experimental evidence of numerous focal adhesion points for chondrocyte attachment to its pericellular matrix from confocal and electron microscopy (Durrant et al., 1999; Eggli et al., 1988). In addition, the microstructural representations of both the ECM and cell were simplified to contain only a network. In reality, the ECM is generally comprised of other biomacromolecules (e.g. proteoglycans) which exist within the network interstitium, and which alter the overall mechanics of the tissue. For the cell, this reduced representation comprised entirely of a network of cytoskeletal filaments was chosen based on studies showing that the cytoskeleton was predominantly responsible for structural integrity and stiffness in a cell (Janmey and McCulloch, 2007), and hence is a reasonable first approximation for modeling the passive mechanical contribution of cells. The current model also accounts for equilibrium mechanical properties only, ignoring the viscoelastic behavior of both the cell and ECM. Nevertheless, development of this model helped gain significant insight into the cellular mechanical microenvironment, and laid the groundwork for future work incorporating further microstructural and mechanical details for the cell and ECM.

Comparison of the inclusion-based model of Hashin with our finite element model results showed close agreement at low cell volume fractions; deviation at higher cell

concentrations were expected since the Hashin model is only relevant at low inclusion densities. While our previous work on cell-seeded collagen gels showed close agreement of Young's modulus predicted by the Hashin model with experimental data at low cell volume fractions (Evans and Barocas, 2009), such models are unable to generate the highly non-linear stress-strain behavior of soft tissues. In addition, elastic theories preclude Poisson's ratios larger than 0.5, while many tissues have been shown to exhibit Poisson's ratios with values much higher than this elastic limit in tension. The ability of our multiscale network simulations to generate non-linear stress-strain behavior (as shown in Fig. 3) and Poisson's ratios beyond the elastic limit demonstrates a more viable and accurate model for application towards soft tissue biomechanics.

The multiscale model predicted similar composite Poisson's ratios regardless of the volume fraction of rigid cell. This unexpected result suggests that the composite Poisson's ratio is dependent only on the collapse of the network in the matrix above the cell, caused by fiber rotation about their cross-links. Across all volume fractions of rigid cell, the matrix-only region (above the cell) experiences the same amount stretch, hence the same degree of network collapse, to produce similar Poisson's ratios.

The model assumption that cells are incompressible is reasonable, validated by experimental data on single chondrocytes where an apparent Poisson's ratio of 0.49 was reported, although this value was shown to decrease with increasing axial strain (Ofek et al., 2009). Modeling the cell as compressible and incompressible, however, generally

represents two extreme cases of the effect of the intracellular fluid; in reality, a cell is likely to be "moderately" compressible and dependent on the time scale of observation. In such cases, we hypothesize that our results would lie between our extreme cases of the compressible and incompressible cells. The resistance to filament rotation into the direction of stretch due to the pressure (Fig. 6) would cause the network to stretch to an intermediate extent, thereby producing stresses bounded by the current results. Similarly, the intracellular pressure would resist cell compression, though to a smaller extent than the incompressible cell case shown in Figure 9b.

In a tissue under tension, the tensile stress on the cell by the fibrillar matrix has the effect of elongating the cell into the direction of stretch; such changes in cell shape and alignment are similar to experimental observations of contact guidance of cells, where cells preferentially elongate with the underlying matrix fibrils aligned under stretch (Eastwood et al., 1998; Huang et al., 1993).

Model results from this study show complex effects of relative cell and matrix stiffness, as well as cytoplasmic pressure, on the overall cellular mechanical microenvironment, which has implications on understanding cellular mechanosensation. That cells respond differently to varying substrate stiffness has been extensively studied, in terms of various cell properties and processes such as cell attachment (Chan and Odde, 2008) and morphology (Yeung et al., 2005), proliferation (Subramanian and Lin, 2005), stem cell differentiation (Engler et al., 2006), and migration (Hadjipanayi et al., 2009). The

justification for modeling the three different scenarios for the relative stiffness between the cell and the matrix was based on experimental results on different cell types showing a wide range of cell stiffness, e.g., from ~0.2kPa in fibroblasts, to 42kPa in cardiac myocytes (Janmey and McCulloch, 2007). From our previous studies, the elastic (tangent) modulus of 2mg/mL acellular collagen gels was found to be on the order of 10kPa (Lai et al., 2012b); compacted gels would exhibit significantly higher modulus. Hence, our three scenarios were designed to qualitatively cover a wide combination of cell types entrapped in different ECM. The current work shows that the stiffness of the matrix relative to that of the cell can also affect the qualitative and quantitative nature of strain transfer from the tissue to the cell. Even in the compressible cell case, the net transverse stress acting on a cell can be tensile or compressive depending on the relative stiffness of the cell and matrix. When the cell is incompressible, the existence of the cytoplasmic pressure can cause significant filamentous tension even in the transverse directions, which might be expected to be in compression or nearly stress-free. To the best of our knowledge, there are no published experimental data on detailed stress and/or strain fields of cells entrapped in a matrix under tension, for comparison with our model predictions.

Recently developed techniques, however, have the potential of quantifying cell/matrix stresses and strains in tissues under tension, e.g., measurement of three-dimensional traction forces exerted by cells entrapped in a hydrogel (Legant et al., 2010), and generation of three-dimensional strain maps of cells with their surrounding matrix (Pizzo,

et al., 2005). The combination of these experimental techniques with computational modeling can provide a clearer picture of the cellular mechanical microenvironment in tissues. Such findings can have implications on improving tissue engineering design, in terms of providing the optimal level of mechanical signaling to promote desired growth and remodeling by the cells.

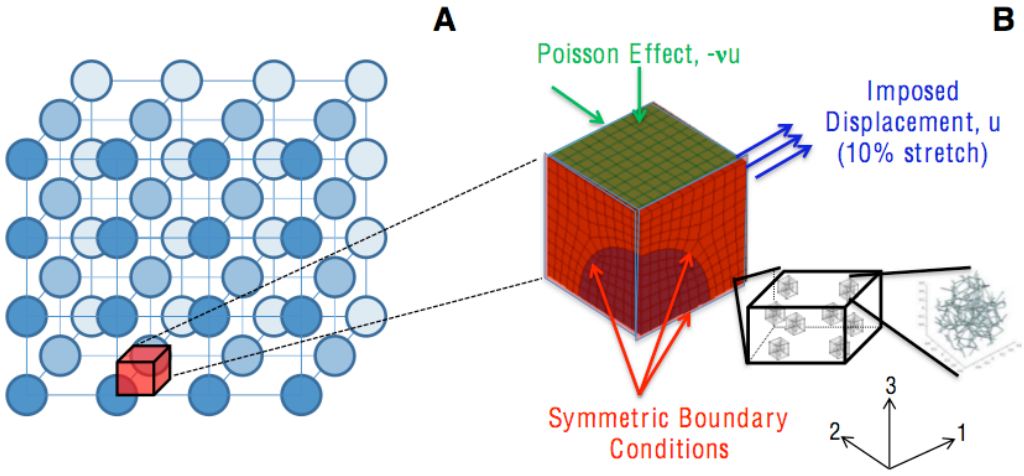

A1 Fig. 1: (A) Schematic representation of cells within a tissue organized in a periodic lattice, based on the assumption that cells are dilute, non-interacting, and spherical in shape. (B) Finite-element mesh showing boundary conditions and three symmetry planes. In the multiscale formulation, each Gauss point in every element is associated with a unique representative volume element (RVE) comprised of a random, interconnected network.

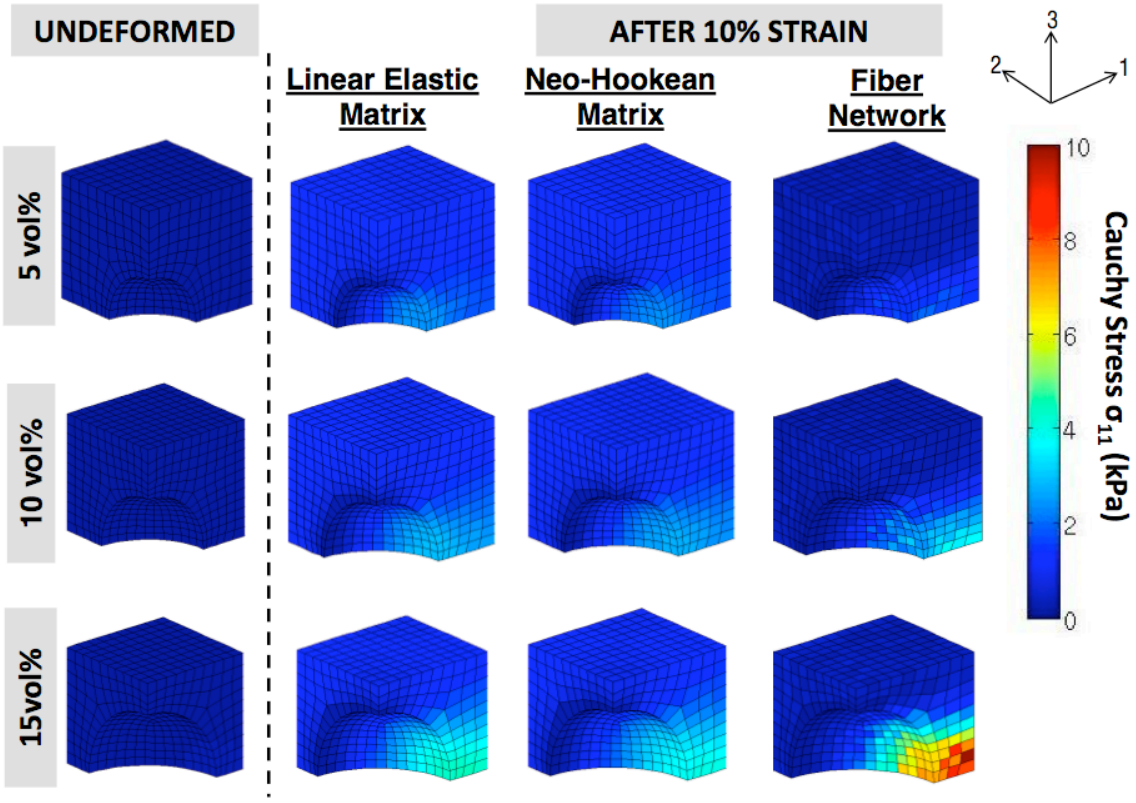

A1 Fig. 2: Undeformed meshes, as well as Cauchy stress (σ_{11}) distributions after 10% strain (averaged over 3 runs for each), for the cases of a linear elastic matrix, Neo-Hookean matrix, and a fiber network at rigid cell volume fractions of 5%, 10%, and 15%. The rigid cells were removed for clarity. In general, larger stresses were observed with increasing cell volume fraction. Variations in cell stresses in the fiber network cases were due to the uniqueness of Voronoi networks used for each element.

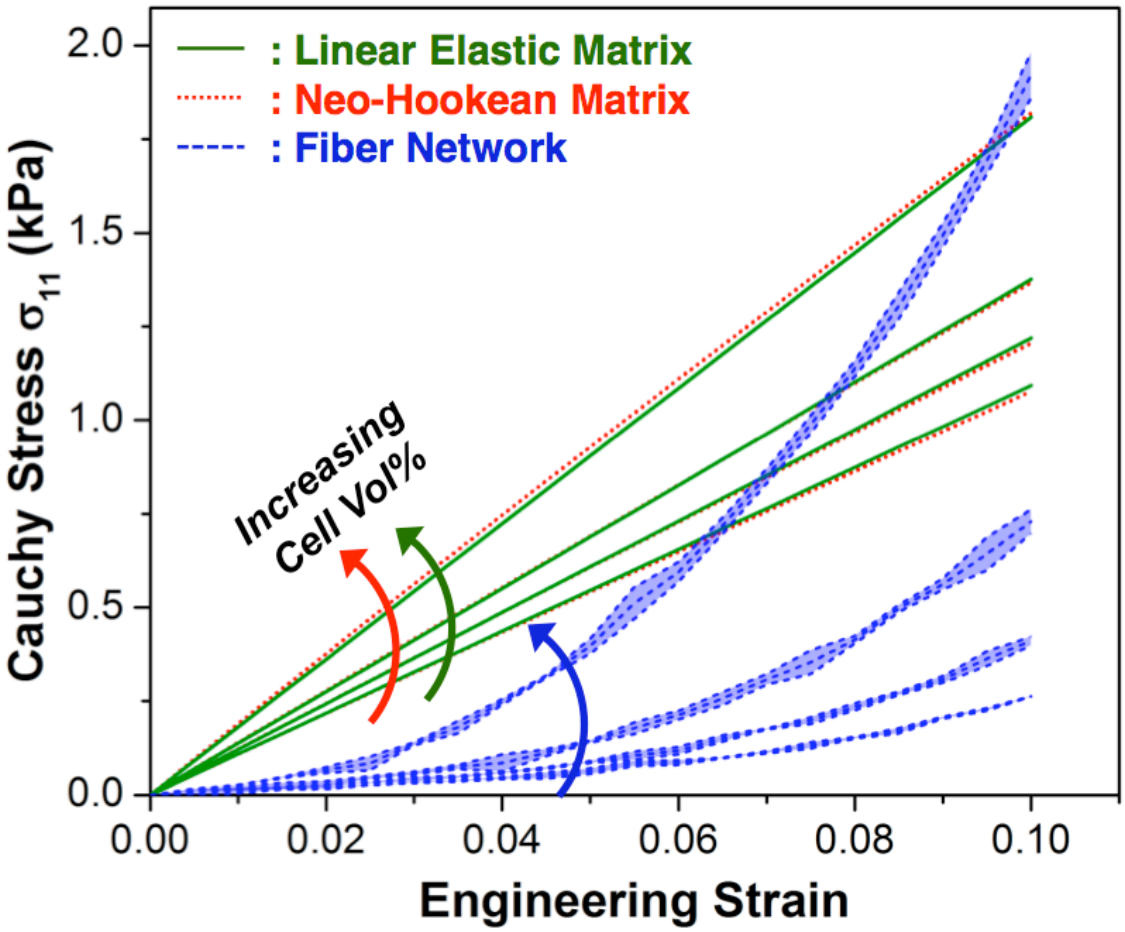

A1 Fig. 3: Cauchy stress σ_{11} vs engineering strain for the linear elastic matrix, Neo-Hookean matrix, and fiber network cases at rigid cell volume fractions of 0%, 5%, 10%, and 15%. Stress-strain curves for the linear elastic and Neo-Hookean matrix cases appeared linear and largely coincided with each other. The fiber network case exhibited non-linear stress-strain behavior, similar to that of soft tissues. Error bands in the fiber network cases are 95% confidence intervals, n = 3 for each case.

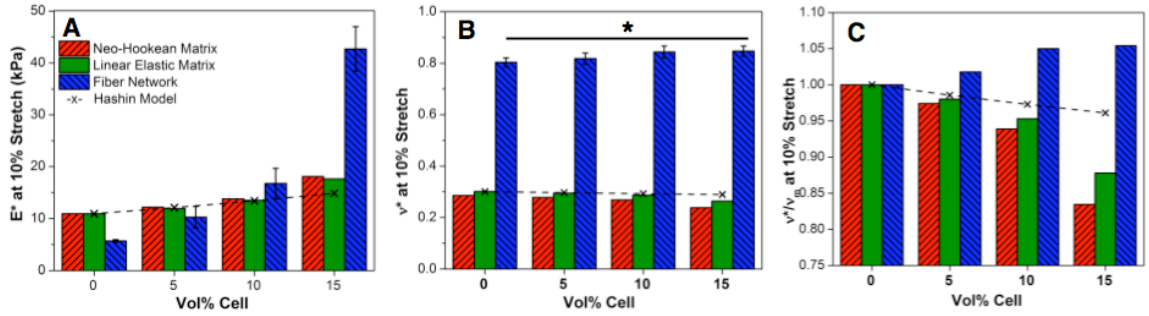

A1 Fig. 4: Plots at 10% stretch of (A) composite elastic modulus E*, (B) composite Poisson's ratio ν*, and (C) composite Poisson's ratio normalized with Poisson's ratio of the matrix, ν^*/ν_m, compared with the Hashin model. * represents statistical significance at the 95% level. Model results showed close agreement with the Hashin solution at lower volume fractions. Unlike the linear elastic and Neo-Hookean matrix cases, the Poisson's ratio for the fiber network case did not decrease with increasing cell volume fraction. Error bars for the fiber network cases are 95% confidence intervals, n = 3 for each case.

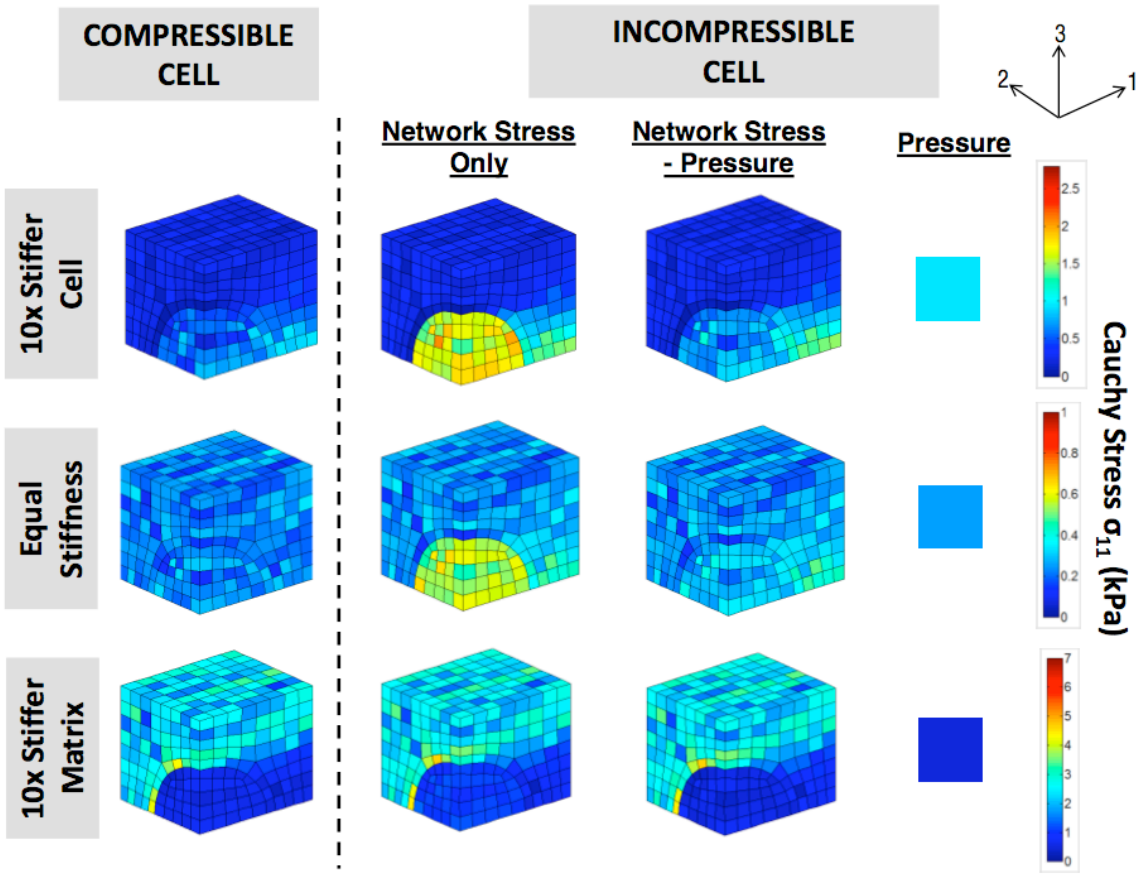

A1 Fig. 5: Cauchy stress (σ_{11}) distributions at 10% stretch of the 10x stiffer cell (1st row), equal cell and matrix stiffness (2nd row), and the 10x stiffer matrix (3rd row) cases, for both the compressible and incompressible cells (averaged over 3 runs for each case). Stress distributions around the cell differed depending on the relative stiffness of cell and matrix. In all cases, introduction of a cytoplasmic pressure to enforce incompressibility increased the stresses borne by the cell filament networks.

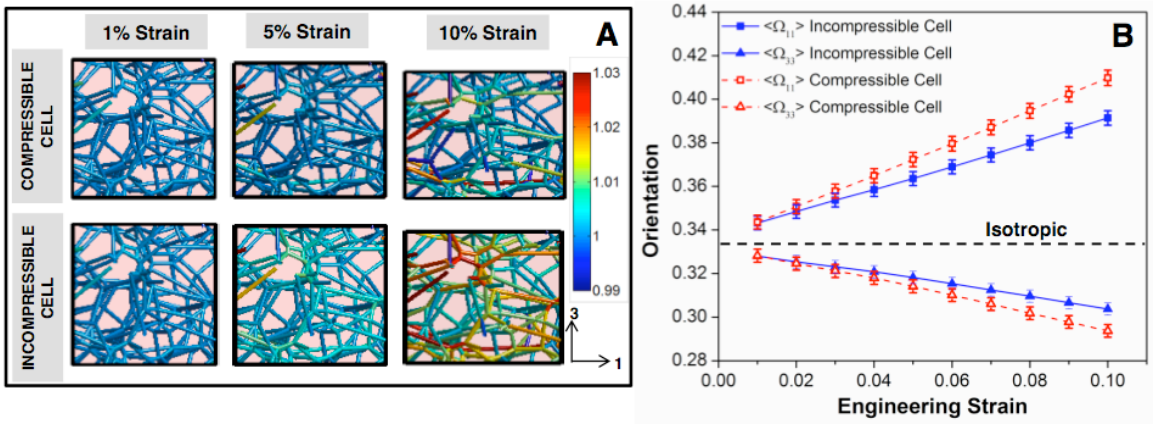

A1 Fig. 6: (A) Representative cell filament network at 1%, 5% and 10% strain for the compressible and incompressible cell cases, showing the distribution of filament stretches in the networks. Larger filament stretches were observed for the incompressible cell case. (B) Average filament orientation in the 1 (Ω_{11}) and 3 (Ω_{33}) directions vs. strain for the compressible and incompressible cell cases. Introduction of a cytoplasmic pressure inhibited filament rotation into the direction of stretch, such that the filaments were less oriented in the incompressible cell. Error bars are 95% confidence intervals, n = 112 (total number of cell elements).

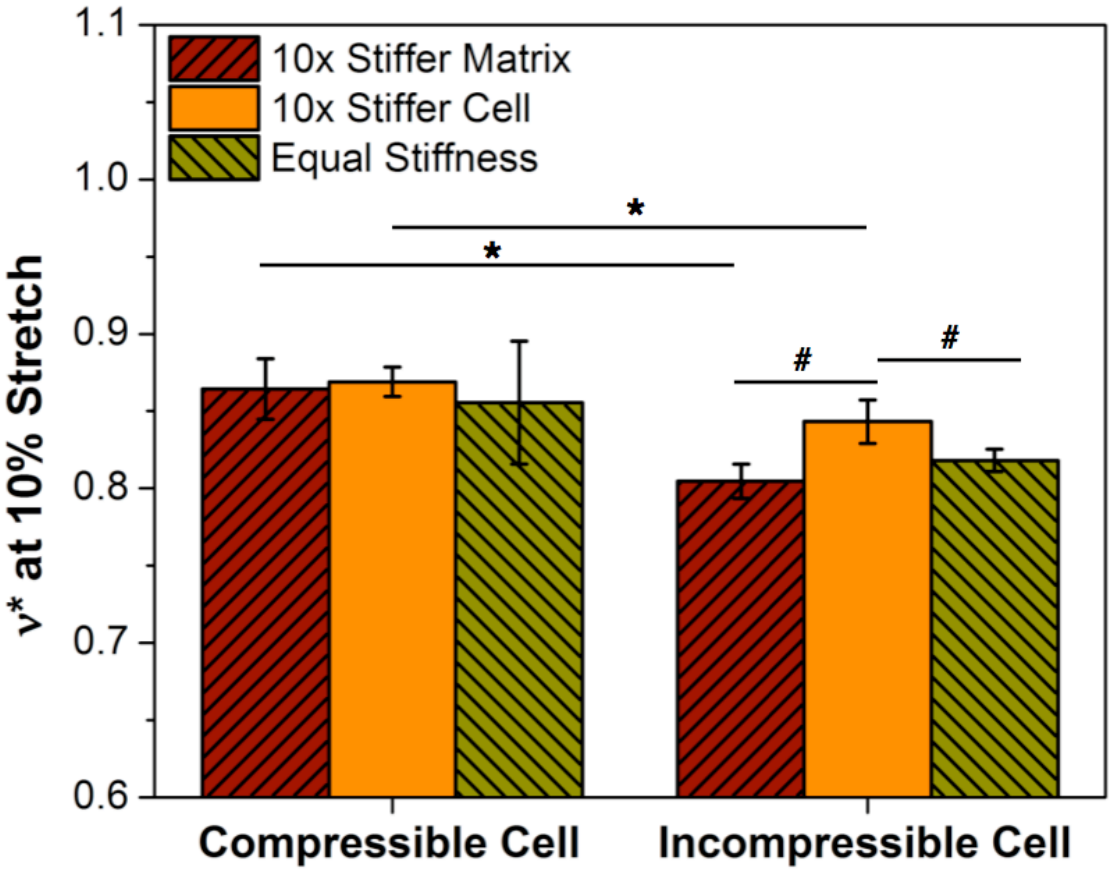

A1 Fig. 7: Composite Poisson's ratio, ν*, at 10% stretch for the compressible and incompressible cell cases, with different relative stiffness of cell and matrix. * and # represent statistical significance at the 95% level. No significant differences were observed between the different relative stiffness cases for the compressible cell. The 10x stiffer cell case had significantly higher ν* than the 10x stiffer matrix ($p = 0.0036$) and equal stiffness ($p = 0.0285$) cases for the incompressible cell. Error bars represent 95% confidence intervals, with $n = 3$ for each case.

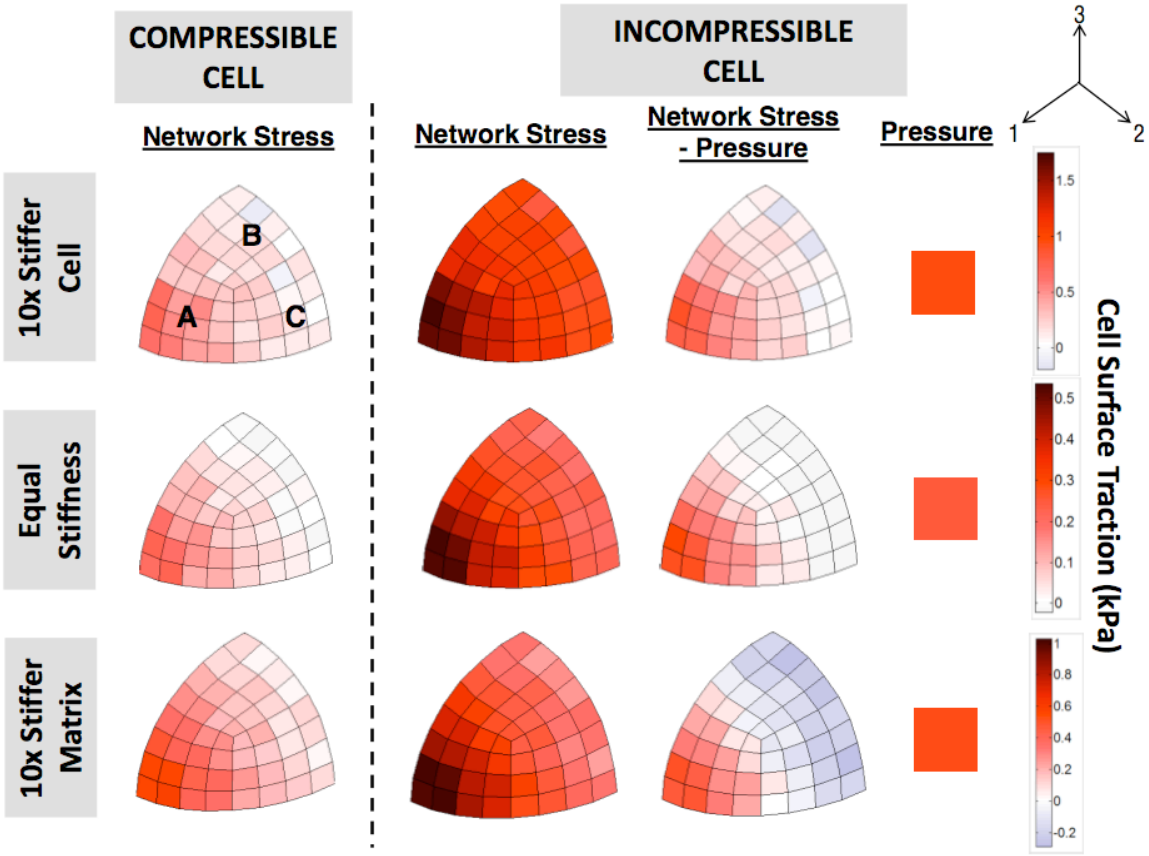

A1 Fig. 8: Cell surface traction at 10% stretch of the 10x stiffer cell (1st row), equal cell and matrix stiffness (2nd row), and the 10x stiffer matrix (3rd row) cases, for both the compressible and incompressible cells (averaged over 3 runs for each case). In the compressible cell cases, large tensile stresses were observed in the direction of tension (region A). The cell surface region under the Poisson effect (regions B and C) did not exhibit large compressive stresses. Addition of pressure increased the surface traction from the cell filament network, and slightly increased the overall compressive stress in regions B and C.

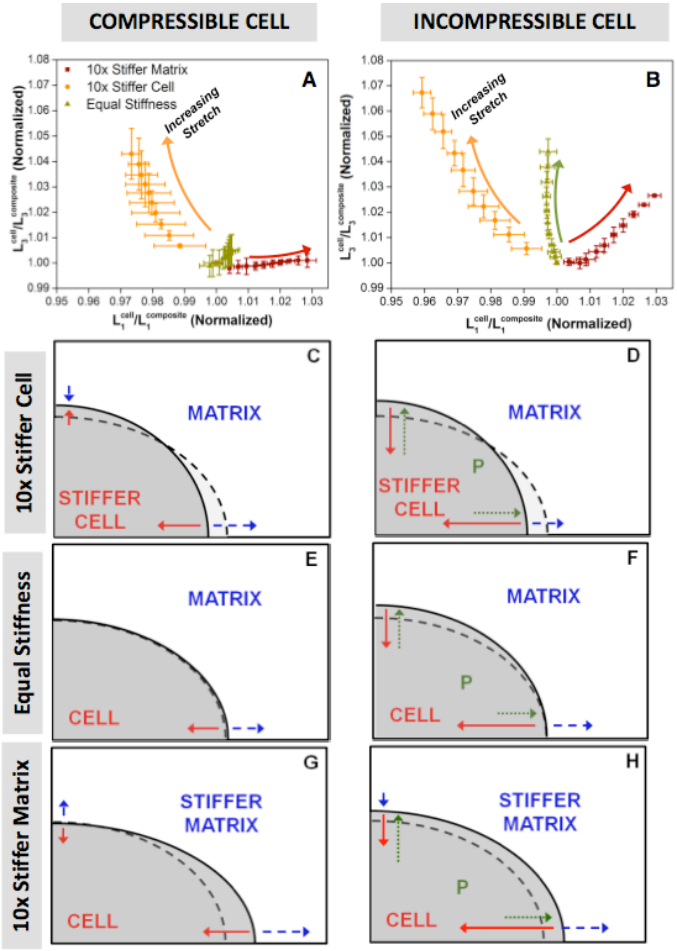

A1 Fig. 9: (A-B): Normalized ratio of cell dimension to composite dimension in the 3-direction vs. the 1-direction. Addition of pressure increased the cell proportion in the 3-direction for all cases. (C-H): Schematic drawings showing differences in cell shape, and the stresses exerted on the cell surface at equilibrium; dotted lines represent the equal cell and matrix stiffness case without pressure. In the compressible cell cases (C, E, G), matrix tension in the 1-direction was always balanced by cell tension. In the incompressible cell cases, (D, F, H), the outward-exerting pressure pushed out against the cell to increase cell proportion in the 3-direction.